

Optical and transport properties of GaN/(Al,Ga)N heterostructures in prospect of infrared unipolar devices

THÈSE N° 6751 (2015)

PRÉSENTÉE LE 25 SEPTEMBRE 2015

LABORATOIRE EN SEMICONDUCTEURS AVANCÉS POUR LA PHOTONIQUE ET L'ÉLECTRONIQUE
PROGRAMME DOCTORAL EN PHOTONIQUE

ÉCOLE POLYTECHNIQUE FÉDÉRALE DE LAUSANNE

POUR L'OBTENTION DU GRADE DE DOCTEUR ÈS SCIENCES

PAR

Étienne GIRAUD

acceptée sur proposition du jury:

Prof. H. P. Herzig, président du jury
Prof. N. Grandjean, directeur de thèse
Dr F. Julien, rapporteur
Dr J. Y. Duboz, rapporteur
Prof. C. Ballif, rapporteur



ÉCOLE POLYTECHNIQUE
FÉDÉRALE DE LAUSANNE

Suisse
2015

Abstract

Over the past decade, a growing interest appeared for III-nitride semiconductors, in view of their potential applications in intersubband (ISB) devices. If these materials are nowadays famous, particularly for having revolutionized domestic lighting thanks to the GaN-based white light emitting diodes, they also feature interesting properties that make them good candidates for infrared (IR) devices. Indeed, their large conduction band offsets (~ 1.8 eV for the AlN/GaN system) enable near-IR ISB applications, at telecommunication wavelengths. Moreover, their large LO-phonon energy, makes them good candidates for devices operating at room temperature in the THz range. They also exhibit ultrafast ISB recombination dynamics, and therefore are promising for high frequency optoelectronic devices.

In the first part, this work presents results obtained on near and mid IR quantum cascade detectors (QCDs). Those devices are a first good step towards quantum cascade lasers (QCLs), as they possess similar multi quantum well (MQW) structures, and similar transport mechanisms. GaN-based QCDs, grown by plasma-assisted molecular beam epitaxy (MBE) have already been demonstrated in the near-IR. In this work, the feasibility of such structures using an NH_3 -source MBE system is demonstrated using optimized growth conditions. In addition, two QCDs presenting novel features are described. The first one, for near-IR applications, detects two different wavelengths, notably at $\lambda \sim 1 \mu\text{m}$ which corresponds to the shortest wavelength ever reported for an ISB device. The second one proposes a new design, relying on a thick alloy extractor instead of a MQW cascade structure, which can be scaled for long wavelengths operations.

The second part presents an in-depth study on resonant tunneling diodes (RTDs). Those devices rely on the non-linear coherent transport of electrons through two potential barriers sandwiching a quantum well (QW). Resonant tunneling is characterized by the appearance of a resonance peak followed by a negative differential resistance in the current-voltage transport measurements. GaN-based RTDs have been extensively studied, since they exhibit a twofold interest: (i) they could be used as oscillators emitting in the THz range, and (ii) they form a key element to understand the mechanism of vertical transport across superlattices, a necessary milestone for the realization of QCLs. However, the reported results are controversial and

present discrepancies. In order to understand these discrepancies, a comprehensive study, together with an original approach are proposed: using weakly strained quantum heterostructures, namely low Al content double barrier GaN/AlGa_N QW achieved after MOVPE growth condition optimization. A self-aligned process is also developed to downsize the device, in order to study the impact of dislocations. The excellent quality of the grown layers is demonstrated by means of low temperature photoluminescence spectroscopy, photo-reflectivity and X-ray diffraction. If the samples reveal similar discrepancies as those already reported in the literature (hysteresis and rapid ageing), this study points out their potential origins, following a deep investigation of the processing issues. Finally, a simple theoretical model is proposed to explain the difficulties encountered to observe quantum coherent electronic transport in GaN-based RTDs.

Key words: III-nitride semiconductors, intersubband transition (ISBT), multi quantum well heterostructure, molecular beam epitaxy (MBE), metal-organic vapor phase epitaxy (MOVPE), unipolar optoelectronic devices, resonant tunneling diode (RTD), negative differential resistance (NDR), quantum well infrared photodetector (QWIP), quantum cascade detector (QCD), quantum cascade laser (QCL).

Résumé

Durant la dernière décennie, les semiconducteurs III-V nitrures ont connu un très fort regain d'intérêt en raison de leur potentiel d'applications unique pour les dispositifs mettant en jeu des transitions intersousbandes. Cependant, ces matériaux sont aujourd'hui plus connus en raison de leur impact colossal dans le domaine de l'éclairage domestique, avec notamment la généralisation des LEDs blanches. Néanmoins, leurs propriétés physiques sont aussi particulièrement intéressantes pour développer des dispositifs optoélectroniques dans l'infrarouge (IR). En effet, la discontinuité au niveau de la bande de conduction entre GaN et AlN atteint la valeur record de 1,8 eV, ce qui permet de fabriquer des structures à puits quantiques absorbant dans la gamme de fréquence des télécommunications. Qui plus est, le temps de relaxation des porteurs dans ces structures est extrêmement rapide, ce qui en fait des candidats de choix pour des applications haute-fréquence.

Dans la première partie, nous présentons les résultats obtenus sur les détecteurs à cascade quantique (QCDs) dans le proche et moyen IR. Ces dispositifs sont un premier pas vers les lasers à cascade quantique (QCLs) car leur structure active et les mécanismes de transports sont similaires. Ces structures ont été fabriquées par épitaxie par jets moléculaires utilisant l'ammoniac comme source d'azote. Deux types de QCDs ont été réalisés : l'un pour des applications dans le proche IR qui peut détecter deux longueurs d'onde différentes, notamment à $\lambda \sim 1 \text{ nm}$, ce qui correspond à la plus courte longueur d'onde jamais reportée pour un dispositif intersousbande. Le second dispositif propose un nouveau design, qui repose sur un extracteur épais à base d'alliage AlGaIn, dans lequel le champ électrique est mis à profit.

La deuxième partie présente une étude sur les diodes à effet tunnel résonant (RTD). Ces dispositifs mettent en jeu le transport électronique cohérent à travers deux barrières de potentiel encadrant un puits quantique. L'effet tunnel résonant se caractérise par l'apparition d'un pic de résonance suivi d'une résistance différentielle négative, clairement identifiable sur les caractéristiques courant-voltage. Les RTDs à base de GaN ont fait l'objet de nombreuses études, car elles présentent un double intérêt : (i) comme oscillateurs pour l'émission dans le domaine THz, et (ii) comme élément clé pour comprendre les mécanismes associés au transport vertical d'électrons dans les super-réseaux, un étape cruciale vers le QCL. Il faut

remarquer que l'état de l'art sur les RTDs fait ressortir de nombreux points qui restent à éclaircir. C'est l'objet du dernier chapitre de cette thèse qui fait d'abord le point sur la situation, puis présente nos propres résultats, avant d'étudier en détails le rôle essentiel des différentes étapes de fabrication des dispositifs. Enfin, une modélisation de RTDs à base de GaN permet de mettre en lumière l'impact décisif du champ électrique ainsi que du désordre dans ce type de structures, et permet de mieux comprendre les difficultés rencontrées lors de mesures expérimentales.

Mots clefs : Nitrures d'élément III, Transition intersousbande (ISB), Heterostructure à multi-puits quantiques, Epitaxie par jets moléculaires (MBE), Epitaxie en phase vapeur d'organometalliques (MOVPE), dispositif optoélectronique unipolaire, diode à effet tunnel résonant (RTD), Détecteur infrarouge à puits quantiques (QWIP), Détecteur à cascade quantique (QCD), Laser à cascade quantique (QCL).

Contents

Abstract, Résumé	i
1 Introduction	1
2 Basics on III-nitride semiconductors and intersubband transitions	5
2.1 A brief history of III-nitride semiconductors	5
2.2 Basics properties of GaN and related compounds	6
2.2.1 Crystallographic phase and lattice parameters	6
2.2.2 Band Structure and bulk optical properties	8
2.2.3 Mechanical properties and polarization fields	10
2.3 Epitaxy and structural characterization	14
2.3.1 Substrates and relative lattice mismatch	14
2.3.2 Molecular beam epitaxy	15
2.3.3 Metal-organic vapour phase epitaxy (MOVPE)	19
2.3.4 Structural and basic optical characterization	20
2.4 III-nitride MQWS properties and band structure calculations	22
2.4.1 Polarization fields in the structures: quantum confined Stark Effect	22
2.4.2 Effective mass model and non parabolicity effects	25
2.4.3 The envelope function approximation	26
2.4.4 Many body effects: the Hartree method	28
2.5 Intersubband transitions in 2D confined systems	29
2.5.1 ISB optical transition and oscillator strength	29
2.5.2 ISB selection rules	31
2.5.3 Specificities of ISB transitions in GaN	33
2.6 State of the art of ISB optoelectronic devices	34
2.6.1 Brief history of ISB transitions and devices	34
2.6.2 Review of GaN based ISB devices	36

3	Intersubband photodetectors	39
3.1	Physics of IR photodetectors	39
3.1.1	ISB photodetectors: principles and figures of merit	39
3.1.2	Photoconductive QWIPs	43
3.1.3	Photovoltaic QWIPs	44
3.1.4	Quantum cascade detectors	45
3.2	GaN based QCDs	47
3.2.1	Motivations for a GaN based QCD	47
3.2.2	Specificities of polar GaN-based QCDs	47
3.2.3	Growth of QCDs by NH ₃ -MBE	48
3.3	A two-color quantum cascade detector	55
3.3.1	Design of the structure	55
3.3.2	Growth and structural characterization	57
3.3.3	Process and characterization	58
3.4	QCD using large AlGaIn extractor	60
3.4.1	Simulations and design	60
3.4.2	Growth and structural characterizations	62
3.4.3	Characterization of the device	63
3.4.4	Detection enhancement using plasmonic structures	64
3.4.5	Growth issues and strain engineering on alloy extractor QCD	65
3.5	Conclusion and Outlooks	68
4	Unipolar vertical transport in (Al,Ga)N/GaN heterostructures	71
4.1	Principles and motivations for the resonant tunneling diodes	71
4.2	Physics of resonant tunneling: the coherent transport model	72
4.2.1	Luryi's picture	72
4.2.2	Esaki's transport model	74
4.2.3	Transmission coefficient calculation: transfer matrix model	75
4.2.4	Limits of the model	77
4.3	Challenges and review of resonant tunneling in GaN	79
4.3.1	Challenges for GaN-based RTDs	79
4.3.2	Littérature review	80
4.4	First generation of RTDs: GaN/AlN structures	84
4.5	Second generation of RTDs: presentation of the approach	86
4.5.1	Materials and growth	86
4.5.2	Processing	88
4.5.3	Design and simulations	90
4.6	Growth quality assessment	94

4.6.1 X-ray diffraction and HR-TEM on MQWs structures	94
4.6.2 Temperature dependent optical spectroscopy	95
4.6.3 Growth control on double barrier structures	97
4.7 Electrical characterization	97
4.7.1 Observed features	98
4.7.2 Effects low temperature measurements, and other treatments	100
4.7.3 Summary of the results	101
4.8 Characterizations of barrierless samples	101
4.8.1 Current-voltage characteristics	101
4.8.2 Process issues	104
4.8.3 Process without dry-etching of GaN	105
4.8.4 Summary of results on barrierless samples	106
4.9 Impact of disorder on the resonance: simulations	106
4.10 Conclusions	110
5 Conclusions and perspectives	111
A Details of RTDs processing	113
B List of acronyms	117
Bibliography	129
Acknowledgements	131
Curriculum vitae	133

1 Introduction

III-nitride semiconductors are interesting materials. Thanks to their large bandgap energies, they are suitable for the optoelectronic interband devices ranging from the ultraviolet to the near infrared. Nowadays, they are widely used, for instance in lighting applications, thanks to the GaN-based white light emitting diodes or in blue-ray players, which rely on GaN based laser diodes. They can also withstand high electric power densities and high breakdown voltages, which makes them materials of choice for high power and high frequency electronics applications.

In addition, III-nitride appears to be excellent candidates for ISB applications. Indeed they exhibit large conduction band offset (up to 1.75 eV for the AlN/GaN system [1]), enabling intersubband (ISB) transitions at short wavelengths. In addition, they exhibit a large LO-phonon energy (92 meV in GaN, compared to 33 meV in GaAs), theoretically leading to two advantages: the possibility to get devices operating at room temperature, plus the possibility to make efficient terahertz sources working at wavelengths corresponding to the LO-absorption band of GaAs (*i.e.* the so-called THz gap).

For all those reasons, ISB transitions have been widely studied since 2000. However, most of the reported results until 2010, covers the near and mid-IR ranges, from 1.5 μm to 3-4 μm . Good performance devices, such as electro-modulators or quantum cascade detectors (QCD), have been reported [2, 3]. However, no quantum cascade laser (QCL) has been reported so far. Indeed, those devices require a very high material quality. This is not the case for the GaN/AlN system, used for near IR ISB devices, which suffers from a large amount of defects, mainly due to the lattice mismatch between those two binary compounds, and to the quality of the AlN templates featuring a dislocation density of $\sim 10^9 \text{ cm}^{-2}$. ISB THz absorption has been recently reported in GaN/AlGaIn heterostructures [4], which is promising for subsequent studies. In addition, for THz applications, such high conduction band offsets are not required, which allows the use of low Al content AlGaIn barriers, that have been proven in our laboratory to

exhibit very low inhomogeneous broadening [5]. The possibility to grow such structures, which possess a lower lattice mismatch compared to the GaN/AlN system, on low dislocation density GaN free-standing substrates, brings as well good hopes for advanced THz ISB optoelectronic devices.

In the present work, we explore two different devices, whose demonstration is a crucial steps towards QCLs: the QCD, which features multi quantum well-based cascade structures, similarly to QCL, and the resonant tunneling diode (RTD), which is a crucial building block to understand vertical coherent transport across heterostructures, and therefore is a necessary milestone towards the realization of a QCL.

Outline

Chapter 2 reports on the basics of III-nitride materials and intersubband transitions. First it gives an overview of the history, then details the physical properties, and particularly the spontaneous and piezoelectric polarization and their consequences on GaN-based heterostructures grown along the (0001) polar axis. The growth techniques and characterization tools are also presented. It is followed by a description of the physics of ISB transitions and their selection rules. Finally a review on ISB devices, and particularly of III-nitride ones is presented. Chapter 3 presents the results obtained on GaN-based QCDs grown by plasma-assisted molecular beam epitaxy (MBE) in the near and mid IR. At first the physics and figures of merit of IR detectors are detailed. Then, the growth conditions and the related optimizations by NH_3 -MBE for near and mid IR applications are discussed. Two QCDs presenting particular characteristics are demonstrated: the first one, for near-IR applications, is a QCD detecting at two different wavelengths, thanks to the $e_1 e_3$ ISB transition. The second one proposes a new design, relying on a thick alloy extractor instead of a multi quantum well cascade structure, and presenting interesting characteristics. This design can be scaled for operations at longer wavelengths.

Chapter 4 describes an in-depth study on RTDs. The physics of resonant tunneling is first detailed. A critical extensive literature review on GaN-based RTDs is carried out, pointing out the different features observed and their common discrepancies. To tackle these issues, a comprehensive study of RTDs is presented. It relies on metal-organic vapor phase epitaxy (MOVPE) GaN/AlGaN ($x_{Al} \leq 15\%$) heterostructures grown on high quality free-standing GaN substrates. The motivations about the choice of this system are deeply discussed. In addition, a specific process has been designed to get small mesa sizes, which is expected to enable to monitor the impact of dislocations. Following the given results, that exhibit discrepancies similar to those reported in the literature, a detailed study on the processing issues is performed and an explanation for those discrepancies is tentatively given. Finally,

a simple theoretical model based on transfer matrix calculation is proposed to explain the difficulties encountered to observe quantum coherent electronic transport in GaN-based RTDs.

2 Basics on III-nitride semiconductors and intersubband transitions

This chapter aims to present in the first place the basic structural and optical properties, the growth techniques of III-nitride semiconductor compounds and their heterostructures. Molecular beam epitaxy (MBE) growing method is detailed, as it consists a major part of this work. In the second part, the theory of intersubband ISB transitions is presented, and their specificities in III-nitrides are discussed. Different existing ISB optoelectronics devices are finally presented.

2.1 A brief history of III-nitride semiconductors

Even though there have been reports of GaN growth in the 20s and 30s, the real interest in III-nitrides has started in the late 60s, when single crystals of GaN could be grown on sapphire by Maruska *et al.* [6]. Few years later, optical spectroscopy on GaN single crystals obtained from hydride vapour phase epitaxy (HVPE) growth by M. Ilegems and coworkers, revealed a clear excitonic resonance, which allowed determining the bandgap energy [7]. However, due to the poor quality of epitaxial layers (high dislocation densities, high residual n-type doping) and to the difficulties to get p-type doping, the research on III-nitrides was nearly stopped for several years.

From the mid 80s, improvements in metal-organic vapour phase epitaxy (MOVPE) growth techniques could circumvent the above mentioned issues and lead to efficient light emitting diodes (LEDs). It started in 1986 from the work of Akasaki, Amano and coworkers, when they discovered that GaN quality grown on sapphire could be improved using an AlN buffer [8]. Few years later they obtained p-type doping with magnesium, using a post-growth low energy electron beam irradiation [9], which could lead to the first true GaN-based p-n junction LED [10]. Meanwhile, the works of Nakamura and co-workers further improved the material quality using a low temperature GaN buffer layer on sapphire [11] and got an efficient p-type doping

performing thermal annealing [12]. Particularly, they understood the role of Mg-H complexes in acceptor compensation mechanisms. All those advancements could lead to the first candle class double hetero-junction blue LED in 1994 [13], and two years later, to the first GaN-based blue laser diode (LDs) [14]. In 2014, Akasaki, Amano and Nakamura got awarded the Nobel Prize for their discoveries leading to efficient blue LEDs.

Today, the most thriving applications of GaN and related compounds are LEDs for lighting applications, laser diodes (*eg.* for blue-ray players) and high electron mobility transistors. GaN is indeed a very good candidate for high power electronics since it can withstand high power densities and large breakdown voltages comparing to other III-V compounds.

2.2 Basics properties of GaN and related compounds

2.2.1 Crystallographic phase and lattice parameters

Unlike most of conventional III-V semiconductor compounds, such as GaAs or InP, which crystallize in a cubic zinc-blende phase, the most stable crystal phase of III-nitrides (where III stands for a group III metallic atom like Al, Ga or In) is the hexagonal wurtzite phase. The zinc-blende phase of GaN can also be obtained using appropriate substrates and proper growth conditions, however all this work has been made using hexagonal III-N compounds. Fig. 2.1(a-b) represent the unit cell and the conventional cell of the wurtzite structure. This crystal structure is anisotropic, which means that most of its properties will differ from one direction to another (*eg.* effective masses, dielectric constants, *etc.*). Fig. 2.1(b) shows the projection of the wurtzite cell: each species form a closed packed stacking with a *ABAB...* sequence. In comparison (Fig. 2.1(c)) the zinc-blende crystal structure exhibits a *ABCABC...* stacking sequence.

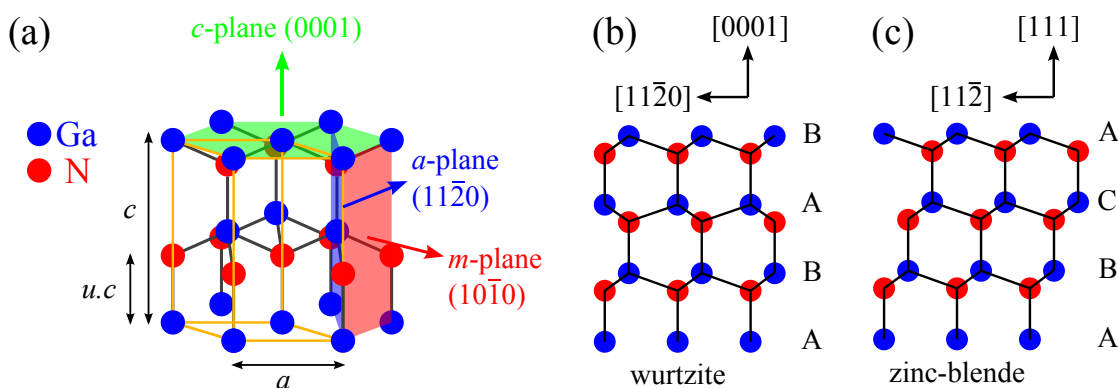


Figure 2.1 – (a) Representation of the conventional hexagonal cell of GaN in wurtzite phase; *c*, *a* and *m* planes are represented in different colors. (b) projection of the crystal structure along the *a* plane, (c) and projection of the zinc-blende crystal structure along $(1\bar{1}0)$ plane.

2.2. Basics properties of GaN and related compounds

The wurtzite phase features a C_{6v} point group symmetry. Each species form independently a hexagonal close compact lattice. The atomic orbitals are sp^3 hybridized, inducing the tetragonal form of each site, where each atom is connected to four other atoms of the complementary species. The distance between the two atoms is noted $u.c$, where c is the height of the hexagonal unit cell. In a perfect wurtzite lattice, those values are:

$$c = \sqrt{\frac{8}{3}}a \quad \text{and} \quad u = \frac{3}{8}$$

The actual figures slightly differ from the ideal ones. The lattice constants of III-nitride compounds are give in table 2.1.

It should be noticed that the wurtzite phase is a non-centrosymmetric system. In other words, the crystal does not have an inversion point symmetry, meaning that the two crystalline directions $[0001]$ and $[000\bar{1}]$ are not equivalent. Depending on the growth conditions and the substrate, GaN can be grown in one or the other direction. The first corresponds to the so-called metal-polarity (the one represented on Fig. 2.1(a-b)), and the latter to the N-polarity. In this work, all studied samples are metal-polar.

Concerning the ternary alloys, the lattice parameters are calculated using the linear Vegard's law:

$$P(A_xB_{1-x}N) = xP(AN) + (1-x)P(BN), \quad (2.1)$$

where x is the alloy content, and A and B stand for the metallic species (Al, Ga or In).

Table 2.1 – Usual III-N basic parameters taken from Ref. [15] if not specified.

Parameter	AlN	GaN	InN
a (Å) at T = 330 K	3.112	3.189	3.545
c (Å) at T = 300 K	4.982	5.185	5.703
u^a	3.82	3.77	3.79
thermal expansion along a ($10^{-6}/K$) ^b	4.2	5.6	3.8
thermal expansion along c ($10^{-6}/K$) ^b	5.3	3.2	2.9
E_g (eV) at T = 0 K	6.25	3.51	0.69 ^c
Varshni parameter α (meV/K)	1.799	0.909	0.414 ^c
Varshni parameter β (K)	1462	830	454 ^c
Δ_{cr} (meV)	-169	10	40
Δ_{so} (meV)	19	17	5
electron effective mass m_e^*/m_0	0.32	0.20	0.07

^aRef. [16], ^bRef. [17], ^cRef. [18]

2.2.2 Band Structure and bulk optical properties

All III-nitride compounds in wurtzite phase have a direct bandgap, *i.e.* the minimum of the conduction band and the maximum of the valence band are both at the Γ point of the Brillouin zone (at $\mathbf{k} = 0$). The values of the band to band energy gaps (denoted E_g) are given in table 2.1. As can be noticed, the E_g values for those materials cover a wide range of energy from 0.69 eV for InN to 6.25 eV for AlN. As a consequence, they exhibit large conduction band offsets (CBO), up to 1.75 eV for AlN/GaN heterostructures, which makes them quite interesting candidates for ISB applications, particularly in the near infrared region. Fig. 2.2 reports the band alignments for different semiconductors. To compare with other materials, Fig. 2.3 displays the bandgap energies and lattice constants of III-nitrides together with usual semiconductors.

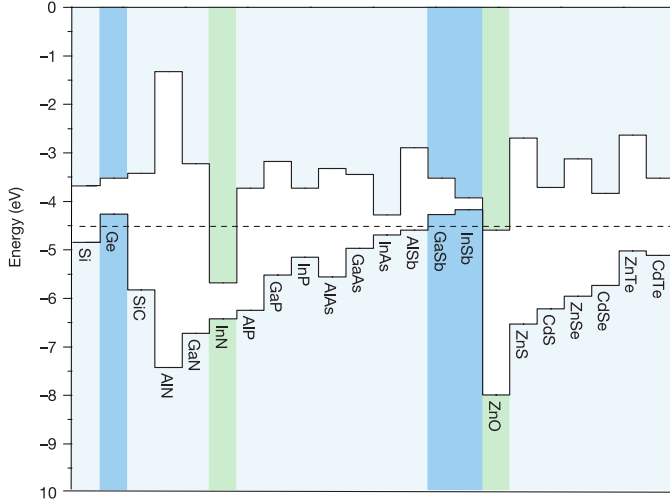


Figure 2.2 – Diagram of band alignments for different semiconductor materials. Figure adapted from Ref. [19].

The bandgap energies of ternary alloys are calculated following a modified Vegard's law (Eq. 2.1), in which a quadratic deviation is introduced by adding a bowing parameter b :

$$E_g(A_xB_{1-x}N) = xE_g(AN) + (1-x)E_g(BN) - bx(1-x). \quad (2.2)$$

The bowing parameters used for this work are 0.7 eV for AlGaN and 1.4 eV for InGaN [15]. The temperature variation of the bandgap is calculated following the empirical Varshni equation [20] :

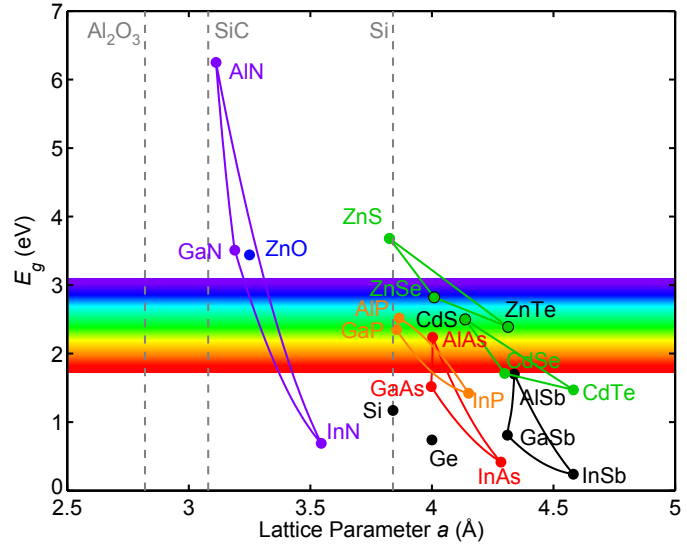
$$E_g(T) = E_g(0) - \frac{\alpha T^2}{\beta + T}, \quad (2.3)$$

where α and β are the Varshni parameters, and $E_g(0)$ the bandgap energy value at 0 K, which are given in table 2.1.

The detailed band structure of GaN is given on Fig. 2.4(a). Due to the anisotropic crystal field in wurtzite structures (Δ_{cr}), and to the spin-orbit interactions (Δ_{so}), the 3-fold degeneracy is lifted, resulting in three bands around $\mathbf{k} = 0$. Those bands are usually called A , B and C ,

2.2. Basics properties of GaN and related compounds

Figure 2.3 – Lattice constants and bandgaps of III-nitride together with usual semiconductors. For cubic systems, the a parameter has been divided by $\sqrt{2}$ for easier comparison with the hexagonal parameter. The vertical dashed lines represent the lattice parameters of the standard substrates for GaN growth.



and show respectively Γ_9 , Γ_{7+} and Γ_{7-} symmetry. They are sometimes denoted respectively by hh , lh and so , standing for heavy holes, light holes and spin-orbit bands. However, this denomination, which comes from zinc-blende compounds, is not appropriate here since the hole effective masses in the \mathbf{k}_z direction are almost identical for the A and B bands in GaN. The valence band structure is shown on Fig. 2.4(b-c).

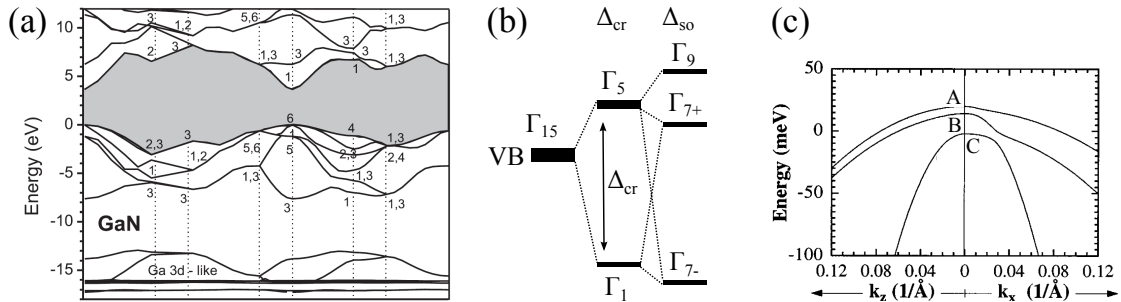


Figure 2.4 – (a) Band structure of GaN reproduced from [21]. (b) Scheme of degeneracy lift of the VB at the Γ point due to crystal field Δ_{cr} and spin-orbit interactions Δ_{so} . (c) detailed valence band structure around the Γ point, reproduced from Ref. [22].

Those three bands raise three excitonic resonances, as shown on Fig. 2.5, which displays the photoluminescence (PL) and the reflectivity spectra of a high quality GaN layer grown on sapphire. The transitions from the A , B and C bands are observed.

In addition, it should be noticed that the large lattice mismatches between usual substrates and GaN, plus the lattice mismatches among the different III-nitride materials induce a significant strain in the layers. It results in a modification of the band structure. Therefore, one has to take into account the deformation potentials to coherently calculate the band structure. Ref. [22] details the $\mathbf{k} \cdot \mathbf{p}$ method for strained materials. Other important consequences of

strain are explained further in this chapter.

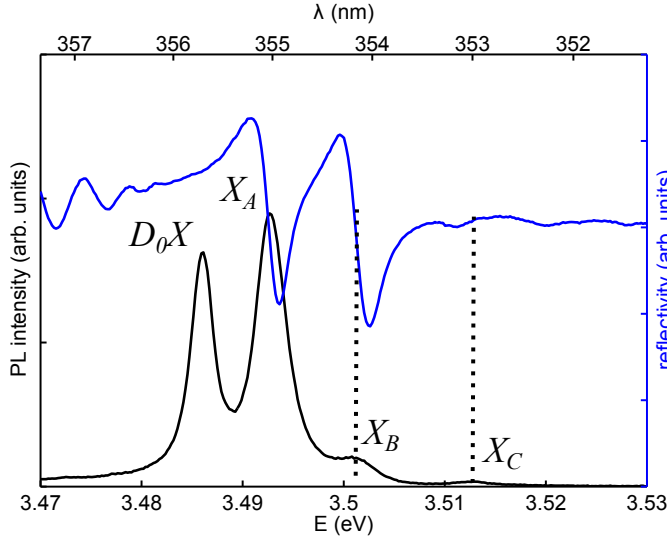


Figure 2.5 – Photoluminescence and reflectivity spectra at 10 K of a 2.5 μm thick GaN layer on sapphire grown by MOVPE. The intrinsic A, B and C excitons are resolved. The D^0X observed on the PL spectrum corresponds to neutral donor bound excitons (noted sometimes I_2).

2.2.3 Mechanical properties and polarization fields

Deformation under a biaxial strain

The large lattice mismatches between GaN and usual substrates, plus between the different III-nitride compounds, induce strains in the epitaxial layers. The deformation of any lattice vector \mathbf{a} is calculated *via* the strain tensor ϵ as follows (using the Einstein summation notations):

$$\mathbf{a}'_i - \mathbf{a}_i = \epsilon_{ij} \mathbf{a}_j, \quad (2.4)$$

where \mathbf{a}' is the deformed vector and \mathbf{a} is the original vector; i and j are the cartesian coordinates $\{x, y, z\}$. ϵ is a symmetric tensor. The diagonal terms ϵ_{ii} correspond to the hydrostatic strain, whereas the off-diagonal terms (ϵ_{ij} with $i \neq j$) correspond to shear strain. Positive (resp. negative) value of ϵ corresponds to a tensile (resp. compressive) strain. The strain tensor is related to the stress tensor σ , which in a way expresses the internal forces in the material, *via* the the elasticity compliance 4th rank tensor C :

$$\sigma_{ij} = C_{ijkl} \epsilon_{kl}. \quad (2.5)$$

2.2. Basics properties of GaN and related compounds

Using the Voigt condensed notation, and accounting the C_{6v} symmetry of the wurtzite structure, this equation can be rewritten:

$$\begin{pmatrix} \sigma_{xx} \\ \sigma_{yy} \\ \sigma_{zz} \\ \sigma_{yz} \\ \sigma_{xz} \\ \sigma_{xy} \end{pmatrix} = \begin{pmatrix} C_{11} & C_{12} & C_{13} & 0 & 0 & 0 \\ C_{12} & C_{11} & C_{13} & 0 & 0 & 0 \\ C_{13} & C_{13} & C_{33} & 0 & 0 & 0 \\ 0 & 0 & 0 & C_{44} & 0 & 0 \\ 0 & 0 & 0 & 0 & C_{44} & 0 \\ 0 & 0 & 0 & 0 & 0 & \frac{1}{2}(C_{11} - C_{12}) \end{pmatrix} \cdot \begin{pmatrix} \epsilon_{xx} \\ \epsilon_{yy} \\ \epsilon_{zz} \\ \epsilon_{yz} \\ \epsilon_{xz} \\ \epsilon_{xy} \end{pmatrix}. \quad (2.6)$$

Thanks to the crystal symmetries, the elasticity tensor is completely given by five parameters: C_{11} , C_{12} , C_{13} , C_{33} and C_{44} , that are given in table 2.2.

Table 2.2 – Elasticity, spontaneous polarization and piezoelectricity coefficients of III-nitride binary compounds. Parameters are taken from Ref. [15], except for spontaneous polarizations, which are taken from Ref. [23].

Parameter	AlN	GaN	InN
C_{11} (GPa)	396	390	223
C_{12} (GPa)	137	145	115
C_{13} (GPa)	108	106	92
C_{33} (GPa)	373	398	224
C_{44} (GPa)	116	105	48
P^{sp} (C/m ²)	-0.090	-0.034	-0.042
d_{15} (pm/V)	3.6	3.1	5.5
d_{13} (pm/V)	-2.1	-1.6	-3.5
d_{33} (pm/V)	5.4	3.1	7.6

If one only considers materials grown on c -plane, the structure is under biaxial strain, and the deformation coefficients become:

$$\epsilon_{xx} = \epsilon_{yy} = \frac{a - a_0}{a_0}, \quad (2.7)$$

where a and a_0 are respectively the lattice constants of the strained and relaxed material. In case of coherent heteroepitaxial growth of GaN, the layers adapt to the substrate in such a way that $a = a_{\text{substrate}}$ and $a_0 = a_{\text{GaN}}$. Besides, the material is free along z direction so that $\sigma_{zz} = 0$. Thus, the deformation along z is easily calculated:

$$\begin{aligned} 0 = \sigma_{zz} &= C_{13}\epsilon_{xx} + C_{13}\epsilon_{yy} + C_{33}\epsilon_{zz} \\ \Leftrightarrow \epsilon_{zz} &= -\frac{2C_{13}}{C_{33}}\epsilon_{xx}. \end{aligned} \quad (2.8)$$

This equation is used to calculate the c lattice parameter, knowing the deformation along

the a parameter. The negative (resp. positive) sign indicates that, if the material is under compressive (resp. tensile) strain, the cell extends (resp. retracts) along the z axis, inducing an increase (resp. decrease) of the polarization field. Those aspects are discussed in the next two paragraphs.

In most of the calculations carried out in this work, a pseudomorphic growth is assumed (*i.e.* all the layers are strained to the substrate). However, this assumption is not always realistic depending on the structure and the substrate. Due to these deformations, the material has to store elastic energy. Above a certain thickness (called the critical thickness), it will be energetically more favourable to relax the elastic energy through plastic deformation by creating dislocations or cracks. More details regarding critical thickness calculation can be found in Ref. [24]. This has to be taken into account for growth optimization to avoid relaxation or formation of cracks.

Spontaneous polarization

As mentioned before, the wurtzite phase corresponds to a polar non-centrosymmetric system, *i.e.* the barycenters of the positive and negative charges do not coincide. This results in a spontaneous polarization along the c -axis (polarization parallel to [0001]). Bernardini *et al.* have calculated *ab initio* the spontaneous polarization [23]. The values are reported on table 2.2. For ternary alloys, the bowing parameters have been calculated as well [25], and the spontaneous polarizations are:

$$\begin{aligned}
 P^{sp}(\text{Al}_x\text{Ga}_{1-x}\text{N}) &= 0.090x - 0.034(1-x) + 0.019x(1-x) \\
 P^{sp}(\text{In}_x\text{Ga}_{1-x}\text{N}) &= -0.042x - 0.034x + 0.038x(1-x) \\
 P^{sp}(\text{In}_x\text{Al}_{1-x}\text{N}) &= -0.042x - 0.090(1-x) + 0.071x(1-x),
 \end{aligned} \tag{2.9}$$

where P^{sp} is the spontaneous polarization in C/m^2 . A schematic representation of the spontaneous polarization is presented on Fig. 2.6(a).

Piezoelectric polarization

In addition to the spontaneous polarization, wurtzite materials are piezoelectric, meaning that *i.e.* stress induces an additional polarization. The relation between the stress tensor and the piezoelectric polarization vector is given by the direct piezoelectric tensor d (3rd rank):

$$P_i^{pz} = d_{ijk}\sigma_{jk}. \tag{2.10}$$

2.2. Basics properties of GaN and related compounds

Using the Voigt notations and accounting for the crystal symmetries, this relation becomes:

$$\begin{pmatrix} P_x^{pz} \\ P_y^{pz} \\ P_z^{pz} \end{pmatrix} = \begin{pmatrix} 0 & 0 & 0 & 0 & d_{15} & 0 \\ 0 & 0 & 0 & d_{15} & 0 & 0 \\ d_{13} & d_{13} & d_{33} & 0 & 0 & 0 \end{pmatrix} \begin{pmatrix} \sigma_{xx} \\ \sigma_{yy} \\ \sigma_{zz} \\ \sigma_{yz} \\ \sigma_{xz} \\ \sigma_{xy} \end{pmatrix}, \quad (2.11)$$

where d_{ij} are the piezoelectric coefficients that are given in table 2.2. They are sometimes replaced by the e_{ij} coefficients, that relate the piezoelectricity polarization with the strain tensor. Using the relation given in Eq. (2.5), those two tensors are linked *via* the elasticity compliance tensor:

$$P_i^{pz} = d_{ijk}\sigma_{jk} = d_{ijk}C_{jklm}\epsilon_{lm} = e_{ilm}\sigma_{lm} \quad \text{with} \quad e_{ilm} = d_{ijk}C_{jklm}. \quad (2.12)$$

The e coefficients have the same units as the polarization (C/m²). If one only considers a biaxial strain along the xy plan, \mathbf{P}^{pz} simply becomes:

$$P_z^{pz} = 2d_{13}\sigma_{xx} = 2d_{13}\left(C_{11} + C_{12} - \frac{2C_{13}^2}{C_{33}}\right)\epsilon_{xx}. \quad (2.13)$$

A schematic representation of piezoelectricity in the wurtzite cell is given in Fig. 2.6.

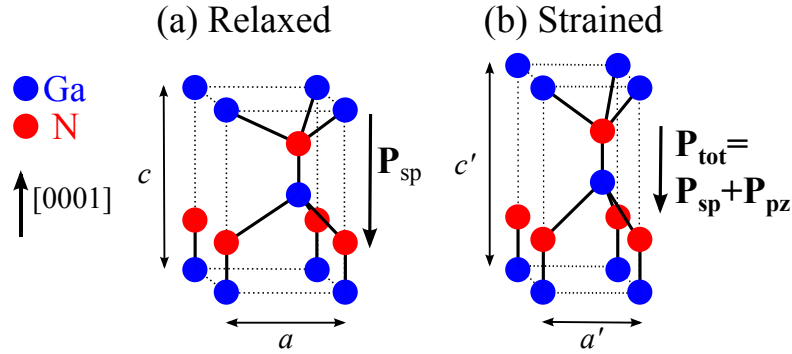


Figure 2.6– representation of the wurtzite cell and the polarization vectors in the unstrained (a) and the compressively strained (b) cases. For layers under compressive strain, the piezoelectric polarization is opposite to the spontaneous one, inducing a lower total polarization. In the case of tensile strain, spontaneous and piezoelectric polarization have the same direction

As it will be demonstrated later in this chapter, both spontaneous and piezoelectric polarization have significant effects on optical properties (ISB and interband) of III-nitride based heterostructures. Indeed, the polarization discontinuity at the interface of a heterojunction will create an electric field having values up to several MV/cm.

2.3 Epitaxy and structural characterization

The three main growth techniques for III-nitride semiconductors are molecular beam epitaxy (MBE), metal-organic vapour phase epitaxy (MOVPE), and hydride vapour phase epitaxy (HVPE). The latest is mostly used to grow thick layers or templates since it allows for very high growth rates, up to few hundreds of $\mu\text{m}/\text{h}$, but it has a lower thickness accuracy, and is not suited for InGaN growth neither p-type doping. This technique will not be detailed in this manuscript, as all samples that are studied in this work are either MOVPE or MBE grown. Before dealing with the details of epitaxy techniques, it is important to have an overview of the different existing substrates that are used for GaN and related compounds. Indeed, the choice of the substrate strongly influences the quality of the epitaxial layer, and one has thus to adapt the growth recipes.

2.3.1 Substrates and relative lattice mismatch

As mentioned earlier, III-nitride compounds have first been grown on foreign substrates with large lattice mismatch. The latter is defined as follows:

$$\frac{\Delta a}{a} = \frac{a_{\text{GaN}} - a_{\text{substrate}}}{a_{\text{substrate}}},$$

and the values are -17% for Si, $+12.9\%$ for sapphire and $+3.5\%$ for SiC. Those large mismatches induce detrimental effects on the crystalline quality (high dislocation density). Besides, those foreign substrates exhibit different thermal expansion coefficients with respect to GaN, inducing a residual strain when cooling down the sample after growth. The lack of suitable substrates in terms of lattice mismatch and thermal expansion coefficient, is the main reason why progress in III-nitride research went slow in the 70s and 80s.

GaN bulk or free standing (FS) substrates are commercially available and are getting more and more affordable (but with much higher costs than sapphire or silicon). They have a low dislocation density, down to $5 \times 10^3 \text{ cm}^{-2}$ for bulk [26], but most generally around 10^6 cm^{-2} for FS substrates. Besides the obvious advantages of homoepitaxy (no lattice mismatch and same thermal expansion), these substrates offer a good electrical and thermal conductivity, thanks to their heavily n-type doping levels. This allows for instance to deposit the n-type contacts of blue LEDs or LDs on the substrate backside. However, when going to far infrared (FIR) ISB optoelectronic devices, they are less suitable due to free carriers absorption that makes them non transparent at those wavelengths.

Today, the most widely used substrates are sapphire for LEDs or FS GaN for lasers. Both are the mainly used substrates in this work. Quantum cascade detectors (QCDs) are mostly grown on commercial AlN template on sapphire, or on home-made MOVPE GaN templates on sapphire,

whereas resonant tunneling diodes (RTDs) in this thesis are mainly grown on by MOVPE on commercial FS GaN substrates.

2.3.2 Molecular beam epitaxy

Principles of MBE:

MBE is an ultra high vacuum physical deposition technique: the residual pressure in the growth chamber is around 10^{-10} mbar or lower. This is necessary to avoid incorporation of impurities and to have a long enough mean free path to allow the atomic species reaching the sample surface without any interaction. The substrate is heated with a filament to the growth temperature T_g , which is monitored and calibrated with a pyrometer. It measures the light power (P) emitted from the sample, according to Stefan-Boltzmann law, which results from of the blackbody radiation theory:

$$P = A\epsilon\sigma T^4, \quad (2.14)$$

where A is the probed surface of the sample, ϵ the emissivity of the sample ($\epsilon \leq 1$), σ the Stefan-Boltzmann constant, and T the temperature of the substrate.

Historically, quantum heterostructures grown by MBE were first demonstrated in the late 60s by A. Cho and coworkers at the Bell Laboratories. For more details, see Ref. [27] and references therein.

Figure 2.7 – Schematic representation of a MBE reactor for III-nitride growth.

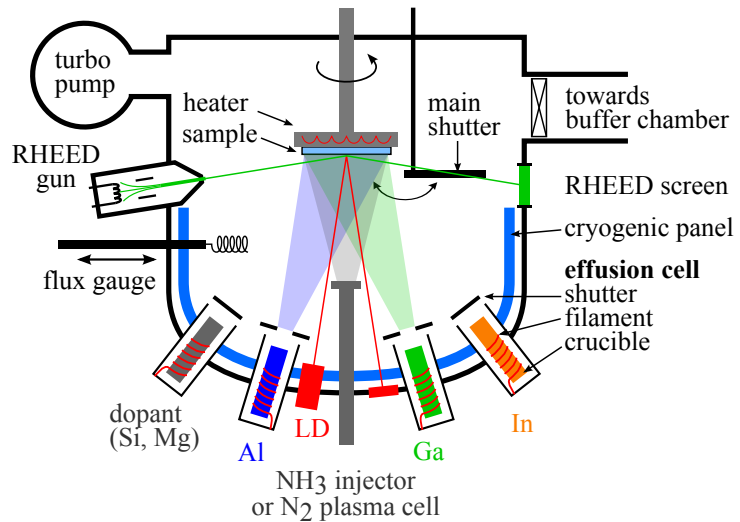


Fig. 2.7 presents a sketch of an MBE reactor. The pressure inside the growth chamber is monitored by a Bayard-Alpert gauge. To enhance the vacuum, the walls of the reactors are cooled with liquid nitrogen. The metal elements (Al, Ga, In) and dopants (Si, Mg) are supplied by Knudsen effusion cells, which are composed of a pyrolytic boron nitride or graphite (both are refractory materials) crucible containing the materials to evaporate or sublimate. Around this crucible a tantalum filament is used to heat the source. The temperature can vary between

Chapter 2. Basics on III-nitride semiconductors and intersubband transitions

400° C to 1300° C depending on the material and the desired flux, and is controlled *via* a thermocouple. Each cell can be open or closed by the shutter triggered by a computer. The atomic fluxes from the effusion cells can be calibrated with a Bayard-Alpert gauge, named the flux gauge. Every few months, the reactor chamber has to be opened to refill the cells. Following this opening, the reactor chamber has to be baked out up to 250° C for several days, to get rid of residual gaseous water, which is the main source of contaminations.

There are two ways to provide the nitrogen species (V-element): ammonia (NH₃-MBE) that is directly cracked on the sample surface, or nitrogen (N₂) which is decomposed in atomic nitrogen by a RF plasma cell (PA-MBE). Those two techniques are quite different: the standard growth conditions are nitrogen-rich for NH₃-MBE and metal-rich for PA-MBE. Also, the growth temperatures are usually higher with ammonia, to ensure efficient NH₃ cracking. Moreover, ammonia growth allows achieving higher deposition rates (up to 1 μm/h), while N₂-plasma standard growth rate is around 0.3 μm/h. However, recent progress in plasma sources enable nowadays growth rates of few μm/h with PA-MBE [28].

The system used for this work is a Riber compact 21 (see picture of the reactor on Fig. 2.8) designed for both ammonia and plasma sources. However, the system is mainly used with ammonia source. All MBE grown samples presented in this manuscript have been grown with ammonia. During the growth, a large amount of ammonia is trapped by the cryogenic panel, which increases the residual pressure in the chamber. The latter has thus to be regenerated every week. For this operation, the cooling nitrogen is stopped and the reactor chamber is heated to ~ 100° C for approximately 24 hours. During this process, the chamber pressure can increase up to few mbar due to NH₃ desorption.

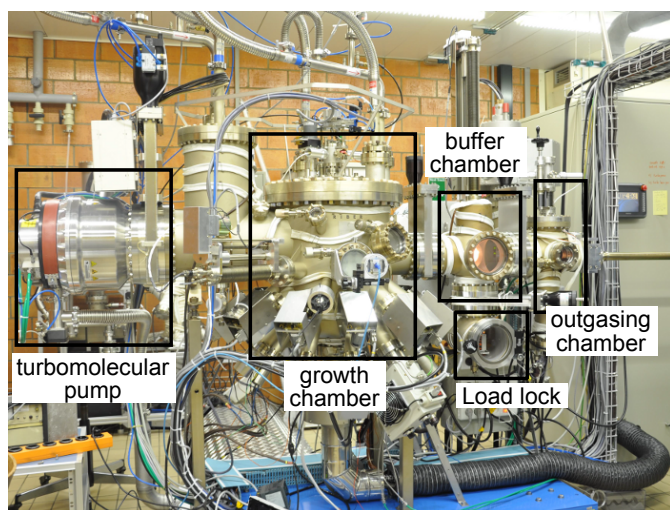


Figure 2.8 – photo of the RIBER Compact 21 MBE reactor used for this work

Concerning the substrates, they are held by a molybdenum block having 4” diameter, which are machined to hold substrates of different sizes. A filament heats up the substrate at temperatures up to 1000° C. Transparent substrates like sapphire have to be the back-side coated

with molybdenum or titanium to ensure absorption, and to enable temperature monitoring with the pyrometer.

The standard growth conditions with NH_3 -MBE for GaN are the following: substrate temperature is $\sim 800^\circ\text{C}$ ($\sim 900^\circ\text{C}$ for AlN) and the ammonia flux is around 80 sccm. The growth rate is monitored *via* reflectivity measurements with a red LD (Fig. 2.7). One period in the reflectivity oscillation corresponds to a thickness of:

$$t = \frac{\lambda \cos \theta}{2n}, \quad (2.15)$$

where n is optical index of GaN, λ the wavelength of the LD and θ the incidence angle. In our system, one period corresponds to 142 nm. Besides it should be noticed that reflectivity measurements requires an index contrast between the epitaxied layer and the substrate. The growth rates can be measured more precisely by reflexion high energy electron diffraction (RHEED), which is the subject of the next paragraph. Usually both methods are combined: RHEED calibrations are performed prior to the growth and the reflectivity is used during the deposition.

Growth rate calibration *via* RHEED oscillations:

One of the advantages of MBE over MOVPE, is the accurate *in situ* growth rate control using calibrations *via* RHEED oscillations. This is highly beneficial to grow complex heterostructures used for ISB devices that can contain several hundreds of QWs. This is an electron diffraction technique at grazing incidence, which gives precious information about the sample surface: it indicates the surface morphology (2D or 3D growth), the in-plane lattice parameter, or the surface reconstruction. This is for instance useful when growing GaN on Si [111] substrate to monitored the 7×7 surface reconstruction. Fig. 2.9 shows photographs of RHEED patterns of GaN layers. The streaky pattern corresponds to a smooth surface (2D surface morphology). The second image shows a 3D surface morphology, typical for quantum dots for instance. More interestingly, this tool provides a direct way to measure the growth rate at the monolayer (ML) scale thanks to RHEED oscillations (Fig. 2.10). An example of measured RHEED oscillations during GaN growth is shown on Fig. 2.11. Calibration *via* RHEED oscillations is performed prior to every growth of ISB device. A camera is recording the spot intensity in real time. Each oscillation maximum corresponds to the completion of a ML at the scale of the coherence length of the electron beam. The inverse of the oscillation period gives directly the growth rate in ML/s. To observe the RHEED oscillations in NH_3 -MBE, the temperature should be set to $\sim 600^\circ\text{C}$, *i.e.* $\sim 200^\circ\text{C}$ lower than the usual growth temperature. The reason is that 800°C corresponds to mean step-flow growth mode conditions, which means that the adatoms will nucleate preferentially at the step edges, making the RHEED oscillations difficult to be observed, and giving anyway wrong growth rate. 600°C corresponds to the pure 2D nucleation

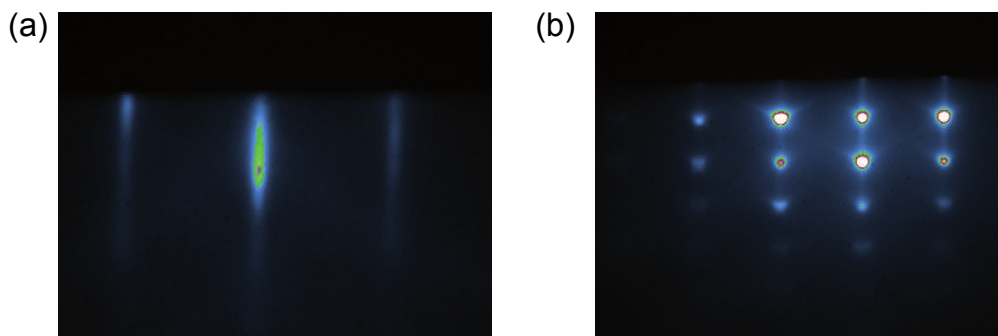


Figure 2.9 – RHEED pattern of a GaN layer patterns exhibiting 2D (a) and 3D (b) surface morphology.

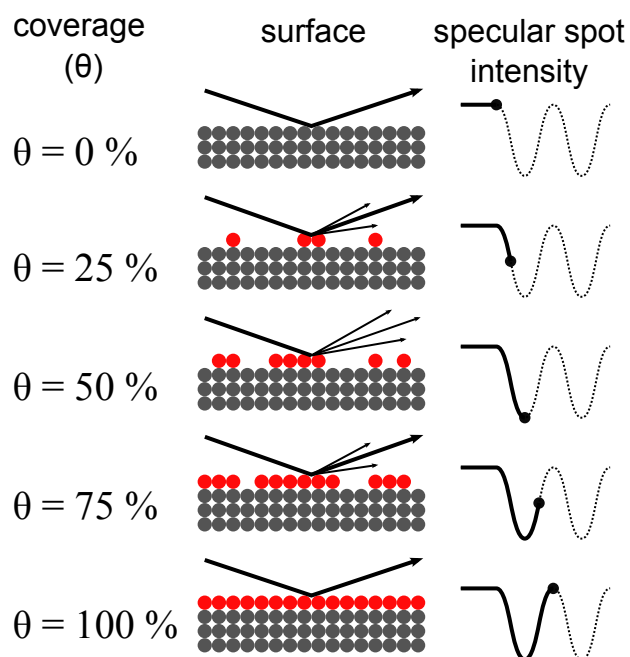


Figure 2.10 – Schematics of RHEED oscillations: the specular beam intensity depends on the roughness of the surface, being maximal for a complete layer and minimal at half coverage.

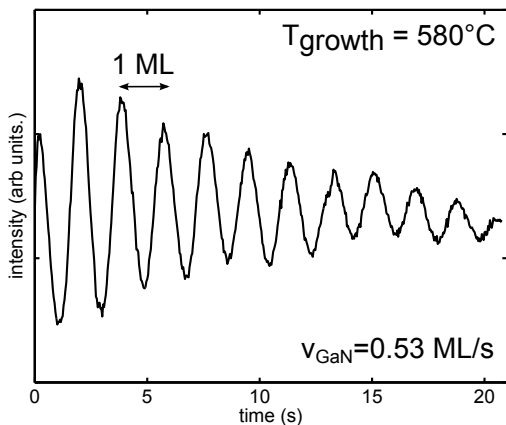


Figure 2.11 – RHEED oscillations recorded during GaN growth. The temperature is set to 580°C to ensure a nucleation growth mode. The pseudo-period of the oscillation (equal to the inverse growth speed in ML/s) is 1.89 s.

growth mode [29]. However the actual growth rates remain unchanged, thanks to the sticking coefficients equal to 1 for Al and Ga (note that this is not the case for In), as long as the NH_3 flux is high enough and the growth temperature not higher than 870°C , where Ga desorption is not negligible anymore. To extract the AlN deposition rate, a first measurement is done with only GaN, then a second is done with AlGaN. The following formula gives the AlN growth rate:

$$v_{\text{AlN}} = v_{\text{AlGaN}} - v_{\text{GaN}}. \quad (2.16)$$

The Al content is then given by:

$$x_{\text{Al}} = \frac{v_{\text{AlN}}}{v_{\text{AlGaN}}} \quad (2.17)$$

Generally, the Ga flux is fixed, and the temperature of the Al cell is set to get the proper growth rate which is given by the Arrhenius law:

$$v_{\text{AlN}}(T) = v_{\text{AlN}}^0 e^{-E_a/k_B T}, \quad (2.18)$$

where E_a is the evaporation (or sublimation) activation energy. The typical growth rate for GaN is around 1 ML/s.

Some advantages of ammonia-source compared to plasma-source MBE are for instance the convenient calibration *via* RHEED oscillations, and usually a higher growth rate achieved with ammonia. Moreover NH_3 -MBE uses a higher growth temperature which is closer to equilibrium and should result in less impurity incorporations. On the other hand, PA-MBE is known to achieve sharper interfaces thanks to the low growth temperatures.

2.3.3 Metal-organic vapour phase epitaxy (MOVPE)

The other growth method used in this work is MOVPE. It is a chemical vapour deposition technique. The III-elements are supplied from organometallic precursors, which are contained in thermostated bubblers. They are mixed with a carrier gas (N_2 or H_2) and directed through gaslines towards the substrate. The precursors are trimethyl-gallium (TMGa) or triethyl-gallium (TEGa) for Gallium, trimethyl-aluminium (TMAI) for aluminium and trimethyl-indium (TMIn) for indium. They are mixed with ammonia, which provides the nitrogen, in the growth chamber and chemically react at the sample surface. The dopant elements are provided by bis-cyclopentadieny-magnesium (Cp_2Mg) for magnesium and silane (SiH_4) for silicon. The growth occurs in nitrogen rich conditions. The sample is heated by a graphite susceptor and the growth temperatures vary between 700°C and 1200°C . The growth rate is monitored *in situ via* laser reflectivity measurements. Two MOVPE reactors were used for this work, an Aixtron 200/4 RF-S $1 \times 2''$ (horizontal reactor) and an Aixtron shower-head (vertical reactor) CCS $3 \times 2''$. Fig. 2.12 are photographs of those two reactors.

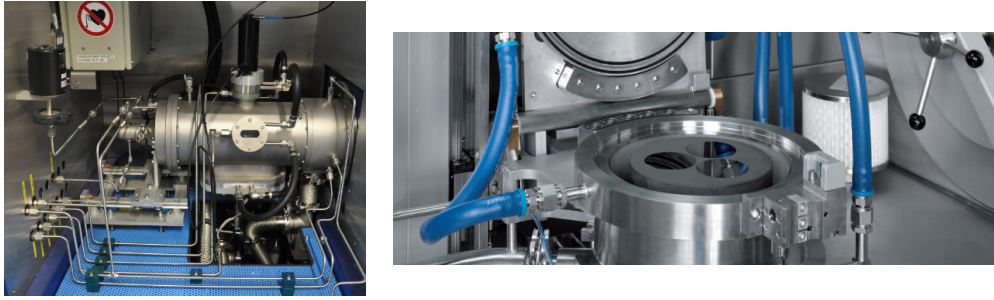


Figure 2.12 – Pictures of the two MOVPE reactors used in this work: (left) the Aixtron 200/4 RF-S $1 \times 2''$ and (right) the Aixtron CCS $3 \times 2''$.

MOVPE is the dominant growth technique for most III-nitride applications, since it gives high growth rates and requires less maintenance than MBE. Besides, the high growth temperature, close to thermodynamic equilibrium, ensures a lower point defect concentration, and overall, better material quality, specially for InGaN alloys. However, MBE is still a favoured technique for complex ISB structures due to the better thickness control and smoother interfaces.

2.3.4 Structural and basic optical characterization

Whatever the growth method, samples are characterized *ex situ* by non destructive methods to assess the quality, and measure the layers thicknesses and compositions.

X-Ray diffraction (XRD): It is a technique consisting in measuring the diffraction of an X-ray beam by the sample. The X-rays are provided by the $K\text{-}\alpha_1$ emission of copper at a wavelength $\lambda = 1.54 \text{ \AA}$, which is small enough to probe the sample at the atomic scale. The crystallographic planes diffract the beam in specific directions. Fig. 2.13 is a representative scheme of an XRD. Measurements are done scanning the Ω and Θ angles. The distance d between two parallel atomic planes (represented in Fig. 2.13(a)) diffracting with a 2Θ angle is given by the Bragg law:

$$n\lambda = 2d \sin\Theta, \quad (2.19)$$

where n is an integer corresponding to the order of diffraction. Analogously in the reciprocal space, a diffraction peak should satisfy the Laue diffraction condition:

$$\mathbf{k}_f - \mathbf{k}_i = \mathbf{Q}, \quad (2.20)$$

where \mathbf{Q} is a vector of the reciprocal lattice, \mathbf{k}_i and \mathbf{k}_f the incident and diffracted wave vectors of the X-ray beam.

For instance, the Θ angle corresponding to the (0002) reflection gives the c parameter of the different layers of the structure, and allows the determination of the alloy compositions. XRD is

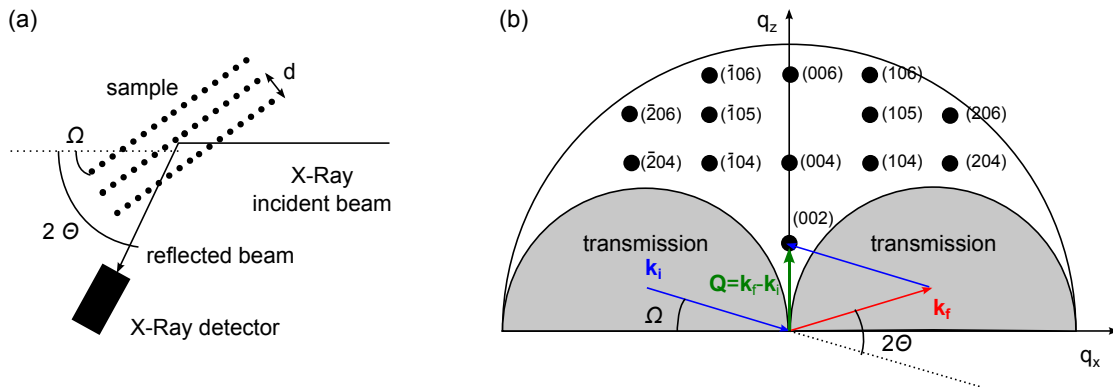


Figure 2.13 – Schematics of XRD principle in the (a) real and (b) reciprocal spaces, where the ω and θ angles are represented. In (b) are represented the accessible reflections for GaN with a (0001) surface orientation and (10 $\bar{1}$ 0) azimuth are represented. For the sake of clarity, the i index of the $(hki l)$ notations is omitted.

a very useful tool to characterize complex heterostructures: for superlattices (SL), $2\theta - \Omega$ scans enable the determination of the SL period. For thick layers, the broadening of the Ω scan (also called rocking curve) is an important figure of merit to assess the material quality. Recently, our institute acquired a Bruker Discovery D8 instrument, which allows reciprocal space mappings. Then, both c and a parameter can be quantitatively measured, using asymmetric reflections ([10 $\bar{1}$ 5] for instance). The relaxation and alloy content can then be determined independently. Besides, this instrument is provided with powerful analysis softwares. For more details, a review on XRD on III-nitride structures can be found in Ref. [30].

Atomic force microscopy (AFM): This method consists of scanning the surface sample with an ultra-sharp tip (the curvature radius at the end of the tip is around 10 nm). Since the tip is very close to the surface, it is sensitive to atomic forces. It results that a slight height change of the surface induces a deflection of the cantilever measured by laser reflection. It allows precise height measurements at the subnanometer scale. It gives information about the surface morphology and the roughness. Threading dislocations can also be imaged. The measurements were performed on a Digital Instruments nanoscope AFM.

Optical spectroscopy: The most used spectroscopy techniques are photoluminescence (PL) and reflectivity. The first one consists of measuring the emission spectrum of a sample excited with a UV laser source having a higher energy than the bandgap of the semiconductor. The main excitation sources were a continuous wave (cw) He-Cd laser emitting at 325 nm, and a cw frequency double Ar laser, emitting at 244 nm. This laser pump excites carriers in the layer (transfer of electrons from the valence band to the conduction band), which then relax *via* different mechanisms. Some of those mechanisms are radiative and give a luminescence

signal, which is collected with a spectrometer. The sample can be placed in a cryostat to perform measurements at low temperatures.

PL is a powerful tool. For thick layers, the linewidth of the emission assesses the quality of the sample. Ref. [31] presents low temperature PL and reflectivity measurements on high quality homoepitaxial GaN layers. For instance, PL spectroscopy on QWs provides information about the confinements energies, which is related to the QW thickness. One can also estimate the disorder in a single or multi QW structure, such as alloy broadening or interfaces disorder, which is closely linked to the emission linewidth at low temperature. Moreover, temperature dependent studies give information about energies of the localized states [32].

In addition to PL spectroscopy, reflectivity provides useful complementary information. It consists in measuring the reflection of a white lamp spectrum from the sample. The reflectivity signal contains the excitonic resonance of the probed material. Cross-linked with PL spectrum, one can determine the origin of a PL peak, since localized state will not give rise to a reflectivity signal.

2.4 III-nitride MQWS properties and band structure calculations

2.4.1 Polarization fields in the structures: quantum confined Stark Effect

Calculation of the internal electric field

As already mentioned, GaN is a polar material, meaning that it exhibits an internal polarization. If the polarization does not exist in thick layer, as the electric fields are screened by mobile charges, the consequences in nanoscale heterostructures are much more dramatic. Indeed, discontinuity in polarization has the same effect as charged interface.

The electrostatic displacement vector \mathbf{D} is given by the following formula:

$$\mathbf{D} = \epsilon_0 \epsilon_r \mathbf{F} + \mathbf{P}, \quad (2.21)$$

where ϵ_0 is the vacuum permittivity ($\epsilon_0 \simeq 8.854 \times 10^{-12}$ F/m), ϵ_r is the relative dielectric constant, \mathbf{F} is the static electric field and \mathbf{P} is the polarization (spontaneous plus piezoelectric) vector. For anisotropic materials, as it is the case for wurtzite phase III-nitrides, the dielectric constant becomes the dielectric tensor (2nd rank tensor), which has the following form for the hexagonal symmetry:

$$\epsilon_r = \begin{pmatrix} \epsilon_{\perp} & 0 & 0 \\ 0 & \epsilon_{\perp} & 0 \\ 0 & 0 & \epsilon_{\parallel} \end{pmatrix}. \quad (2.22)$$

However, for epitaxial layers grown on c-plane, which is the case in this work, all vectors (\mathbf{D} , \mathbf{F} and \mathbf{P}) are along z , so that only ϵ_{\parallel} is important for calculations of the static fields. For

2.4. III-nitride MQWS properties and band structure calculations

simplicity, the indices will be omitted in the following. The usual values for the dielectric constant are 8.57 for AlN, and 10.1 for GaN [33]. The neutrality of the medium ensures that $\nabla \cdot \mathbf{D} = 0$, which means that the displacement vector should remain constant across all the layers of the structure. From Eq. (2.21), one can deduce the electric field in a single QW, with infinite barriers:

$$F_w^{SQW} = \frac{P_b - P_w}{\epsilon_0 \epsilon_r} = \frac{\Delta P}{\epsilon_0 \epsilon_r}, \quad (2.23)$$

where the indices b and w stand for the barrier and the well. ΔP is the polarization difference:

$$\Delta P = (P_b^{sp} + P_b^{pz}) - (P_w^{sp} - P_w^{pz}). \quad (2.24)$$

For GaN SQW with AlN barrier, the computed electric field is as high as 10 MV/cm. In the case of a MQW structure, the electric field is distributed in the barriers and QWs. If the periodic conditions are assumed for the electric potential over a period, the following condition is fulfilled:

$$t_b F_b + t_w F_w = 0. \quad (2.25)$$

Together with the continuity equation of the displacement vector:

$$\epsilon_0 \epsilon_b F_b + P_b = \epsilon_0 \epsilon_w F_w + P_w, \quad (2.26)$$

it results in:

$$F_w^{MQW} = \frac{\Delta P}{\epsilon_0} \frac{t_b}{\epsilon_w t_b + \epsilon_b t_w}. \quad (2.27)$$

With the approximation $\epsilon_b \simeq \epsilon_w$, the previous expression can be simply written:

$$F_w^{MQW} = F_w^{SQW} \frac{t_b}{t_b + t_w} \quad \text{and} \quad F_b^{MQW} = -F_w^{SQW} \frac{t_w}{t_b + t_w}. \quad (2.28)$$

For ISB dedicated samples, such as QCDs, the heterostructures are much more complex and contains generally a large number of QWs (up to 500 for some samples grown for this work) that have different barrier or well thicknesses, and different barrier height. Then, neglecting the effect of charge screening, the formula of the electric field in any layer indexed by i becomes:

$$F_i = \frac{\sum_{k \neq i} (P_k - P_i) l_k / \epsilon_k}{\epsilon_i \sum_k l_k / \epsilon_k}. \quad (2.29)$$

It should be noted that the previously presented calculation does not take into account the converse piezoelectric effect, *i.e.* the electric field induces strain, in addition to the elastic compliance (*cf.* Eq. 2.5). The presented model, also known as the *uncoupled* model, is common and induces a deviation of around 2 % from the *coupled* model [34].

Besides, one should notice that all the previous calculations assume that there are no free

charges in the materials. This would be the case for an ideally undoped material. However, residual doping is usually high enough (generally higher than 10^{16} cm^{-3}) to create free charges. Depending on the sign of the polarization discontinuity, those free charges will be accumulated or depleted at the interfaces, inducing a screening effect of the static electric field. To predict accurately the potential profile, the potential should be computed self-consistently with the Schrödinger-Poisson model. The method will be described later in this chapter.

Effects of the electric field on QWs

The presence of an electric field in a quantum structure induces a red-shift of the interband transition. This is called the quantum confined Stark effect (QCSE). The electric field can be either external or internal (from the piezoelectric and the spontaneous polarization). The QCSE was first reported by Miller *et al.* on GaAs [35] QWs under an external electric field. Fig. 2.14 (a-b) represents the band structure with and without polarization of a 3 nm thick GaN QW in AlN barriers. For an electric field value F and a QW thickness t_{QW} , this energy can be written as:

$$\hbar\omega = E_g + E_e^{conf} + E_h^{conf} - E_X^b - qt_{QW}F, \tag{2.30}$$

where E_g is the bandgap energy, E_e^{conf} and E_h^{conf} are the confinement energies of electrons and holes in the QW, E_X^b is the exciton binding energy, and q the electron charge. The value of E_X^b can vary between 10 and 50 meV depending on the electric field and the well thickness. For a large enough QW, the QW transition energy becomes lower than the bandgap (see Fig.2.14(c)). QCSE has been experimentally observed in AlGaIn/GaN QWs [36].

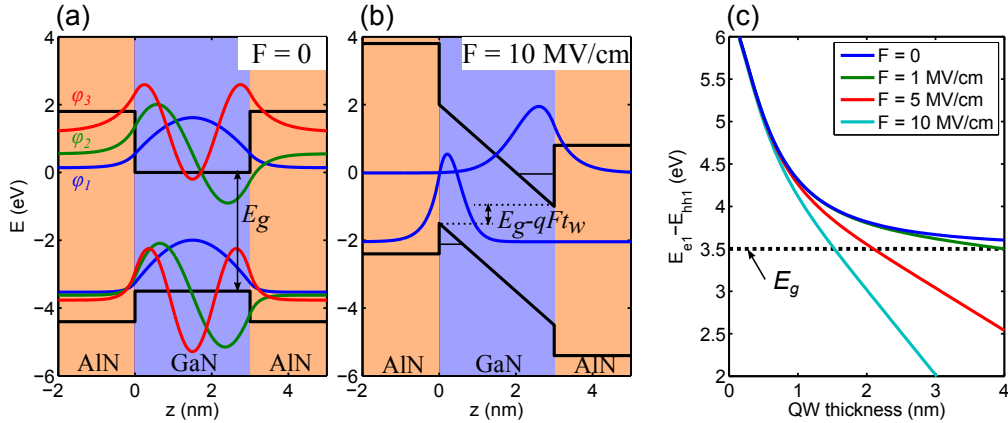


Figure 2.14 – **Effects of internal electric field:** band structure of a 3 nm GaN QW in AlN without (a) and with (b) an electric field of 10 MV/cm. (c) Evolution of the interband transition with the QW thickness for different values of the electrical field; the horizontal line represents the bandgap of GaN.

Another important consequence of the electric field is the spatial separation of the electron and hole envelope wave functions in the QW, as depicted in Fig. 2.14(b). As it will be demonstrated

2.4. III-nitride MQWS properties and band structure calculations

later in this chapter, the matrix element of the dipole moment for interband transition is proportional to:

$$|\langle \nu | c \rangle|^2 = \left| \int \varphi_e^*(z) \varphi_h(z) dz \right|^2, \quad (2.31)$$

where $\varphi_{e/h}$ are the envelope wave functions for the electrons and holes. It is clear that the spatial separation of the electrons and the holes will lower the value of this matrix element, inducing a lower absorption or emission rate. The radiative life time (τ_r) will be longer, resulting in a lower internal quantum efficiency, since the latter can be expressed as function of the radiative and non radiative recombination life time as:

$$\eta_i = \frac{\tau_{nr}}{\tau_r + \tau_{nr}} \quad (2.32)$$

The internal electric field has also strong impacts on ISB transitions, on both the transition energies and the selection rules. These points will be discussed later.

2.4.2 Effective mass model and non parabolicity effects

To know the energies and wave-functions of one electron in a bulk crystal, one has to solve the following Schrödinger equation:

$$\left[\frac{\mathbf{p}^2}{2m_0} + V(\mathbf{r}) \right] \psi(\mathbf{r}) = \mathcal{E} \psi(\mathbf{r}), \quad (2.33)$$

where $V(\mathbf{r})$ is the crystalline potential, having the same periodicity as the crystal lattice. It includes the coulombic interactions with the nuclei and the mean field potential from the other electrons. In this model, the relativistic terms such as spin-orbit interaction, the many body effects or the interactions with the lattice vibrations are neglected.

Due to the periodicity of the potential, Bloch's theorem states that the solutions of the Schrödinger equation are the Bloch functions which have the following form:

$$\psi(\mathbf{r}) = u_{\mathbf{k}}(\mathbf{r}) e^{-i\mathbf{k}\cdot\mathbf{r}}, \quad (2.34)$$

where $u_{\mathbf{k}}(\mathbf{r})$ are functions that present the same periodicity as the crystal. The Schrödinger equation for Bloch states has to be solved to get the energy dispersion curves $E(\mathbf{k})$ in the first Brillouin zone. Several methods exist, and one of the most popular is the semi-empirical Kane's $\mathbf{k} \cdot \mathbf{p}$ method [37]. Those calculations result in energy bands that are approximately parabolic around the Γ point of the Brillouin zone $\mathbf{k} = 0$. This brings the concept of effective mass. The dispersion is given by the following relation (for an isotropic effective mass):

$$E(\mathbf{k}) = E_n + \frac{\hbar^2}{2m^*} \mathbf{k}^2. \quad (2.35)$$

In this approximation, the electron in the crystalline periodic potential behaves like a free particle having the mass m^* . For a one band $\mathbf{k} \cdot \mathbf{p}$ model, the value is:

$$\frac{m^*}{m_0} = \left(1 + \frac{E_P}{E_g}\right)^{-1}, \quad (2.36)$$

where E_P is called the Kane energy, and its typical values is around 20 meV. However, this model is usually not satisfactory, specially for the calculation of ISB levels. Indeed the high CBO between AlN and GaN induces high enough energy subbands where the parabolic approximation is not applicable. Therefore, a full 8 bands $\mathbf{k} \cdot \mathbf{p}$ model, or a model with non parabolicity corrections (energy dependent effective mass $m^*(E)$) should be used for accurate predictions of the subbands energies. For instance, Ref. [1] gives the following quadratic relation of the electron effective mass in GaN, extracted from the $\mathbf{k} \cdot \mathbf{p}$ model:

$$m^*(E) = 0.22 m_0 (1 + 0.613 E + 0.057 E^2). \quad (2.37)$$

2.4.3 The envelope function approximation

Multiple heterostructures exist in a stacking of different materials having different properties, and particularly different bandgap energies. It results that the conduction and valence band edges at $\mathbf{k} = 0$ are discontinuous across the heterostructure, *i.e.* a discontinuity of the crystalline potential. III-nitrides are always type I heterostructures (*cf.* Fig. 2.2), meaning that the QW, made of the lower bandgap energy material, acts as a confining potential for both electrons and holes. The potential discontinuity for an electron in the conduction band is characterized by the CBO. Its value between GaN and AlN has been experimentally measured by means of ISB spectroscopy and is around 1.75 eV [1]. Therefore, the electron undergoes the crystalline potential $V(\mathbf{r})$ plus the potential of the heterostructure $U(\mathbf{r})$, which takes into account the potential discontinuity at each interface and electric field induced potential for polar structures. Therefore, the Schrödinger equation becomes:

$$\left[\frac{\mathbf{p}^2}{2m_0} + V(\mathbf{r}) + U(\mathbf{r}) \right] \psi(\mathbf{r}) = \mathcal{E} \psi(\mathbf{r}). \quad (2.38)$$

The following paragraph gives the results of the envelope function approximation. The rigorous demonstration is tedious and more details can be found in Ref. [38]. It should be noticed that the main assumption made for the envelope function formalism is that the heterostructure potential $U(\mathbf{r})$ is varying slowly comparing to the crystalline potential $V(\mathbf{r})$, *i.e.* the MQW period should be much longer than the lattice parameter. At $\mathbf{k} = 0$ the eigenstates of Eq. (2.38) can be developed as:

2.4. III-nitride MQWS properties and band structure calculations

$$\psi(\mathbf{r}) = \sum_n u_{n,0}(\mathbf{r}) F_n(\mathbf{r}), \quad (2.39)$$

where $u_{n,0}$ are the periodic parts of the Bloch waves, and $F_n(\mathbf{r})$ is the envelope function of the n^{th} band. For MQW structures, since the confinement is only in the z direction, it results in the following envelope function:

$$F_n(\mathbf{r}) = \frac{1}{S} e^{i\mathbf{k}_{\parallel} \cdot \mathbf{r}_{\parallel}} \varphi_n(z), \quad (2.40)$$

where S is the surface of the heterostructure (along x and y), \mathbf{k}_{\parallel} and \mathbf{r}_{\parallel} are the wave and position vectors in the layer plane. By injecting the wave equation under this form in equation (2.38) and using the effective mass formalism, it follows that the $\varphi(z)$ function is solution of the following equation:

$$\left[-\nabla \frac{\hbar^2}{2m^*(z)} \nabla + U(z) \right] \varphi_n(z) = \left(E - \epsilon_{n0} - \frac{\hbar^2 \mathbf{k}_{\parallel}^2}{2m^*} \right) \varphi_n(z), \quad (2.41)$$

where ϵ_{n0} is the band edge energy at the Γ point. Finally, for a potential $V(r)$ which varies slowly comparing to the crystalline potential, the envelope wave function of an electron in a certain band is the solution of the Schrödinger equation of a particle having the effective mass corresponding to the band and undergoing the potential $U(\mathbf{r})$.

In the case of a triangular QW, assuming a constant effective mass and an infinite vertical barrier, this equation has analytical solutions which are expressed with the Airy function of the first kind. However, those two assumptions are not accurate. Therefore it is preferable to look for approximated numerical solutions. Several algorithms exist for that, such as transfer matrix method or finite difference methods. At each hetero-interface, the following boundary conditions should be considered to solve Eq. (2.41):

$$\begin{aligned} \varphi(z_i^-) &= \varphi(z_i^+) \\ \frac{1}{m^*(z_i^-)} \frac{d\varphi}{dz}(z_i^-) &= \frac{1}{m^*(z_i^+)} \frac{d\varphi}{dz}(z_i^+), \end{aligned} \quad (2.42)$$

where z_i is the position of the interface. Another important feature to solve this equation are the boundary conditions at the extremities of the structure. For MQW structure, periodic boundary conditions are used $\varphi(0) = \varphi(T)$ where T is the period. For single QW structures, the Neumann boundary conditions (the derivative is zero at the boundaries) are the most commonly utilized.

2.4.4 Many body effects: the Hartree method

In the previous sections, the calculations do not take into the electron-electron interactions arising from other electrons that populate the conduction band. However, for a doped structure, this assumption is not realistic. Furthermore, in polar MQWs, the space charge distribution will reorganize to screen the internal electric field. The most simple way to treat those interactions is a mean field approximation. It consists of calculating the mean coulombic potential of those electrons, and adding it to the potential, which can then be written $U(z) = U_H(z) + U_{SP}(z)$, where $U_H(z)$ is the heterostructure potential and $U_{SP}(z)$ the calculated Poisson potential (SP stands for Schrödinger-Poisson). This potential is the solution of the Poisson equation:

$$\frac{d}{dz} \varepsilon_r(z) \frac{d}{dz} U_{SP}(z) = -\frac{\rho(z)}{\varepsilon_0}, \quad (2.43)$$

where $\varepsilon(z)$ is the relative dielectric constant, and $\rho(z)$ the charge density. For QWs, the electron distribution depends on the shape of the wave functions. For each subband with an envelope function $\varphi(z)$, the density of the subband is noted N_i . Therefore, the charge density becomes:

$$\rho(z) = -q \left(\sum_i N_i \langle \varphi_i | \varphi_i \rangle \right) + q N_D^+(z), \quad (2.44)$$

where the second term corresponds to the fixed ionized donors. For reasons of global neutrality, the following relation should be fulfilled:

$$\sum_i N_i = \int N_D^+(z) dz. \quad (2.45)$$

The electronic density in the i^{th} subband is:

$$N_i = \int D_i(E) f(E) dE, \quad (2.46)$$

where $f(E)$ is the Fermi filling factor $D_i(E)$ is the 2D density of state, given by $D_i(E) = \frac{m^*}{\pi \hbar^2} H(E - E_i)$, with H the Heavyside function. It results:

$$N_i = \frac{m^*}{\pi \hbar^2} \int_{E_i}^{\infty} \frac{dE}{1 + \exp((E - E_F)/(k_B T))} = \frac{m^*}{\pi \hbar^2} \left[k_B T \ln \left(1 + \exp \left(-\frac{E_i - E_F}{k_B T} \right) \right) \right]. \quad (2.47)$$

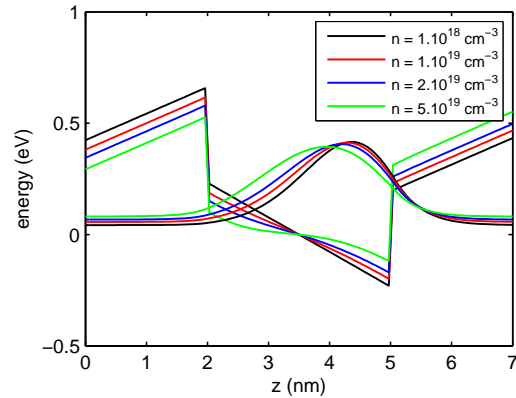
Finally, the Schrödinger equation requires the knowledge of U_{SP} , which needs the subband energies and wave functions. Those two equations have to be solved self-consistently:

$$\begin{cases} \left[-\nabla \frac{\hbar^2}{2m^*(z)} \nabla + U_H(z) + U_{SP} \right] \varphi_i(z) = E_i \varphi_i(z) \\ \frac{d}{dz} \varepsilon_r(z) \frac{d}{dz} U_{SP}(z) = \frac{1}{\varepsilon_0} q \left(\sum_i N_i \langle \varphi_i | \varphi_i \rangle - N_D^+(z) \right) \end{cases} . \quad (2.48)$$

2.5. Intersubband transitions in 2D confined systems

This system is called Schrödinger-Poisson, and is usually solved iteratively until the desired convergence. Most of band structure calculations presented in this manuscripts have been done using Nextnano software [39]. It solves self-consistently the Schrödinger-Poisson problem using a 8 bands $\mathbf{k} \cdot \mathbf{p}$ model. The numerical method for solving differential equations is the finite difference method.

Figure 2.15 – Effect of charge screening in a 3 nm GaN QW with $\text{Al}_{0.3}\text{Ga}_{0.7}\text{N}$ barrier calculated at different doping concentrations with Schrödinger-Poisson method.

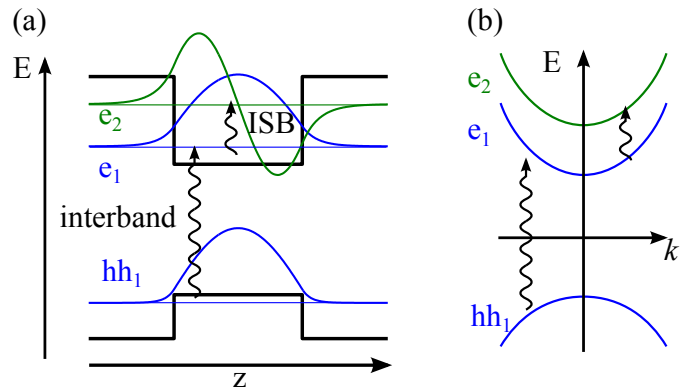


An example of Schrödinger Poisson calculation is given in Fig. 2.15 which evidences the electric field screening by free charges in the QWs.

2.5 Intersubband transitions in 2D confined systems

This section explains the physics of ISB transitions, emphasizing the major differences with interband transitions and the specificities of ISB transitions on III-nitride based heterostructures.

Figure 2.16 – illustration of inter-band and ISB optical transition in the real space (a) and in the reciprocal space (b).



2.5.1 ISB optical transition and oscillator strength

Once the band profile, the energies and the envelope functions of the MQW structure have been computed, one can now consider the interaction with an electromagnetic field with a

Chapter 2. Basics on III-nitride semiconductors and intersubband transitions

pulsation of ω . The magnetic and electric fields (\mathbf{B} and \mathbf{E}) of the electromagnetic wave are characterized by the vector potential \mathbf{A} and the scalar vector U via the following relations:

$$\begin{aligned}\mathbf{B}(\mathbf{r}, t) &= \nabla \times \mathbf{A}(\mathbf{r}, t) \\ \mathbf{E}(\mathbf{r}, t) &= -\frac{\partial \mathbf{A}(\mathbf{r}, t)}{\partial t} - \nabla U(\mathbf{r}, t).\end{aligned}\quad (2.49)$$

It can be shown that the hamiltonian under those potentials can be written as:

$$\hat{H}(\mathbf{r}, t) = \frac{(\hat{\mathbf{p}} - q\mathbf{A}(\mathbf{r}, t))^2}{2m} + V(r) + qU(\mathbf{r}, t) \quad (2.50)$$

In the case of a monochromatic plane wave, the Coulomb gauge is well-adapted, since it induces a simple form of the hamiltonian. The Coulomb gauge is characterized by:

$$\nabla \cdot \mathbf{A}(\mathbf{r}, t) = 0. \quad (2.51)$$

This relation induces that the scalar potential $U(\mathbf{r}, t)$ is equal to zero (for a plane wave in a dielectric medium).

If the electric field is:

$$\mathbf{E} = \mathbf{E}_0 \cos(\mathbf{k} \cdot \mathbf{r} - \omega t) = E_0 \boldsymbol{\epsilon} \cos(\mathbf{k} \cdot \mathbf{r} - \omega t),$$

where $\boldsymbol{\epsilon}$ corresponds to the unitary polarization vector, the vector potential then becomes:

$$\mathbf{A} = \frac{\mathbf{E}_0}{\omega} \sin(\mathbf{k} \cdot \mathbf{r} - \omega t).$$

Hence the Eq. (2.50) can be developed in the Coulomb gauge. If the second order terms are neglected, the hamiltonian is:

$$\hat{H} = \hat{H}_0 + \hat{W}(t) \quad \text{with} \quad \hat{W}(t) = -\frac{q}{m} \mathbf{A}(\mathbf{r}, t) \cdot \hat{\mathbf{p}} \quad (2.52)$$

\hat{W} is called the $A \cdot p$ hamiltonian, and \hat{H}_0 is the electron hamiltonian studied before. The spacial dependency of the vector potential is neglected since the typical structure sizes are much smaller than the wavelength of the excitation wave. The interaction energies with the electromagnetic wave are small compared to the coulombic potential, thus $A \cdot p$ hamiltonian can be treated in the framework of perturbation theory. Therefore, the transition rate $\Gamma_{if} = dP_{if}(t)/dt$ (where $P_{if}(t)$ is the transition probability) from initial quantum state $|i\rangle$ of energy E_i to a final state $|f\rangle$ of energy E_f is given by the following Fermi golden rule [40]:

$$\Gamma_{fi} = \frac{\pi}{2\hbar} |W_{fi}|^2 \delta(E_f - E_i - \hbar\omega), \quad (2.53)$$

2.5. Intersubband transitions in 2D confined systems

where δ is the dirac distribution, and W_{fi} are given by the following formula:

$$W_{fi} = \langle f | \hat{W} | i \rangle = \frac{qE_0}{m_e\omega} \langle f | \mathbf{p} \cdot \boldsymbol{\epsilon} | i \rangle. \quad (2.54)$$

Using the commutation relations, it is straightforward to demonstrate that:

$$W_{fi} = -\frac{i(E_f - E_i)}{\hbar\omega} qE_0 \langle f | \mathbf{r} \cdot \boldsymbol{\epsilon} | i \rangle. \quad (2.55)$$

In the case of resonant excitation ($\hbar\omega = E_f - E_i$), the Goeppert-Mayer gauge ($\hat{W} = -\mathbf{D} \cdot \mathbf{E}$) would give the same result. To quantify the transition, it is useful to define the oscillator strength, which is a dimensionless quantity :

$$f_{osc} = \frac{2m}{\hbar^2} (E_f - E_i) |\langle f | \mathbf{r} \cdot \boldsymbol{\epsilon} | i \rangle|^2, \quad (2.56)$$

The absorption, spontaneous and stimulated emission rates between $|i\rangle$ and $|f\rangle$ levels are all proportional to f_{osc} .

2.5.2 ISB selection rules

Let's focus on the term $\langle f | \mathbf{r} \cdot \boldsymbol{\epsilon} | i \rangle$ from equation (2.56). In the envelope function formalism, the electron wave function is written:

$$\psi_{i/f}(\mathbf{r}) = \frac{1}{\sqrt{S}} \varphi_{i/f}(z) \exp(i\mathbf{k}_{\parallel}^{(i/f)} \cdot \mathbf{r}_{\parallel}) u_{n_{i/f}, \mathbf{k}=0}(\mathbf{r}), \quad (2.57)$$

where the \parallel sign in index means that only the components parallel to the QW (x and y) are used. n_i and n_f correspond to the bands of the initial and final states. For ISB transition the two values will be equal, whereas for interband transitions they will be different. Taking into account the fact that the envelope functions vary slowly at the scale of the unit cell, it results [40]:

$$\begin{aligned} \langle f | \mathbf{r} \cdot \boldsymbol{\epsilon} | i \rangle &\simeq \boldsymbol{\epsilon} \cdot \langle u_{n_f, \mathbf{0}} | \mathbf{r} | u_{n_i, \mathbf{0}} \rangle \langle \varphi_f(z) | \varphi_i(z) \rangle \delta_{\mathbf{k}_{\parallel}^i, \mathbf{k}_{\parallel}^f} \\ &+ \langle u_{n_f, \mathbf{0}} | u_{n_i, \mathbf{0}} \rangle \langle \varphi_f(z) | \mathbf{r} \cdot \boldsymbol{\epsilon} | \varphi_i(z) \rangle \delta_{\mathbf{k}_{\parallel}^i, \mathbf{k}_{\parallel}^f}, \end{aligned} \quad (2.58)$$

where δ is the Kronecker symbol, meaning that the parallel components of the wave vectors are conserved. Equation 2.58 is the sum of two distinct terms. The first term is non zero only if the states $|i\rangle$ and $|f\rangle$ are from different bands $u_{n_i, \mathbf{0}}$ and $u_{n_f, \mathbf{0}}$ having different parity. This corresponds to an interband transitions. It follows that for interband transition the dipole moment is proportional to the overlap integral $\langle \varphi_f(z) | \varphi_i(z) \rangle$ (see eq. 2.31).

The second term corresponds to the ISB transition. In this case we have $n_i = n_f$ which implies

that $\langle u_{n_f,0} | u_{n_i,0} \rangle = 1$, and results to a simple form of the matrix element:

$$\langle f | \mathbf{r} \cdot \boldsymbol{\epsilon} | i \rangle \simeq \langle \varphi_f(z) | \mathbf{r} \cdot \boldsymbol{\epsilon} | \varphi_i(z) \rangle = \boldsymbol{\epsilon} \cdot \hat{\mathbf{u}}_z \langle \varphi_f | z | \varphi_i \rangle \quad (2.59)$$

where $\hat{\mathbf{u}}_z$ is the unitary vector in the z direction. The oscillator strength for an ISB transition can be rewritten as :

$$f_{osc} \simeq \frac{2m}{\hbar^2} (E_f - E_i) |\langle \varphi_f | z | \varphi_i \rangle|^2 \boldsymbol{\epsilon} \cdot \hat{\mathbf{u}}_z \quad (2.60)$$

From this result, one can deduce the two important selection rules that govern ISB transitions:

- The factor $\boldsymbol{\epsilon} \cdot \hat{\mathbf{u}}_z$ indicates that only the z component of the electric field induces a transition. In other words, the wave should be *TM* polarized. This has incidence on the way to measure ISB absorption, since the wave propagation vector cannot be perpendicular to the sample surface, as it is generally the case for interband absorption measurements. One has to use specific geometries, such as the multipass waveguide configuration (Fig. 2.17) or a grating on the sample surface to couple the light and observe an ISB transition. This selection rule is also a major criterion to prove that observed optical absorption or emission comes from ISB transition.
- The second selection rules originates from the term $|\langle \varphi_f | z | \varphi_i \rangle|^2$. This term is non zero only if the two functions have a different parity. For instance, in a square QW, the $e_1 - e_2$ transition is possible whereas the $e_1 - e_3$ transition is forbidden. It is the opposite for interband transitions where the two envelope functions should have the same parity.

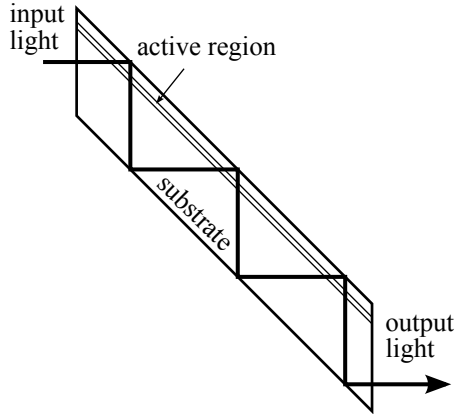


Figure 2.17 – Multipass waveguide configuration with facets polished at 45° for ISB absorption measurements.

Another specificity of ISB transition is the quasi-resonant absorption spectrum. This comes from the Dirac function in the transition rate $\delta(E_f - E_i - \hbar\omega)$. Indeed the energies in the QW can be written as :

$$E_{i/f} = \epsilon_0 + e_{i/f} + \frac{\hbar^2 \mathbf{k}_{\parallel, i/f}^2}{2m^*}$$

where ϵ_0 is the energy of the band at $\mathbf{k} = 0$, and $e_{i/f}$ are the energies of the subbands. Since

the wave vector \mathbf{k}_{\parallel} is conserved, it results that the energy difference $E_f - E_i$ does not depend on the wave vector. It is another major difference with interband transition where the energy difference increases with the wave vector. The subband energy difference is depicted in figure 2.16(b). Finally, even if the confinement is only in one direction, meaning that the subbands have a continuous energy spectra, the transition behaves as if the two levels were discrete.

2.5.3 Specificities of ISB transitions in GaN

The specificity of polar GaN-based heterostructure is the internal electric field. The effects of this field on interband transitions have been described in section 2.4.1. Regarding ISB transitions, the electric field has also important impacts, as illustrated in Fig. 2.18. The calculations have been performed in GaN/AlN MQWs assuming a CBO of 1.8 eV and an effective mass of $0.2 m_0$.

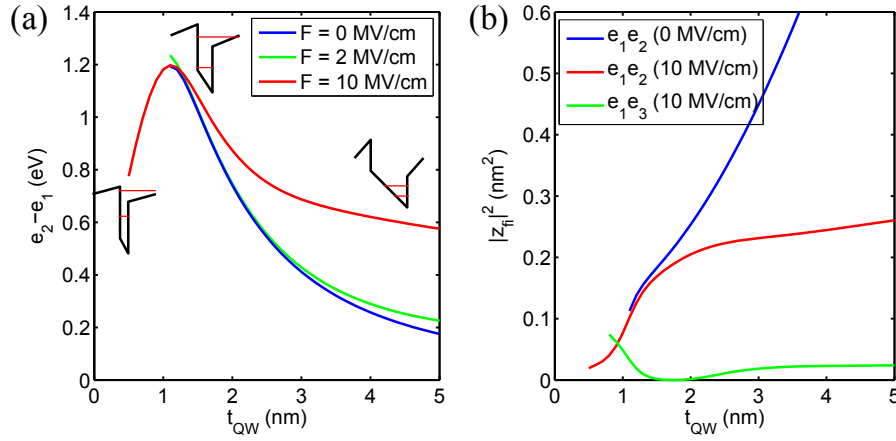


Figure 2.18 – **Effect of internal electric field on ISB transitions in AlN/GaN MQW structure:** calculations are done assuming periodic boundary conditions on a MQW structure, with a varying QW thickness (t_{QW}) and a fixed barrier width of 4 nm. (a) Transition energy between the two first levels for different values of electric field. (b) $|\langle \varphi_f | z | \varphi_i \rangle|^2$ matrix elements of the ISB transitions.

First, on Fig. 2.18(a) one can see that for large enough QWs the ISB transition energy is higher in the presence of an electric field than for flatband conditions ($F = 0$ MV/cm). This is due to the higher confinement energy in the triangular potential. Besides, for very thin QW (with large enough barriers), the second level is not confined in well, but partially in the barriers, due to the sawtooth profile of the MQW structure. Therefore the ISB energy increases at first when the QW thickness increases. For thicker QWs, both levels are confined in the triangular potential, resulting in a decreasing followed by a constant ISB energy. Indeed, for large QWs, the levels are not confined by the QW thickness, but by the triangular potential. To reach long wavelengths, one has to overcome the effects of the internal field. For instance one can use AlGaN barriers to reduce the polarization discontinuity, or adjust the doping level to induce

a screening of the field. However, this is not sufficient for THz wavelengths. ISB absorption in THz has been observed, using GaN/Al_{0.05}Ga_{0.95}N stepped QWs in Al_{0.1}Ga_{0.9}N barriers, to compensate the electric field in the QW [4]. Coupled QWs can also be a solution to observe transition in THz regime [41].

Secondly, since the electric field breaks the symmetry in the QW, ISB transitions between levels having the same parity become possible. The green curve in Fig. 2.18(b) gives the $|z_{fi}|^2$ matrix element for the $e_1 - e_3$ transition, which is forbidden in a square QW. However, the oscillator strength remains lower for this transition than for the $e_1 - e_2$ transition.

2.6 State of the art of ISB optoelectronic devices

2.6.1 Brief history of ISB transitions and devices

The first ISB absorption measurements have been performed by West and Eglash in 1985 [42] on AlGaAs/GaAs MQW structures. They measured an absorption of few percents at room temperature with illumination under oblique incidence. Two years later, Levine *et al.* from the Bell laboratories demonstrated a dramatic improvement of the absorption at room temperature (up to 95 %) using the multipass waveguide configuration (Fig. 2.17).

The first ISB optoelectronic device is the QW infrared photodetector (QWIP) demonstrated in 1987 by Levine and coworkers at Bell Laboratories [43]. The principle of QWIP is illustrated on figure 2.19(a). It consists of an n-doped MQW structure with bottom and top contacts. The structure is designed to have the first subband levels partially populated with electrons that cannot tunnel in the SL. When ISB absorption occurs, the electrons can hop to the continuum or to a higher subband that allows tunneling to the next QW. Repetition of this process induces a drift of the electron in a preferred direction, thanks to an external applied voltage, creating a photocurrent. This bias voltage is necessary to detect a photocurrent. Therefore, a dark current is always observed in the absence of absorption. Today, QWIPs are commercially available and are mainly used for thermal IR imaging. More recently, in 2002, ISB detectors using quantum cascade structures, named quantum cascade detectors (QCD) have been demonstrated [44, 45]. Unlike QWIPs, they are photovoltaic detectors, and thus do not require a bias voltage, which induces dark current. Besides a responsivity as high as 35 mA/W could be achieved [45]. However, they exhibit a lower detectivity due to noise arising from parasitic transition. QCDs are the subject of the next chapter, where the physics will be more detailed. ISB absorption modulators have also been demonstrated. For instance Harwit and Harris reported in 1987 that Stark effect changes the ISB energy [46]. Modulated absorption has also been obtained using electric field induced electron transfer in coupled QWs [47].

In 1988, M. Helm reported the first ISB electroluminescence in the far IR [49]. The higher subbands are populated by applying an electric field parallel to the QWs and the light is

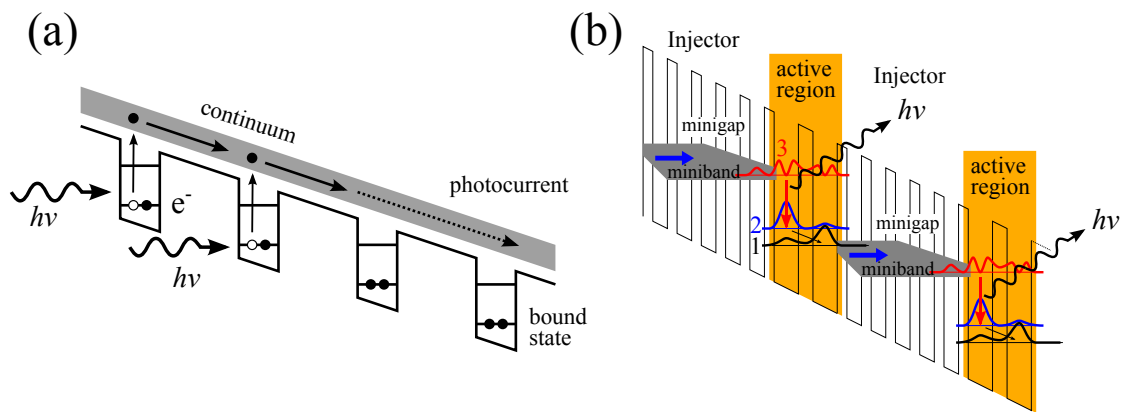


Figure 2.19 – (a) Schematic representation of a QWIP using bound to continuum mechanism. electrons from the bound state hop to the continuum after IR absorption, making the material conductor. (b) band diagram of a mid-IR QCL, using SL miniband transport for extraction and injection, and bound states in QWs for the active region. The optical transition occurs between levels $|3\rangle$ and $|2\rangle$. Figure adapted from Ref. [48]

extracted thanks to a grating. The first ISB laser, named quantum cascade laser (QCL), emitting at $\lambda = 4 \mu\text{m}$ was demonstrated at Bell laboratories in 1994 by Faist and coworkers [50]. This light amplification in SL subbands has been theoretically predicted in 1971 by Kazarinov and Suris [51]. The structure of a QCL is complex and consists of a periodical stacking of an injector region and an optically active region. The injector region is a MQW structure that allows miniband transport to fastly depopulate the ground level of the active region, and therefore achieve the population inversion. Sufficient gain is achieved thanks to the large number of periods. A QCL consists typically of several hundreds of periods. Fig. 2.19(b) gives a schematic representation of QCL principle. It is nowadays a well established technology and room temperature continuous wave lasers exist from $4 \mu\text{m}$ to over $20 \mu\text{m}$ wavelength, most of them based on low-strain InGaAs/AlInGaAs structures on InP. The realization of QCL in the THz regime (below the LO-phonon energy) was a complicated task, principally due to the difficulty to get fast enough transport without involvement of LO-phonon interactions. It is in 2002 that Kohler *et al.* demonstrated a QCL based on GaAs/AlGaAs and working at low temperature in the THz regime [52]. Recently, dramatic progress have been made in THz QCL and operating temperatures above 180 K have been reported [53, 54] using efficient injection and depopulation by LO-phonon assisted scattering instead of resonant tunneling SL structures. More details about QCLs will be found in Ref. [55]. Optically pumped ISB lasers, known as quantum fountain laser, have first been reported in 1997 in mid-IR [56]. More recently, strong coupling between cavity photons and ISB excitation have been published [57]. Those ISB polaritons present also good prospects for laser applications [58].

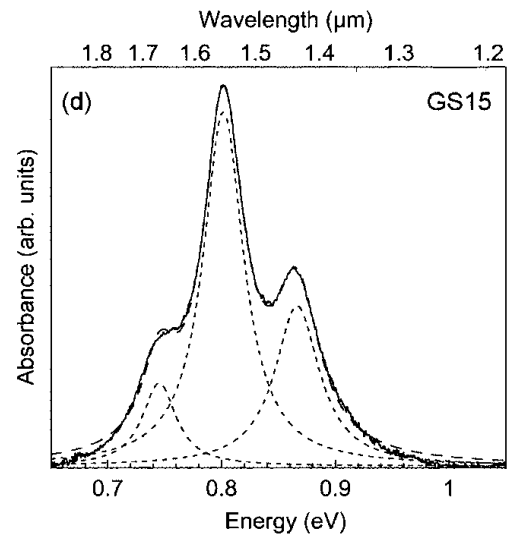
2.6.2 Review of GaN based ISB devices

From the mid 90s, a growing interest in ISB devices for optical-fiber telecommunication wavelengths arose. In 1994, Smet *et al.* report ISB absorption at 1.55 μm on InGaAs/AlAs QWs [59]. However, the important strain does not permit to grow good quality QCL structures. Besides AlAs barriers would induce parasitic intervalley leakage which is not suitable to achieve lasing. Short wavelength ISB transitions have also been reported on ZnSe/BeTe type II SL [60]. Today, the shortest wavelength reported for a QCL is 2.6 μm , operating up to 175 K, using InAs/AlSb lattice matched system, which feature a large CBO [61].

III-nitrides appear to be candidates of choice for short wavelength operating devices. Not only they benefit from large band offset, but their polar structure enable ultrafast relaxation *via* interactions with phonons. The first theoretical works on the subject have been performed by Suzuki and Iizuka [62, 63, 64]. They have predicted the feasibility of ISB GaN-based devices working at 1.55 μm . They have also calculated a relaxation time of 100 fs, much shorter than for InGaAs-based QWs. In 2000, the same authors reported ISB absorption in MOVPE grown $\text{Al}_{0.65}\text{Ga}_{0.35}\text{N}/\text{GaN}$ MQWs at a wavelength of $\sim 4.6 \mu\text{m}$ [65]. They measured a relaxation time of 150 fs, close to their previous predictions. Shortly after, Gmachl *et al.* at Bell Laboratories demonstrated absorption at different wavelengths from 1.55 to 4 μm , in PA-MBE grown Al-GaN/GaN MQWs with Al content up to 85 % in the barriers [66, 67]. Iizuka *et al.* also achieved ISB absorption in PA-MBE grown AlN/GaN MQWs structures at wavelengths as short as 1.3 μm , with low enough linewidth ($\Gamma \sim 80 \text{ meV}$) to resolve single ML thickness fluctuations in the QWs [68]. They measured a relaxation time of 400 fs. The shortest measured wavelength is achieved by Kishino and coworkers, with a value of 1.08 μm [69], very close to the maximal theoretical value. ISB absorption on coupled (Al,Ga)N/GaN QWs has also been observed [70, 71]. In 2005, our laboratory and collaborators demonstrated absorption in MOVPE grown lattice matched InAlN/GaN MQWs heterostructures at $\lambda = 3 \mu\text{m}$ [72]. ISB absorption on high quality GaN/AlN MQWs with low absorption broadening ($< 70 \text{ meV}$ at room temperature) could allow determination of CBO with excellent accuracy [1] (Fig. 2.20 shows the ISB absorption of a high quality sample). ISB emission in GaN/AlN MQW structure grown on AlN templates on sapphire by PA-MBE has been demonstrated for the first time by Nevou *et al.* at $\lambda \sim 2 \mu\text{m}$ [73, 74]. Similar results have been reported by other groups [75].

Following those improvements in ISB absorption in III-nitrides, the first GaN-based QWIP, operating below 2 μm wavelength up to 150 K, was demonstrated by Hofstetter *et al.* in 2003 [76]. This device exhibits a responsivity of 20 $\mu\text{A}/\text{W}$ at 10 K. Few years later, Vardi *et al.* demonstrated the first QCD based on GaN/AlGaIn/AlN MQWs detecting at 1.7 μm at room temperature [77]. This device has a responsivity of 20 mA/W . The same authors showed high speed operation on similar structure (cutoff frequency of $\sim 11 \text{ GHz}$) [3]. Detectors in near IR relying on intrasubband transition in quantum dots have also been reported [78, 79]. In 2014,

Figure 2.20 – ISB absorption measurement from a GaN/AlN (1.5/2.8 nm) PA-MBE grown MQW structure emitting at 1.55 μm . The sample quality is attested by the resolved ML fluctuations. Reproduced from Ref. [1].



QCDs grown by MOVPE and operating at $\lambda \sim 4 \mu\text{m}$ have been achieved [80].

Another kind of GaN-based ISB devices are the absorption modulators. They are of different kinds. The first type are the fully-optical modulators working with absorption saturation. The principle is the following: ISB absorbing QWs are pumped by an IR light, and the absorption of the probe at shorter wavelength is measured. At high pump power, electrons are mostly in the excited state, quenching the absorption of the probe. The first demonstration has been reported by Iizuka *et al.* with sub-picosecond switching times [81, 82, 83]. The second type is the depletion modulator, demonstrated by Baumann *et al.* [84], which consists of controlling the 1st level population by adjusting the bandstructure *via* an external voltage. When the QWs are depleted, the ISB absorption is reduced. The last kind of modulator is the electro-optical switch, involving charge transfer between two coupled QWs by applying an external voltage. This device has been fabricated by Nevou *et al.* in 2007 [2]; they also measured a cut-off frequency around 3 GHz [85].

However, one should notice that near infrared optoelectronic devices for fiber communications (such as lasers, detectors or modulators) are already very well established by interband devices made of InGaAsP on InP, and exhibit high performance. Even if III-nitride semiconductors can provide very fast ISB relaxation dynamics, the chances that they could compete with this well established technology are low. Therefore, more important effort has been made in the last 6-7 years to develop GaN based source in THz range. Thanks to the high LO-phonon energies of III-nitride (92 meV for GaN) they theoretically enable sources emitting in the Reststrahlen band of GaAs and InP, corresponding to a non transparency window due to LO-phonon absorption ($\hbar\omega_{\text{LO}} = 36 \text{ meV}$ for GaAs and 38 meV for InP). Some theoretical works have been done to demonstrate the feasibility of GaN-based QCL operating at room temperature, or to propose optimized designs [86, 87, 88]. THz absorption at cryogenic tem-

Chapter 2. Basics on III-nitride semiconductors and intersubband transitions

perature have been observed at 2.1 THz ($\sim 143 \mu\text{m}$) and 4.2 THz ($\sim 70 \mu\text{m}$) using stepped QWs [4]. Following this work, Sudjarat *et al.* demonstrated a QWIP working at $\lambda \sim 23 \mu\text{m}$ on the same kind of stepped QWs [89]. The device exhibits a responsivity of $\sim 7 \text{ mA/W}$ and works up to 50 K. Growth and characterization of QCL structures have also been attempted in the group of Hirayama in Japan [90]. These authors have observed a TM-polarized electroluminescence on those quantum cascade structures at low temperature centered at 1.37 THz ($\sim 225 \mu\text{m}$) [41]. All those preliminary results are promising. However, all those devices operate at low temperatures.

3 Intersubband photodetectors

This chapter aims to present the results obtained on QCDs. The first section provides generalities on IR ISB detectors, explaining the physics, transport models, and the figures of merit. The second part introduces the specificities of a GaN-based QCD. The last two sections present the results obtained on two different designs of QCDs. The first approach is a two-colors QCD that uses the $|1\rangle - |3\rangle$ transition (normally forbidden in a square QW) to detect at $\lambda \sim 1 \mu\text{m}$, which is the shortest wavelength ever reported for an ISB device. The second solution proposes a novel design on AlGaIn alloy extractor. This simpler active region is more robust from a growth point of view.

3.1 Physics of IR photodetectors

There are two main categories of photodetectors. In a photoconductive detectors, the absorbed light changes the carrier state from a resistive to a conductive state, *i.e.* it modulates the conductivity of the material. In this case, a voltage needs to be applied in order to detect light. This is the case for standard QWIPs. The other kind of detectors are photovoltaic, which means that in addition to the conductivity modulation, the asymmetry of the structure favors one direction for the current, *i.e.* a voltage is detected under illumination on an open-circuit operation. This asymmetry can be achieved for instance using a p-n (or p-i-n) junction, a Schottky barrier, a modulation doping, or an asymmetric MQW structure, as it is the case for QCDs.

3.1.1 ISB photodetectors: principles and figures of merit

In the next two paragraphs, one details the principal figures of merit of ISB photodetectors: the responsivity and the detectivity. In addition, the frequency response is also discussed, as it is a crucial parameter for high speed operation.

Responsivity of a detector:

The responsivity quantifies the efficiency of the detector. It is generally expressed in A/W, *i.e.* it corresponds to the ratio between the photocurrent and the light intensity on the surface of the detector. Let's consider a luminous flux impinging the detector with a power P (corresponding to a number of photons per unit time $N_\phi = P/h\nu$). The responsivity of a detector is then:

$$\mathcal{R} = \frac{q}{h\nu} \eta g \simeq \frac{\lambda [\mu\text{m}]}{1.24} \eta g, \quad (3.1)$$

where η is the quantum efficiency and g the optical gain. The quantum efficiency corresponds to the number of photons arriving at the detector surface divided by the number of photo-emitted electrons, which ideally corresponds to the number of absorbed photons if one neglects parasitic absorption processes. η is the product of the external and internal quantum efficiencies :

$$\eta = \eta_{int} \eta_{ext}$$

where η_{ext} is related to the reflectivity ($\eta_{ext} = 1 - R$), with R the reflectivity coefficient which is easily calculated for a flat surface of a semiconductor having an optical index n : $R = (n - 1)^2 / (n + 1)^2$. The reflectivity varies depending on the incident angle. For ISB processes, light is generally injected at the Brewster angle (around 60° for GaN), where the reflection of the p -polarized light (that can satisfy the ISB selection rules) is zero. The reflectivity can also be tuned using gratings, photonic structures, or simply roughening of the surface. The internal quantum efficiency η_{int} is related to the absorption in the structure. Concerning the optical gain (g factor in Eq. 3.1), it corresponds to the number of collected electrons in the external circuit, divided by the number of photo-emitted electrons. In general, this parameter is not necessarily limited to one: for instance an avalanche photodiodes can have a gain higher than 1000. In a general way, this gain can be expressed as the carrier lifetime (in the the conductive state) divided by the transit time, *i.e.* the time to go from one contact to the other:

$$g = \frac{\tau}{\tau_{tr}}. \quad (3.2)$$

For an ISB photodetector like a QWIP or a QCD, the gain is given by the following formula:

$$g = \frac{p_e}{N p_c} \quad (3.3)$$

where N is the number of periods in the structure, p_e and p_c are the escape and capture probabilities:

$$p_e = \frac{\tau_{relax}}{\tau_{relax} + \tau_{esc}} \quad \text{and} \quad p_c = \frac{\tau_{trans}}{\tau_{trans} + \tau_c}, \quad (3.4)$$

where the different τ corresponds to the lifetime of the different processes: τ_{relax} stands for

the relaxation time between the excited state to the ground state of the active QW, τ_{esc} stands for the escape time from the QW, τ_{trans} is the transit time from one active QW to the next one (in the next period), and τ_c is the capture time to the ground state of the next QW.

Noise and detectivity:

Any photodetector generates some noise, which is superimposed with the photo-generated signal. To detect a signal, the detector should allow to extract the detection signal from the noise, which means that the signal-noise ratio must be maximized. If one note i_S the photocurrent and i_N the noise-originated current, the ratio to maximize is :

$$\frac{S}{N} = \frac{i_S}{i_N}$$

Knowing that the signal is related to the light power *via* the responsivity, one can define the noise equivalent power (NEP) that corresponds to the impinging light power inducing a signal-noise ratio equal to one:

$$NEP = \frac{i_N}{\mathcal{R}}, \quad (3.5)$$

which corresponds to the minimal power that can be detected. It is clear that this value is not intrinsic and will depend on the area of the detector A and its spectral bandwidth $\Delta\nu$, which is related to the acquisition time: $\Delta\nu = 2/T_{acq}$. The detectivity D^* is then defined as:

$$D^* = \frac{\sqrt{A\Delta\nu}}{NEP} = \frac{\mathcal{R}\sqrt{A\Delta\nu}}{i_N}, \quad (3.6)$$

and depends only on the material. It is a crucial figure of merit of any photodetector. The unit used for D^* is $\text{cm Hz}^{1/2} \text{W}^{-1}$, usually referred as *Jones*. There are three main origins for the noise in a photodetector.

- **thermal noise** (or Johnson noise) [91] comes from the thermal fluctuations of the carriers velocity. This thermal noise is present even in the absence of any signal. The average value of the so-generated current is zero, however $\overline{i_{th}^2}$ is non zero and depends on the temperature according to the following relation:

$$\overline{i_{th}^2} = \frac{4k_B T \Delta\nu}{R}, \quad (3.7)$$

where R is the resistance of the sample.

- **Shot-noise** (or generation-recombination noise) has for origin the quantized nature of the carriers. It comes from random processes, which follow a Poisson statistics. In other words, shot noise is associated with any detected signal. If the expected value of the collected electrons is \overline{N} , corresponding to an average current $I = q\overline{N}/T$, then the

properties of Poisson distribution imply that the variance of σ_N^2 is equal to \bar{N} . Therefore, the noise associated to the current I becomes:

$$\overline{i^2} = \left(\frac{q}{T}\right)^2 \sigma_N^2 = 2qI\Delta\nu.$$

If both generation and recombination processes are involved, the two contributions will be added, and the formula is more complex:

$$\overline{i_{gr}^2} = 4qgI\Delta\nu, \quad (3.8)$$

where g is the gain introduced in Eq. 3.1. In addition to the shot noise associated with the photo-induced signal, dark and leakage currents also generate shot noise.

- **Background noise** corresponds to the shot-noise of the current from the detected background photons. Those parasitic photons come from the black-body radiations in the surroundings of the detectors. The related current density is given by [40]:

$$J_{bg} = qg \int_{\lambda_1}^{\lambda_2} \eta(\lambda) \frac{d\Phi_{bg}(\lambda)}{d\lambda} d\lambda, \quad (3.9)$$

where $d\Phi_{bg}(\lambda)/d\lambda$ is the spectral photon flux due to black-body radiation (in $\text{cm}^2\text{s}^{-1}\mu\text{m}^{-1}$).

It should be noticed that thermal and generation-recombination noises are intrinsic, whereas the background noise comes from the surroundings. The thermal noise and the generation-recombination noise increase with the temperature (since the dark or leakage current are mainly coming from thermally activated carriers), whereas the background noise is constant. From this point, one can define a critical temperature under which the noise is background dominated, meaning that the performance of the detector cannot be enhanced. This temperature is noted T_{BLIP} , where *BLIP* stands for background limited infrared performance. It is also a good figure of merit, since it corresponds to the optimum working temperature. In this work, QCDs are characterized at room temperature above T_{BLIP} .

Frequency response:

Another important characteristic, particularly for applications in the telecommunications, is the cut-off frequency. It characterizes the shortest delay between two pulses that can be detected. This cut-off frequency is generally dominated by capacitive effects:

$$f_c = \frac{1}{RC},$$

where R is the resistance coming from the layer and contacts, and C the capacitance due to the space charge in the layer. So the optimum cut-off frequency is for minimal values of R and

C. State of the art QWIPs or QCDs have cut-off frequencies of several tens of GHz. This value is mostly dominated by extrinsic parameters (geometry of the device, and the RC constant), rather than the intrinsic carriers dynamics of the material.

3.1.2 Photoconductive QWIPs

The QWIP was first demonstrated by Levine *et al.* [43]. A schematic representation of the mechanism is given in Fig. 2.19(a). Electrons are populating the first subband of the QW and the IR absorption induces a transition to a conductive state. This transition can be either bound to bound (with an upper state that enables tunneling) or bound to continuum. More details about the physics of QWIPs can be found in the textbook from Schneider and Liu [92].

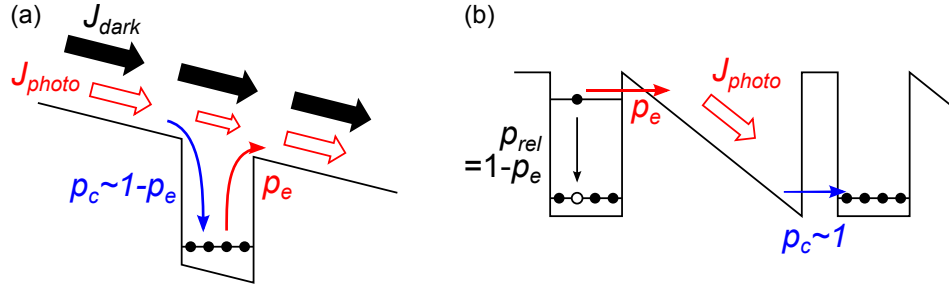


Figure 3.1 – (a) Mechanism of a photoconductive QWIP, with representation of emission and capture probabilities. (b) Mechanism of a photovoltaic QWIP or a QCD.

Figure 3.1(a) explains the mechanism of a QWIP: IR absorption excites an electron from the bound state to the continuum with a certain emission probability p_e , creating the photo-induced current (noted J_{photo}). A carrier from the continuum can also be trapped, with the capture probability of p_c . Those two mechanisms (escape and capture) are not independent; their respective probabilities are related *via* the following relation: $p_c \simeq 1 - p_e$. From equations (3.1) and (3.3), one can calculate the response of a QWIP:

$$\mathcal{R} = \frac{q}{h\nu} \eta_{MQW} \frac{p_e}{N p_c} = \frac{q}{h\nu} \eta_{1QW} \frac{p_e}{p_c}, \quad (3.10)$$

where N is the number of periods. To get the second relation, we used the fact that the absorption is proportional to the number of QWs. It results finally that the responsivity is independent from the number of periods.

Concerning the detectivity of QWIPs, it is generally limited by the noise arising from the dark current (for operating temperature higher than T_{BLIP}). The generation-recombination noise for a QWIP is given by [93]:

$$\overline{i_{gr}^2} = 4qI_{dark}(1 - p_c/2) \frac{1}{N p_c} \Delta\nu, \quad (3.11)$$

where I_{dark} corresponds to the dark current: $I_{dark} = Aq\rho_{3d,th}v$, with A the surface of the detector, $\rho_{3d,th}$ the density of thermally activated carriers in the barriers, and v the carriers velocity, which is the product of the mobility and the electric field ($v = \mu E$). If L is the barrier thickness between each QW, then $\rho_{3d,th} = \rho_{2d,th}/L$, which results in [40]:

$$\rho_{3d,th} = \frac{mk_B T}{l\pi\hbar^2} \exp(-E_a/(k_B T)).$$

Finally, the detectivity becomes:

$$D^* = \frac{\eta_{1QW} p_e}{hv} \sqrt{\frac{N}{p_c(1-p_c/2)\mu E \frac{mk_B T}{\pi\hbar^2 L} \exp(-E_a/(k_B T))}}. \quad (3.12)$$

So for a QWIP, the detectivity increases with the number of periods, and decreases with the temperature and the applied bias.

3.1.3 Photovoltaic QWIPs

From the previous paragraph, a clear drawback of standard QWIP is the dark current and its related noise. Therefore, shortly after the demonstration of QWIP by Levine *et al.* [43], the design was worked out to enable operation without bias voltage. Kastalsky *et al.* [94] demonstrated the first QWIP operating in photovoltaic mode. It relies on a miniband transport in a MQW structure and a collector made of a graded AlGaAs alloy, which creates an electric field.

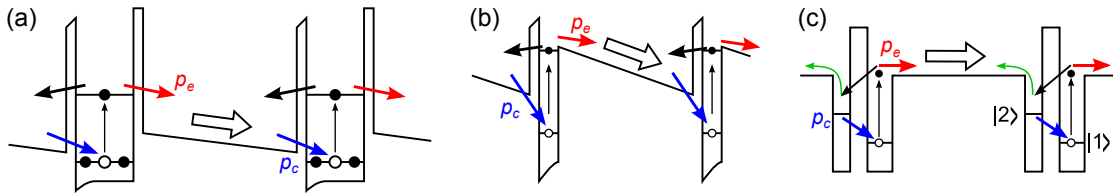


Figure 3.2 – Three different QWIP designs working in photovoltaic mode. (a) and (b) (respectively from Refs. [95] and [96]) use modulation doped large barriers. (c) uses tunneling between two adjacent QWs [97].

Figure 3.2 presents three different designs for photovoltaic QWIPs. For all three diagrams, the blue arrows represent the capture of an electron in the active QW, the red arrows, the emission mechanism giving a photocurrent (represented by the empty large arrow), whereas the black and green arrows represent the parasitic processes. The first design was proposed by Schneider *et al.* [95]. Each period consists on a double barrier GaAs/AlAs QW, and an AlGaAs large extractor. The electric field is achieved by modulation doping of the AlGaAs layer. The second design proposed few years later by the same group [96] is similar, except for

the asymmetric barrier around the QW to favor the electron extraction in the right direction. Finally, the last design is known as the four-zone QWIP [97]. It features two coupled QWs. An electron photo-emitted from the large QW will drift to the narrow QW of the next period. Then tunnelling occurs between the bound state of the narrow QW ($|2\rangle$) to the bound state of the large active QW ($|1\rangle$). The asymmetry comes from the fact that the tunneling time is much shorter than the escape time from the narrow QW to the previous period (represented by the green arrow).

All those designs have the common property that the capture mechanism is independent of the emission, inducing $p_c \simeq 1$. It is also clear from the drawings that the probability that a photo-excited electron will relax to the same QW cannot be neglected, resulting in a lower emission rate ($p_e < 1$). This has a direct influence on the response (Eq 3.10), which will be lower than for the QWIP. However, the shot-noise associated to any signal will be also lower. Indeed taking $p_c = 1$ in Eq. (3.11) results in:

$$\overline{i_{gr}^2} = 2qI \frac{1}{N} \Delta\nu, \quad (3.13)$$

which corresponds to a noise reduction of a factor $\sqrt{2}$. Another advantage of the photovoltaic mode is the absence of dark current, which implies that the detectivity is limited by the Johnson noise:

$$D^* = \frac{q\eta_{1QW}}{h\nu} \frac{p_e}{p_c} \sqrt{\frac{AR}{4k_B T}}, \quad (3.14)$$

where R is the resistance of the layer and A the surface of the detector. As the resistance increases linearly with the number of periods, the detectivity also increases with the number of periods. This behaviour is similar for QCDs. Experimentally, this resistance is extracted from current-voltage measurements.

3.1.4 Quantum cascade detectors

QCDs are also photovoltaic devices. This implies that their responsivity is given by Eq. 3.10, and the detectivity is also limited by the thermal noise (see Eq. 3.14). The difference with the afore presented photovoltaic QWIPs stands in the extraction region, which is not anymore a thick layer, but a graded SL, in which each energy level of each QW is designed to create a built-in electric field. The extractor superlattices are similar to the injector used in QCLs. This device was first demonstrated by Hofstetter *et al.* who showed that a QCL structure can also be used as a photodetector [44]. This mechanism was later on improved by Gendron *et al.* [45]; they could get a responsivity of 35 mA/W at $\lambda \sim 10 \mu\text{m}$. Later, the same group proposed an improved QCD design with higher resistance, giving a detectivity of 4.5×10^{11} Jones at 50 K for an operating wavelength of $8 \mu\text{m}$ [98]. QCDs operating in the THz range have also been

Chapter 3. Intersubband photodetectors

demonstrated by Graf *et al.* in 2005 [99]. The band structure of a QCD is given in Fig. 3.3(a). QCDs, compared to photovoltaic QWIPs, allows for more degrees of freedom. For instance, quantum engineering can help enhancing the p_e factor, using minigap or miniband. It can also help to achieve faster devices using LO-phonon assisted sequential tunneling. Recent reviews concerning the progress of QCDs can be found in Refs. [100] and [101].

If in an ideal QCD the dark current is zero, those devices however suffer from leakage current arising from unwanted diagonal transitions. In Fig. 3.3(a), for instance, electron transfer can occur from subband $|1\rangle$ to $|4\rangle$, $|3\rangle$ or $|2\rangle$ *via* thermal activation. This effect have been theoretically studied [102] and measured by magnetotransport characterization [103]. Those leakages induce a decrease of the layer resistance, therefore an increase of the Johnson noise. When accounting all the parasitic channels from two subsequent cascades A and B , the leakage current can be written:

$$J = q \sum_{i \in A} \sum_{j \in B} [G_{ij}(V) - G_{ji}(V)], \quad (3.15)$$

where the G_{ij} are the transfer rates (expressed in $\text{m}^{-2}\text{s}^{-1}$) calculated using the electron-phonon interactions, which strongly depend on the temperature [102, 104]. Finally, the associated resistance over one cascade becomes:

$$R_0 A = \frac{k_B T}{q^2 \sum_{i \in A, j \in B} G_{ij}}. \quad (3.16)$$

Let's conclude this section by a brief summary of the advantages and drawbacks of QCDs, compared to photoconductive QWIPs. The main disadvantage is the lower gain in QCD due to capture probability close to 1, which gives a lower responsivity, typically by a factor of 10 with respect to QWIP. On the other hand, photovoltaic detectors do not suffer from dark current, which allows to dope more the active QW, and thus increase the absorption with limited deleterious effects on the noise. Besides, the lower gain also induces a lower noise incoming with a signal (so a lower background noise or signal noise). Thanks to this lower noise, QCDs exhibit comparable detectivity to QWIPs, even with a lower response. So QCDs can have a certain advantage for devices that need a large area or large integration time systems, where the circuit will be much less saturated because of parasitic signal, such as dark current.

3.2 GaN based QCDs

3.2.1 Motivations for a GaN based QCD

As mentioned earlier, GaN-based heterostructures can have large CBOs, which enable ISB devices working in the near infrared, and particularly in the telecom range. So far, the shortest wavelength achieved for ISB detectors on conventional III-V materials is $2.14 \mu\text{m}$ [105]. Another advantage is the very short ISB relaxation time, which can result in ultrafast detectors. Thus, by engineering the cascade structure, GaN detector could outperform existing interband InAs or HgCdTe based detectors in the near IR. Cut-off frequencies as high as 42 GHz could be measured on AlN/GaN QCDs at $\lambda = 1.55 \mu\text{m}$ [106]. III-nitride compounds also offer the promise of devices operating in the THz bandgap (*i.e.* in the Reststrahlen band of GaAs) [89]. The demonstration of GaN-based QCDs is also a proof of principles of quantum cascade structures, and of the vertical transport mechanisms, which are crucial building block for the realization of QCLs.

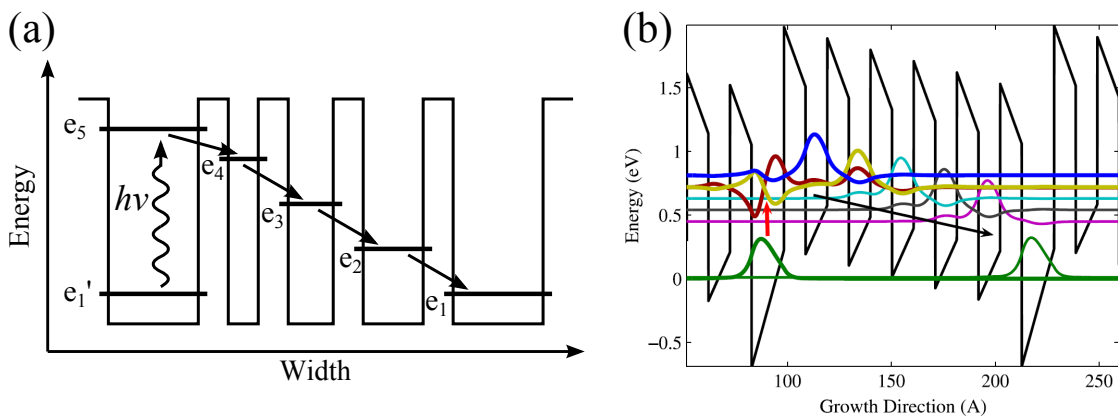


Figure 3.3 – Conduction band diagram of QCDs made of GaAs/AlGaAs (a) [45] and GaN/AlGaAs (b) MQW structures [77]. The second one achieves the staircase profile thanks to the internal electric field: the QWs of the extractor region have identical thicknesses.

3.2.2 Specificities of polar GaN-based QCDs

The most obvious difference between GaN/AlGaAs QCDs, when compared to other III-V materials, is the presence of the internal electric field. This is schematized on Fig. 3.3. For the GaAs-based QCD, the cascade structure is achieved using an increasing QW thickness in the extractor region. In contrast, for the GaN-based QCD, the staircase profile of the extractor is achieved thanks to the internal electric field, with a sequence of several identical barrier and QW thicknesses. The energy difference between two adjacent QWs of the extractor region is

then:

$$e_{i+1} = e_i - qF(t_w + t_b), \quad (3.17)$$

where e_i is the energy of the i^{th} QW, F the average electric field in the extractor region, t_w and t_b the thicknesses of the QW and the barrier, respectively.

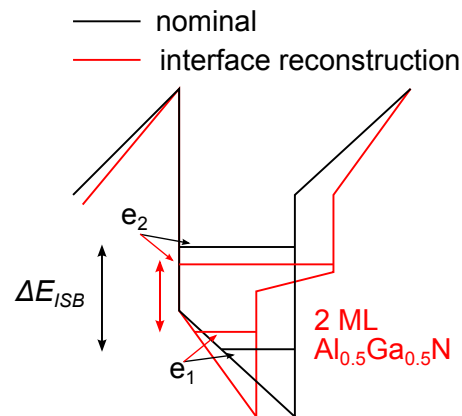
Another specificity of III-nitrides is the high electron effective mass, which induces, together with the large CBO, a strong confinement in the QWs of the extractor region. This influences the transport mechanisms in the structure. If coherent tunneling transport has been predicted and observed for GaAs-based QCDs [107], it is not likely the case for GaN-based QCD, where the involved mechanism is sequential tunneling *via* multiple scattering events. These scattering processes can have different origins, such as phonon interactions or interface roughness scattering. Coherent tunneling in GaN is a complex subject, which will be discussed in the next chapter dealing with RTDs. In addition, the disorder, which is higher in III-nitrides than in III-arsenides, is also detrimental for coherent transport. However, one should notice that in spite of all those difficulties, GaN-based QCDs, including those demonstrated in this work, well compete with other state of the art IR detectors, in terms of responsivity, detectivity or cut-off frequencies.

3.2.3 Growth of QCDs by NH₃-MBE

All QCDs presented in this manuscript have been grown by NH₃-MBE in a Riber compact 21 reactor. Optimized growth recipes have been developed previously in our lab for fiber optic wavelength QCDs using AlN/GaN SLs. This optimized recipe is detailed in the article of A. Dussaigne *et al.* [108] and in the thesis of S. Nicolay [109]. The most crucial requirements for short wavelength ISB devices are threefold. First, one should use high CBO materials system. The AlN/GaN system is therefore the most suitable one. Secondly, the QW has to be thin enough, typically between 1 and 1.5 nm (4-6 ML) [1]. This requires an excellent control of the growth rates, which have to be precisely calibrated prior to any growth. The third requirement concerns the sharpness of the GaN/AlN interface. Indeed interface disorder, even homogeneous, is highly critical to achieve ISB transitions in telecommunication range [110]. For instance, a simulation of a 2 ML graded AlGaIn interface instead of a sharp GaN/AlN interface, shows that the ISB energy is dramatically reduced, as illustrated in Fig. 3.4.

Ga surface segregation can occur in GaN/AlN MQWs, resulting in graded interfaces. As it is a thermally activated process, it is more pronounced for MOVPE or NH₃-MBE grown samples than for PA-MBE samples. This is the main reason why early MOVPE grown AlN/GaN SLs were exhibiting absorption at lower energy (at 2.4 μ m) [111, 112] than similar PAMBE grown structures [67]. In addition, the strain in the AlN barriers favors interface reconstructions, that hinders the formation of sharp interfaces. Theoretical investigation have indeed shown that

Figure 3.4 – Influence of interface reconstruction, modeled with a 2 ML $\text{Al}_{0.5}\text{Ga}_{0.5}\text{N}$ interlayer, in the ISB energy. The later is strongly reduced. Figure adapted from Ref. [108].



the GaN/AlN interface is not stable when strained to GaN [113, 114], and a graded interface is energetically more favourable. Nicolay *et al.* from our laboratory have demonstrated that telecom wavelength could be reached on MOVPE grown structures [110] by reducing the growth temperature from 1020° C to 935° C, and using unstrained AlN barriers. This last condition is achieved using an AlN (instead of usual GaN) template on sapphire substrate. They also demonstrated an improvement of the MQW quality using indium as surfactant [115]. More recent studies have demonstrated shorter wavelength from MOVPE grown samples using lower growth temperature and pulsed injection [116, 117].

Optimized NH_3 -MBE growth conditions:

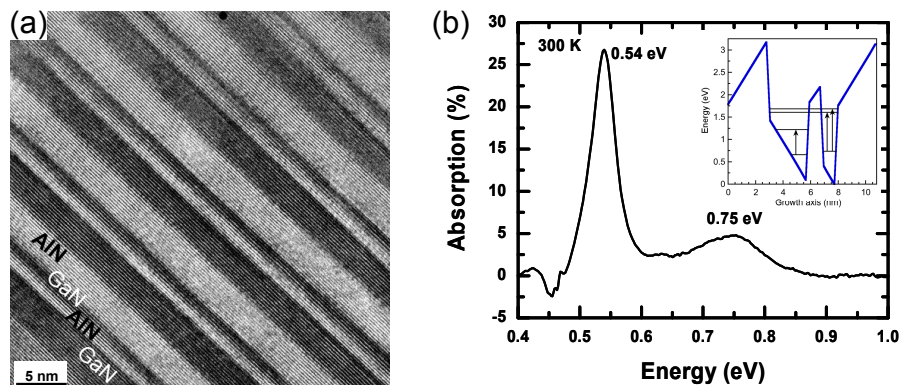


Figure 3.5 – (a) TEM image of an electro-optical modulator made of an AlN/GaN MQW structure grown by NH_3 -MBE. (b) PIA measurements of the same structure, the inset shows the band calculation. Figures reproduced from Ref. [108].

Concerning the GaN/AlN MQW structures, the optimized conditions for NH_3 -MBE growth are the following: the usual growth rate for GaN (resp. AlN) is ~ 1 ML/s (resp. ~ 0.1 ML/s). Those growth rates are calibrated using RHEED calibration and are also monitored *via* the reflectivity measurements for thick layers. Concerning the ideal temperatures, best qualities are achieved for GaN grown at 800° C and AlN at 900° C. The samples are also grown in nitrogen

rich conditions, and the ammonia flow is set constant at 80 sccm for the active region, whereas thick AlN layers are grown under a flux of 30 sccm, which is still a high V/III ratio, but sufficient due to higher NH₃ cracking efficiency at 900° C [118]. Typical temperature for the gallium (resp. aluminium) effusion cells is around 950-1000° C (resp. 950-1050 ° C). For PA-MBE samples, those parameters are quite different: typical growth rates are around ~0.3 ML/s and growth temperatures between 700° C and 750° C for GaN. Besides, the usual growth conditions are metal rich, using a wetting layer of 2 ML of gallium during the growth.

In our case, to minimize the interface instabilities and surface segregation of gallium in the AlN barrier, a growth interruption is done after the GaN QW. Then the substrate temperature is decreased from 800° C to 780° C. After a few tens of seconds, when the temperature is stabilized, the substrate temperature is increased progressively (usually up to 830° C or more depending on the barrier thickness) while the Al cell is opened for the barrier growth. For the subsequent GaN QW, no growth interruption is performed between the AlN barrier and the GaN QW, and the temperature is decreased to 800° C. Those temperatures are calibrated prior to growth using the pyrometer, giving a corresponding value for the substrate heater power. During the growth, the heater is only controlled by the input power.

The growth recipes have been adapted and developed for mid IR QCDs, which require AlGaN barrier instead of AlN. Depending on the Al concentration, the AlGaN barriers are grown at lower temperature and higher growth rate than AlN. The growth interruption between the QW and the barrier to prevent interface instabilities are still done, even if interface instability is less critical for longer wavelengths and AlGaN alloy barriers. More details regarding the growth is given for each specific sample presented here.

Substrate for short wavelengths operation devices:

As discussed earlier, and pointed out by Nicolay *et al.* [110], it is a great advantage to grow the GaN/AlN MQW structure on AlN, to minimize the strain in the AlN barriers and increase the interface stability. The same effect is observed on NH₃-MBE samples [108]. Figure 3.6, illustrates the improvement obtained using AlN templates.

Fig. 3.6(a) compares the ISB energy for similar structures grown using PA-MBE [1] on AlN template and NH₃-MBE on both AlN and GaN templates. The AlN template enables absorption above 0.8 eV (telecom wavelength limit). Fig. 3.6(b) compares two samples grown with the same optimized conditions described in the previous paragraph, using the same recipe for the active region. The structure is made of 15 periods of 5 ML GaN QW and 12 ML AlN barrier. A clear blue-shift of the photo-induced absorption is observed thanks to the AlN buffer layer. Such a shift cannot just be explained by a change of the CBO, but mainly by interface reconstruction due to the strain in the barriers. Another significant advantage of AlN template, which is still beneficial for Mid IR applications, is that the GaN/(Al,Ga)N SL is

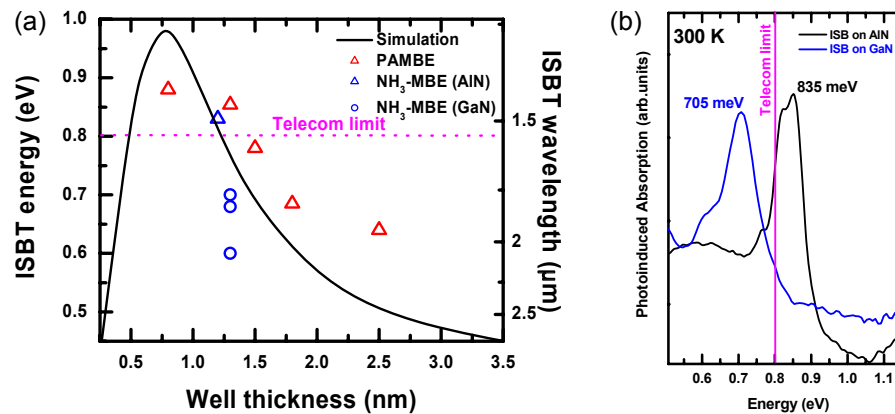


Figure 3.6 – **Substrate choice for AlN/GaN MQWs for NIR ISB applications.** (a) ISB measured energy depending on the GaN well thickness for PA-MBE grown structures [1] and NH₃-MBE grown structures on AlN and GaN templates on sapphire. (b) PIA measurement of the same structure grown by NH₃-MBE on GaN and AlN templates. Figure depicted from Ref. [108].

be under compressive strain ; this prevents the formation of cracks and increases the critical thickness. This advantage is even more valuable for QCDs structures, which have usually much thicker active regions (500 to 1000 nm) than the samples presented in Ref. [108].

For those reasons, all QCDs for near and mid-IR have been grown on commercial AlN templates on sapphire. They consist of a $1 \pm 0.3 \mu\text{m}$ AlN layer. They are of good quality, which is attested by the XRD rocking curves of the [0002] reflection exhibiting FWHM lower than 100 arcsec. The dislocation density is around 10^9 cm^{-2} . AFM pictures confirm the atomically smooth surface.

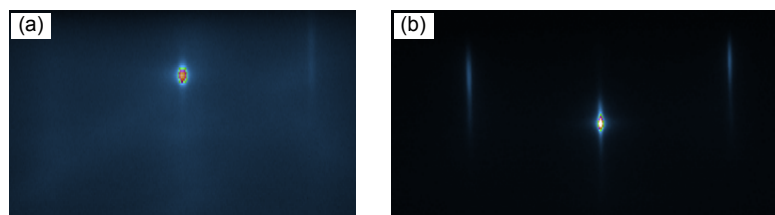


Figure 3.7 – RHEED pattern of an AlN template before (a) and after (b) HF cleaning.

However, those templates suffer from surface contamination, and get oxidized when stored for a long time, even in controlled atmosphere, which is detrimental for the quality of the subsequent epitaxial layer. Several processes have been tested to recover an epitaxy-ready clean surface. The best results were obtained by a two hours treatment in hydrofluoric acid (HF) at room temperature, followed by a water rinsing. Fig. 3.7 shows the RHEED pattern of the same AlN template before (left) and after (right) HF treatment. The more streaky and less diffuse pattern attests the improvement of the surface quality.

Influence of doping levels on ISB transitions:

Another crucial parameter for ISB is the doping level in the absorbing QWs. Indeed the first subband has to be populated at equilibrium in order to observe ISB absorption. Simulations using Nextnano were carried out to adjust the doping levels, in order to get a Fermi level approximately at the same energy of the first subband of the absorbing QW. Influence of doping on ISB transition on PA-MBE grown GaN/AlN MQWs has been studied by Helman *et al.* [119], where they observed a blue-shift when increasing the doping concentration due to electron-electron exchange interactions. A broadening of the ISB absorption have also been observed while increasing the doping level [120].

The doping level are even more crucial when dealing with ISB detectors. Indeed the Fermi level should be high enough to have the ground level populated and have sufficient absorption. On the other hand, too high doping levels first reduce the material quality, but more importantly reduce the layer resistivity, increasing the leakage currents and decreasing the detectivity. Furthermore, the ground level should not be saturated in order to increase the capture efficiency (p_c factor illustrated in Fig. 3.1 (b)). So a compromise should be found to get a high absorption (quantum efficiency) and a high layer resistance for maximum detectivity.

Practically, the dopant species is silicon, which is provided by a standard single filament effusion cell, whose crucible contains a crushed silicon wafer. The temperature of the cell typically ranges from 1050° C to 1300° C giving doping concentrations up to $\sim 2 - 3 \times 10^{19} \text{ cm}^{-3}$ under standard growth conditions. We could achieve very high Si-doping levels in our system, up to $2 \times 10^{20} \text{ cm}^{-3}$ by reducing the GaN growth rate to 0.1 ML/s and substrate temperature to 700° C to enhance Si incorporation [121]. The doping levels are regularly calibrated *via* Hall-effect measurements using the Van der Pauw geometry, or by capacitance-voltage measurements.

Fig. 3.8 shows the room temperature absorption measurement of four different grown QCDs. samples L373 and L429 consist of similar QCD structures designed to operate in the mid-IR at $\sim 2.6 \mu\text{m}$ (red curves). Each period consists of an optically active 3.1 nm GaN QW, followed by the extractor region made of three 1.5 nm GaN QWs separated by 1 nm AlN barriers. The complete structure consists of 40 periods. The two other samples (L374 and L440: blue curves) are very similar, except that the AlN barriers are replaced by $\text{Al}_{0.35}\text{Ga}_{0.65}\text{N}$ barriers. The simulations predict an ISB absorption at $\sim 3.6 \mu\text{m}$. The major different between the first series (L373 and L374) and the second series (L429 and L440) is the doping level in the active QWs. Due to a problem encountered with the Si effusion cell, the first series (Fig. 3.8(a)) was undoped. After opening the MBE reactor and changing the cell, the second series had QWs exhibiting $2 \times 10^{19} \text{ cm}^{-3}$ doping levels. For the first series, no ISB absorption could be detected, but only a photo-induced absorption. This method consists in exciting optically the electrons from the valence to the conduction band *via* a chopped UV-laser ($\lambda = 244 \text{ nm}$), then a second IR source is used to measure synchronously the ISB absorption [122]. The doped

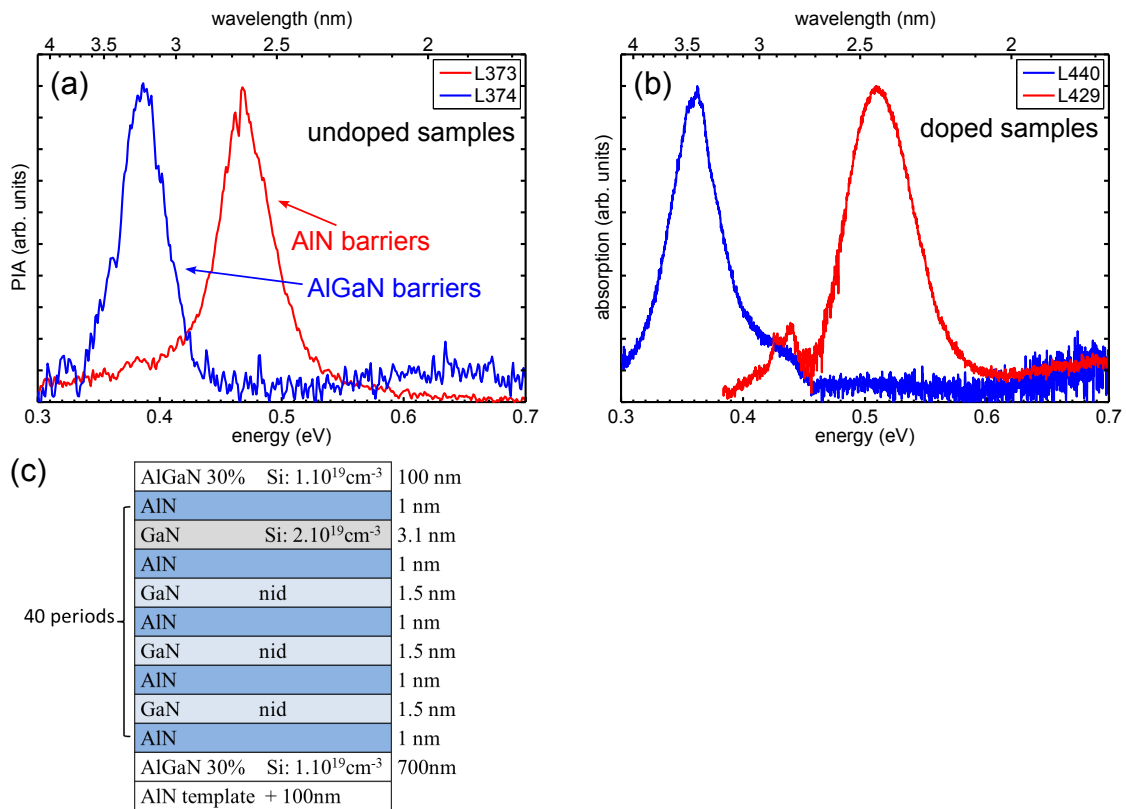


Figure 3.8 – (a) PIA of two undoped QCDs and (b) ISB absorption of similar structure with n-doped GaN QWs. For both figures, absorption was only observed under TM polarization. Undoped structures did not exhibit ISB absorption without interband pumping. (c) structure at 2.6 μm (samples L373 and L429)

samples exhibit a direct absorption in the IR. No signal was observed under TE-polarization, which confirms the ISB origin of this signal. Between L473 and L429 samples (having the AlN barriers), the blue shift is observed, as what has been reported for PA-MBE grown samples [119]. Concerning the other two samples, a red shift is observed, but is probably due to calibration issues of the AlGaN barrier. The absorption linewidths are quite narrow for all samples. The FWHMs range from 40 to 60 meV, which corresponds to state of the art values for GaN/(Al,Ga)N MQW structures. Only a slight increase of the FWHM is observed for the doped samples. Those results confirm the good quality of the grown structures. Interband PL have been performed on those samples, and energy broadening of 100-120 meV have been measured for the QW emission. There is factor 2 between interband and ISB emission linewidths, which is not surprising when considering the additional term $eL_w F$ for interband transitions.

It is interesting to note as well that on this figure 3.8, no ML fluctuations are resolved, as opposite to what is observed on good quality PA-MBE grown samples, with even higher

FWHM [68, 1]. This is neither observed on MOVPE grown samples [110]. This difference could be due to the large terraces induced by the Ga-rich growth conditions in PA-MBE.

Towards THz wavelengths:

Nowadays, GaN and related materials have also raised interest for ISB applications in the THz range, for the reasons explained in the previous chapter. The requirements for THz emitting devices are different: the thickness control is less restrictive since long wavelengths are achieved with wider QWs. Besides, those devices can feature low Al content AlGaN barriers, since the height of the confining potential is not a limiting factor anymore. The possibility to use low Al content barriers offers multiple advantages. First, the strain induced interface instability is much less critical, and higher quality substrate with lower dislocation densities than AlN templates be used. Moreover, low Al content barriers will suffer less from inhomogeneous broadening inherent with alloy inhomogeneities. This alloy broadening have been studied by Schubert *et al.* on thick AlGaAs layers by means of PL broadening [123]. Similar studies are reported on MOVPE grown AlGaN layers [124]. Inhomogeneous broadening has also been studied in NH₃-MBE grown GaN/Al_xGa_{1-x}N ($x \leq 0.35$) QWs [125]. Feltin *et al.* have reported PL linewidth as narrow as 10 meV for MOVPE grown single GaN QW with Al_{0.1}Ga_{0.9}N barriers [5]. Moreover, the low Al content will also reduce the electric field in the QW [126], enabling longer ISB wavelengths. Finally, the low band offset may enhance resonant tunneling and thus promote ultrafast transit times. A counterpart is that the control of doping level becomes more critical when going to THz wavelengths, because the low energy difference between the subband levels requires good accuracy on the Fermi levels to have only the first subband populated. Additionally, using low Al content AlGaN barriers does not allow ISB transition in THz, because of confinement from the triangular potential induced by the internal polarization. Band engineering is thus needed to achieve long wavelength ISB transitions. Possible solutions are stepped or graded QW [4] to cancel the electric field, or transitions between coupled QWs.

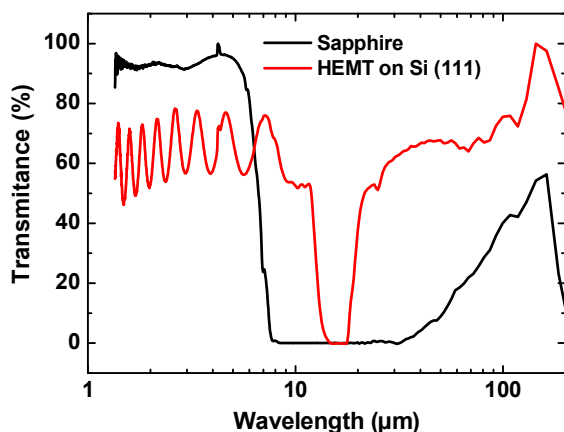


Figure 3.9 – Room temperature transmission measurements of GaN on Si (red) and sapphire substrates from near-IR to THz wavelength. Depicted from Ref. [120].

Another issue for THz applications is the substrate choice. The use of a transparent substrate in the targeted wavelength is preferable, particularly for preliminary studies, for instance to be able to use multipass waveguide configuration for absorption measurements. Fig. 3.9 shows the absorption of sapphire (black) and silicon (red). Sapphire, which is the standard substrate for near and mid-IR, presents a strong absorption for wavelengths above 7 μm . By contrast, Si remains almost transparent over a broad spectral range from near IR to THz. The absorption band observed between 12 and 20 μm is not due to the silicon substrate, but to the LO-phonon absorption of the deposited GaN layer. One should notice that at cryogenic temperatures, sapphire becomes transparent in this range, but this is not of high interest since we aim to demonstrate room temperature operation. Another possibility is to grow on low-dislocations density free-standing (FS) GaN substrates, that could increase significantly the quality of the material. However, those substrates, generally designed for laser applications, have a high n-type doping level, which makes them non transparent in the THz range, because free carriers absorption. One QCD structure for THz wavelengths has been grown both on FS GaN and on silicon (111) wafer, in order to benefit from high quality substrate and also carry out standard ISB standard characterization. However, only an unpolarized-induced photocurrent could be measured.

To conclude this part, NH_3 -MBE seems to offer a good compromise for short wavelength devices, cumulating the advantages of PA-MBE, such as sharp interfaces under optimized conditions and excellent thickness control, and the advantages of MOVPE, *i.e.* a growth temperature closer to equilibrium that induces less point defects. It should be pointed out, that for longer wavelength applications, MOVPE can become a competitive technique.

3.3 A two-color quantum cascade detector

This section presents the results obtained on the two-colors QCD reported in Ref. [127]. The structure was design by our collaborators at IEF in Paris. Growth and structural characterization have been performed at EPFL, ISB transmission spectroscopy, process and photocurrent measurements at IEF.

3.3.1 Design of the structure

The $e_1 e_3$ ISB transition, normally forbidden in square QWs, is made possible in III-nitrides heterostructures grown along on the (0001) polar axis thanks to the asymmetry induced from the internal electric field. This asymmetry has already been used to observe non linear effects, such as ISB resonant enhancement of second harmonic generation [128]. Here we propose to use it for a QCD detecting at two different wavelengths, corresponding to the $e_1 e_2$ and $e_1 e_3$ transitions. Multiple wavelength QWIPs have already been demonstrated using GaAs and

related alloys [129, 130]. Broad response QCDs have also been reported [131]. However, they all work using stacking of different active regions absorbing at different wavelengths. In this kind of geometry the electron extraction from one period to the other is more difficult, leading to a limited responsivity. Our design presents the advantage to have the same repeated active region, with the same absorbing QW. However, it should be noticed that this configuration does not allow wavelength discrimination.

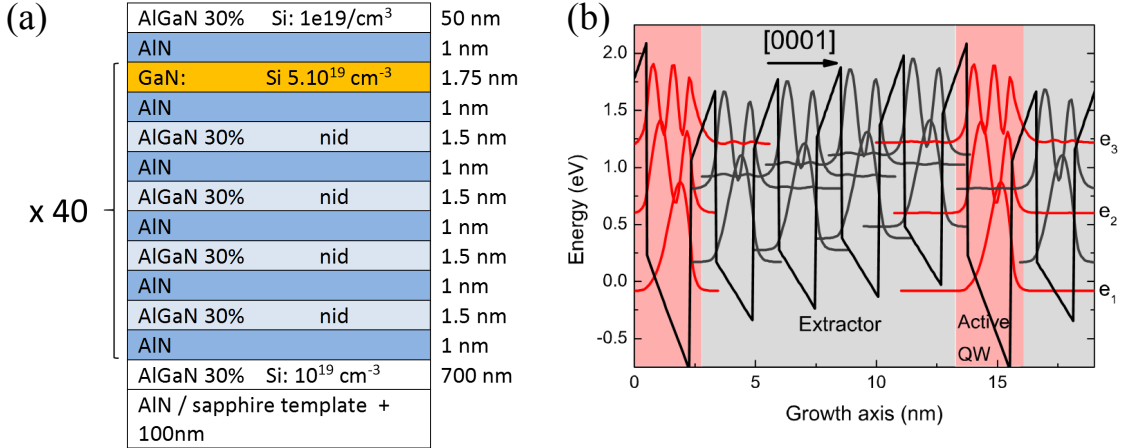


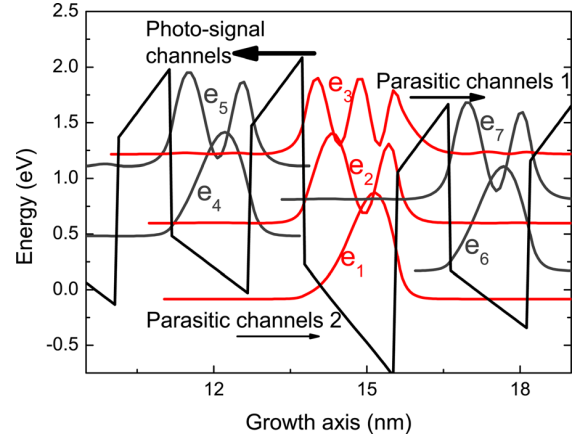
Figure 3.10 – Structure of the two wavelengths QCD (a) and its corresponding band profile (b).

The structure is presented in Fig. 3.10(a). Absorption occurs in the 1.75 nm thick GaN QW, which is nominally n-doped at $5 \times 10^{19} cm^{-3}$, surrounded by two 1 nm thick AlN barriers. The extractor is made of four non-intentionally doped 1.5 nm thick $Al_{0.3}Ga_{0.7}N$ QWs, separated by 1 nm AlN barriers. The whole active region is made of 40 periods. The active region is sandwiched between two thick $Al_{0.3}Ga_{0.7}N$ layers, doped at $10^{19} cm^{-3}$, of 700 and 50 nm for the bottom and top respectively. Fig. 3.10(b) shows the conduction band profile of one period of the sample. Simulations have been performed with Nextnano software [39] using a 8 bands $\mathbf{k} \cdot \mathbf{p}$ model. The GaN QW have three subband levels, raising ISB energies of 0.7 and 1.3 eV (corresponding to 1.7 and 1 μm wavelength) for the $e_1 e_2$ and $e_1 e_3$ transitions, respectively. The calculated oscillator strengths are 3.56 and 0.17 respectively. As can be seen on the band structure, each of the two excited levels of the absorbing QW can be coupled to two different parallel extracting cascades. The lower cascade extracts the electrons from level e_2 , whereas the upper one extracts the excited electrons from the e_3 level. The extracting SL is engineered with an average electric field of 0.3 MV/cm, resulting in a energy level difference of 85 meV between each subsequent QWs of the cascade. This energy is intentionally close to the LO-phonon energy to enhance the transfer rate *via* multiple LO phonon emission.

The transfer mechanisms have been estimated from calculations, using the Fröhlich electron-phonon model detailed in Ref. [104]. The scattering time have been calculated for the different levels represented in Fig. 3.11. If an electron is excited from level $|1\rangle$ to level $|2\rangle$, one wants

3.3. A two-color quantum cascade detector

Figure 3.11 – conduction band diagram close to the active QW, showing the levels taken into account in the efficiency calculations. The photo-generated electrons should be extracted towards the left to raise a photocurrent; other mechanisms are parasitic and hinder the responsivity.



to get maximal extraction towards level $|4\rangle$, the first level of the extracting cascade. However, this transfer is in competition with two parasitic relaxation processes: one to the ground state ($|2\rangle \rightarrow |1\rangle$), and one to the previous cascade ($|2\rangle \rightarrow |6\rangle$). The extraction efficiency from $|2\rangle$ is given by the following formula:

$$\eta_2 = \tau_{24}^{-1} \tau_2, \quad (3.18)$$

where τ is the lifetime in $|2\rangle$: $\tau_2^{-1} = \sum_i \tau_{2i}^{-1} = \tau_{21}^{-1} + \tau_{24}^{-1} + \tau_{26}^{-1}$ in the model. For level $|3\rangle$, two extracting channels exist: the first one *via* the upper cascade ($|3\rangle \rightarrow |5\rangle$), or by relaxation to the second level ($|3\rangle \rightarrow |2\rangle \rightarrow |4\rangle$). The efficiency is then:

$$\eta_3 = \eta_{35} + \eta_{324} = \tau_{35}^{-1} \tau_3 + \eta_2 \times \tau_{32}^{-1} \tau_3 \quad (3.19)$$

The calculated scattering times ($\tau_2=73$ fs, $\tau_{24}=279$ fs, $\tau_3=46$ fs, $\tau_{35}=185$ fs and $\tau_{32}=107$ fs) give the finally extraction efficiencies $\eta_2=26\%$ and $\eta_3=36\%$. Besides, the parasitic relaxations $|2\rangle \rightarrow |6\rangle$ and $|3\rangle \rightarrow |7\rangle$ appear to be negligible from the simulations

3.3.2 Growth and structural characterization

This structure is grown on AlN template by NH_3 -MBE, following the procedure explained in section 3.2.3. The growth rates were set to 0.45 ML/s and 0.19 ML/s for GaN and AlN, respectively (calibrated with RHEED oscillations), which gives an Al content of 30%. The Al content in the cladding layers is close to the average Al content of the active region, in order to reduce the band bending and minimize the strain over the active region. The ammonia flow was set to 80 sccm. The AlGaIn layers have been grown at 820°C, and the GaN QWs at 800°C, and growth interruptions were performed between GaN and the AlN barriers as described previously.

Following the growth the sample is characterized by XRD. Fig. 3.12(a) presents the $2\theta - \Omega$ diffractogram of the sample around the (0002) symmetric reflection. The number of resolved

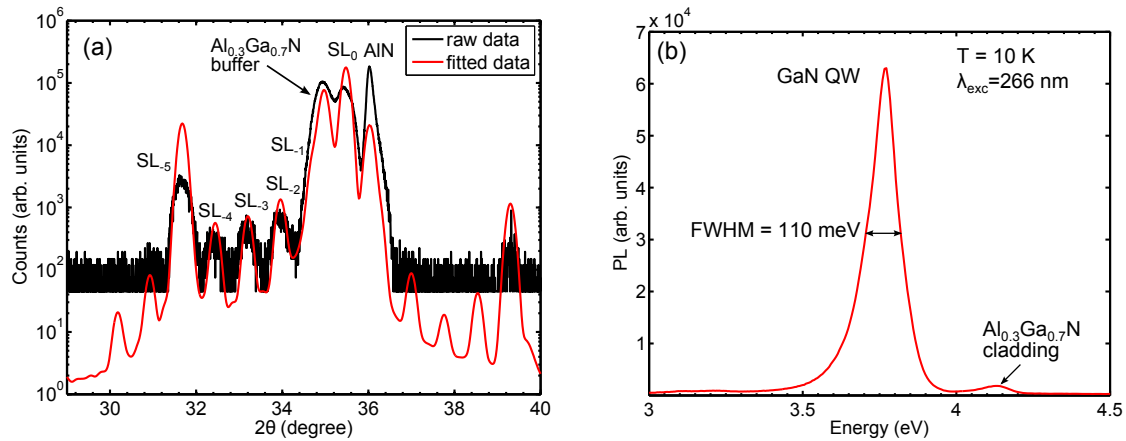


Figure 3.12 – (a) 2θ - Ω scan around the (0002) reflexion of sample L294. Fit of the data (in red) attests a thickness deviation lower than 5%. (b) interband PL spectrum of L294 at $T=10$ K.

satellite peaks of the SL confirms the good periodicity of the structure. The best fit (presented in red on the figure) is obtained for AlN barriers of 1 nm, AlGaN QWs of 1.41 nm and a GaN QW of 1.68 nm. Those values are very close to the nominal structure and correspond to a deviation of 5%. Concerning the thick AlGaN layer, fitting assuming a complete relaxation gives a value of 28% Al content instead of 30% nominally. Fig. 3.12(b) presents the PL spectrum at 10 K under the excitation of a laser at 266 nm. The maximum energy peak at 3.77 eV (above E_g) corresponds to the expected value for the QW emission, accounting for the confinement energy in such a narrow QWs. A less intense peak at 4.14 eV (to be more accurate the localization energy should be measured) is ascribed to the thick AlGaN layer, and gives a good agreement with the 30% Al nominal concentration, confirming the results obtained with XRD. The energy broadening of the QW emission is 110 meV. This value is slightly higher than what has been reported on AlN/GaN MQWs structures [132]. However, one should consider that the active region is grown on a thick AlGaN buffer and the structure is more complex than an AlN/GaN MQW. All these characterizations validate the good control of the growth parameters.

3.3.3 Process and characterization

Prior to the electrical characterization, the ISB transmission measurement is performed on the sample using a Fourier transform IR (FTIR) spectrometer. It consists of a Michelson interferometer having one moving mirror: the Fourier transform of the signal as function of the mirror position results in the spectrum. For the measurements, the sample edge is polished at 45° for multipass waveguide configuration. The number of pass in the active region is given by the following formula:

$$1 + \frac{L}{e},$$

3.3. A two-color quantum cascade detector

with e the thickness of the sample and L its length. For this specific sample, the number of passes was 8. A polarizer is positioned before the sample. The light enters with normal incidence to one facet, passes several times through the active region by total internal reflection and exits from the other facet (*cf.* Fig. 2.17). The signal is then measured by an InSb detector, and treated to obtain the spectrum. Finally, to get the transmission curve, the spectrum is subtracted from the spectrum of the reference sample, which is the substrate without the grown active region if one wants to get the absolute absorption. The blue curve of Fig. 3.14(a) shows the absorption spectrum of the sample. The sample absorbs at the expected $e_1 e_2$ energy of $1.7 \mu\text{m}$, with a FWHM of 93 meV. The weak oscillator strength does not enable to detect the $e_1 e_3$ ISB absorption peak. No absorption could be detected under TE polarized light, confirming the ISB origin of the signal.

For electro-optical measurements, the sample have been processed using standard optical lithography. $700 \times 700 \mu\text{m}^2$ mesas have been dry-etched by ICP with a Cl_2 mixture, using an SiO_2 mask. Then Ti/Al/Ti/Au ohmic contacts were deposited *via* e-beam evaporation. Fig. 3.13 shows a sketch and a photograph of the processed device.

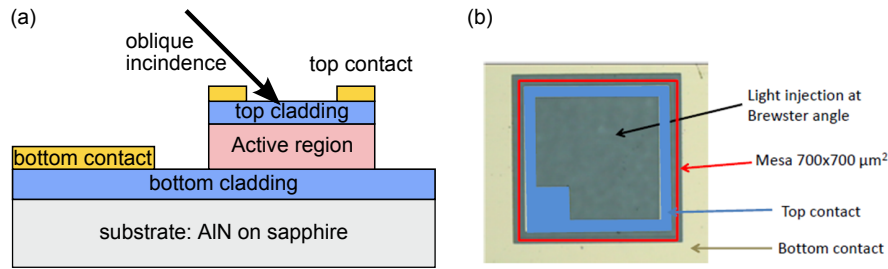


Figure 3.13 – (a) Scheme of a processed QCD and (b) optical microscopy image of a processed QCD ($700 \times 700 \mu\text{m}^2$ mesa).

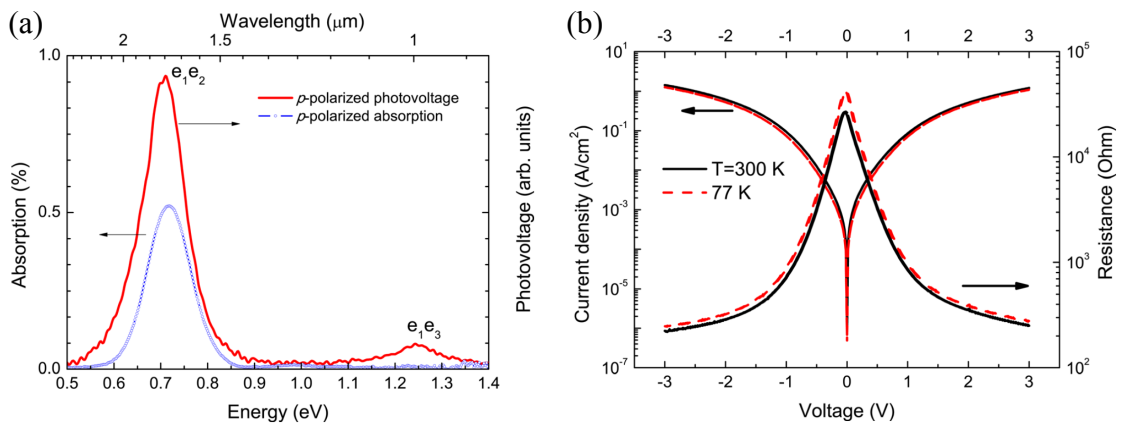


Figure 3.14 – (a) absorption (blue curve) and photovoltage (red curve) spectra under TM polarization measured at room temperature. (b) Current voltage and calculated resistance at 77 K and 300 K.

Standard current-voltage characterization have also been performed at 77 K and room temperature, using a Keithley 2636 parameter analyser and a probe station. Fig. 3.14(b) displays the measured curves and the calculated resistance. At zero voltage, the I-V curve is nearly symmetric, and the corresponding resistance is $\sim 60 \text{ k}\Omega$ (resp. $\sim 120 \text{ k}\Omega$) at 77 K (resp. 300 K). Due to the asymmetric band profile, one should expect an asymmetric I-V curve. This can be explained by the presence of parasitic leakage channels.

To collect the photovoltage spectra, the white source, coupled to the FTIR spectrometer, operated in the step-scan mode, is chopped mechanically at frequencies of few hundreds of Hz, and hits the sample surface at oblique incidence. A polarizer is positioned before the sample. The photovoltage (or photocurrent) detection is done synchronously to the modulated excitation using a lock-in amplifier. The red curve of Fig. 3.14(a) gives the photovoltage spectrum. The two peaks at 1.7 and 1 μm are observed, in agreement with the simulations. Those peaks are only observed under TM polarization only, and exhibit a FWHM of 100 and 83 meV, respectively. The photovoltage increases linearly with the pump power, and the responsivity at 77 K is estimated to 100 and 8 $\mu\text{A/W}$, for the 1.7 and 1 μm peaks, respectively. Those values are decreased by a factor of 1.6 at room temperature. These low values compared to others QCDs in the near-IR ($\sim 10 \text{ mA/W}$ in Ref. [3]) can be explained by the low absorption (probably resulting from a low doping level) and by the fact that the structure presenting two parallel extraction channels provides also more parasitic channels, compared to a single cascade design. Interestingly, the responsivity of the $e_1 e_3$ peak is only 12 times smaller than the $e_1 e_2$ peak, whereas the oscillator strength is more than 20 times smaller. This can be explained by a more efficient extraction of the higher energy level, since it is less confined (lower effective barrier) than the lower one. This is consistent with the calculations, giving a higher extraction efficiency of the e_3 level compared to the e_2 level. One can notice that 1 μm detection corresponds to the shortest wavelength ever reported for an ISB detector.

3.4 QCD using large AlGaN extractor

This section presents the results obtained on the large alloy extractor QCD. The results are based on Ref. [133]. The sample design, as well as processing and ISB characterization was performed at IEF. Then the growth by NH_3 -MBE and structural characterization was carried out at EPFL. Process and ISB characterization have been performed in Paris. More details about devices processing and characterization can be found in the thesis of S. Sakr [134].

3.4.1 Simulations and design

The short period extractor SL, which is generally used for QCDs, is complex in terms of structure design and growth control. Here we propose to replace it by a thick AlGaN layer.

The design takes advantage of the internal polarization of III-nitride heterostructures grown along the (0001) direction. The internal electric field makes the band structure asymmetric and favors one direction for electron extraction.

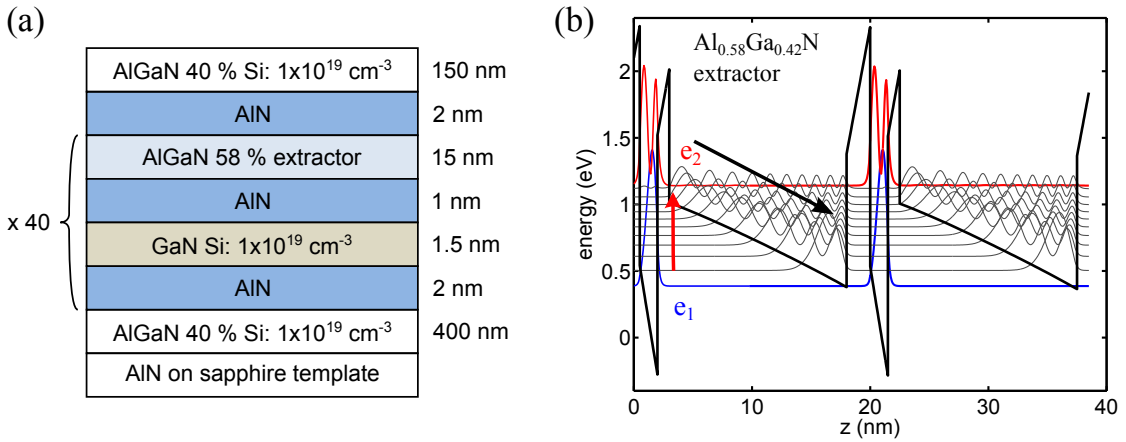


Figure 3.15 – Simplified alloy extractor QCD. Structure (a) and band-profile (b) of sample L430.

The sample structure and conduction band profile is given in Fig. 3.15. Each period of the active region consists in an absorbing GaN QW of 1.5 nm thickness surrounded by two AlN barriers. In order to enhance the extraction in the right direction, those two barriers are of different thicknesses: 2 nm for the left and 1 nm for the right. The GaN QW has two quantized states according to simulations and is nominally n-doped at 10^{19} cm^{-3} . The calculated ISB energy is 0.7 eV. After the 1 nm barrier, the large extractor is made of a non intentionally doped 15 nm thick $\text{Al}_{0.58}\text{Ga}_{0.42}\text{N}$ layer. The overall active region contains 40 periods. The electric field in the extractor is equal to 0.4 MV/cm. Contrary to the two-colors QCD, the electrons drift from left to right, *i.e.* from the substrate to the surface. The two contact regions are made of 400 and 150 nm thick (respectively for the bottom and the top contact) $\text{Al}_{0.4}\text{Ga}_{0.6}\text{N}$ layers doped at 10^{19} cm^{-3} . The average Al content in the active region is $\sim 60\%$, which is higher than the 40% of the contact region. This configuration is not ideal in terms of strain, however $\text{Al}_{0.4}\text{Ga}_{0.6}\text{N}$ was found to be a fair compromise to get good enough contacts.

This band-structure looks like the one proposed by Schneider and coworkers in the mid 90s for a photovoltaic QCD, as is it schematized in Fig. 3.2(a-b) [97, 96]. However, in those structures the electric field was achieved by a graded alloy or modulation doping. Our structure profits from the internal electric field, and no graded alloy nor modulation doping is necessary, which is of prime interest from a growth point of view. Besides, this design allows to achieve higher electric fields.

3.4.2 Growth and structural characterizations

The sample has been grown by NH_3 -MBE. The $\text{Al}_{0.4}\text{Ga}_{0.6}\text{N}$ cladding layer were grown at 850°C , under an ammonia flow of 30 sccm. The active region was deposited using 80 sccm ammonia flow and the substrate temperature was set to 800°C for the GaN QW. Growth interruptions have been performed between each GaN QW and the subsequent AlN barrier. The temperature was set to 830°C for the thick alloy extractor. The GaN QW was nominally doped at 10^{19} cm^{-3} . Two Ga cells have been used, the first one heated at 990°C giving a deposition rate of 0.32 ML/s, and the second one for the low flux was heated at 850°C corresponding to $v_{\text{GaN}}=0.15\text{ ML/s}$. The aluminium cell was heated to 1068°C giving $v_{\text{AlGaN}} = 0.21\text{ ML/s}$. This growth rate gives a Al composition of 40 % (resp. 58 %) when used together with first (resp. second) Ga cell. All growth rates have been calibrated by RHEED oscillations.

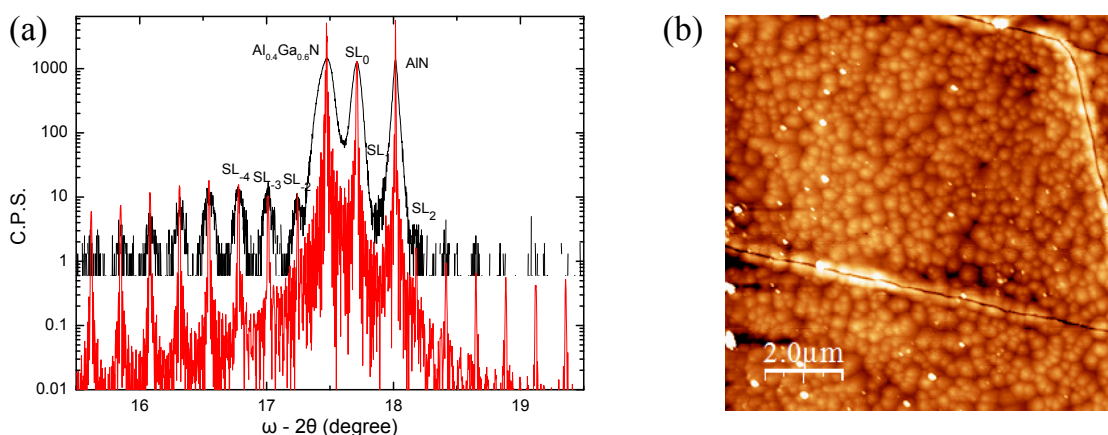


Figure 3.16 – (a) X-ray diffraction $2\theta - \Omega$ scan of L430 around the [0002] reflexion. The black curve corresponds to the measured data, and the red curve to the simulation. (b) AFM picture of L430 on a $10 \times 10\ \mu\text{m}^2$ window. The RMS surface roughness is 2.0 nm

XRD measurements were performed on the sample and are shown on Fig. 3.16. The satellite peaks are thin and numerous, which attests the good periodicity of the sample. Furthermore, the XRD data could be fitted, resulting in a period of 20.4 nm for the SL, corresponding to a deviation from the nominal structure lower than 2 MLs. Moreover, the best fit for the alloy extractor Al composition is obtained for $x_{\text{Al}} = 60 \pm 2\%$, corresponding to the nominal value.

Fig. 3.16(a) displays the AFM picture of the sample surface on a $10 \times 10\ \mu\text{m}^2$ scan area. The average surface roughness is lower than 2 nm. The surface exhibits a hillock morphology which is usual for GaN-based structures grown by NH_3 -MBE. It is attributed to kinetic roughening effects, as already pointed out by Veizian *et al.* [135]. The AFM picture also features some cracks on the sample surface. This issue will be discussed further. However those cracks did not bring dramatic consequences on the sample characterization, as it is shown in the following.

3.4.3 Characterization of the device

The sample has been then characterized and processed at IEF, in the same way as the two colors QCD. Absorption measurements were performed at room temperature, using a multipass waveguide configuration with polished facets at 45° , resulting in 12 passes through the active region. The result is given on Fig. 3.17(a) (blue curve). The absorption peak is detected only for TM polarized wave and is centered at 0.67 eV ($1.84 \mu\text{m}$) with a FWHM of 63 meV. This absorption comes from the e_1e_2 ISB transition of the 1.5 nm thick GaN QW. The total absorption at maximum is $8.5 \pm 0.1\%$, which corresponds to an absorption per QW of $\alpha = 1.77 \pm 0.18 \times 10^{-4}$. This value is much lower than expected. This discrepancy can be explained by a lower doping level than the nominal one and by the fact that the bottom cladding layer has a lower Al composition than the SL, which induces band bending and creates a depletion region at zero bias over the active layer.

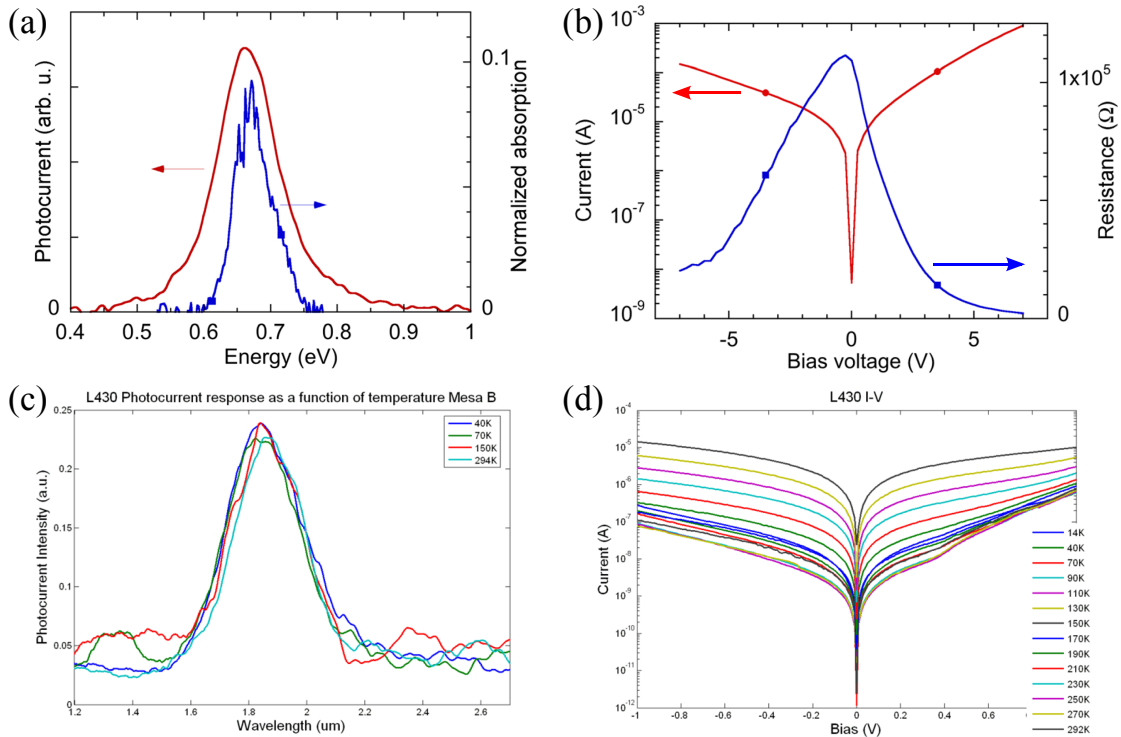


Figure 3.17 – (a) ISB absorption and photocurrent measurements of L430 sample. (b) Current-voltage characteristics of the sample at room temperature under TM-polarization. (c) Photocurrent measurements as function of the temperature. (d) Current-voltage measurements at different temperatures.

The red curve of Fig. 3.17(a) is the photocurrent spectrum measured at room temperature (in the same conditions as the two-colors QCD) on a $700 \times 700 \mu\text{m}^2$ device. The signal is only observed under TM-polarized excitation, as for the absorption signal. The peak is centered at $1.87 \mu\text{m}$, and has a FWHM of 103 meV. This broadening can be tentatively explained by

oblique transitions between the ground state of the QW and the quasi-continuum states of the extractor large layer. Indeed, even if the oscillator strengths of these transitions are small, the large number of states, plus the enhanced transfer efficiency can promote the photocurrent signal arising from those transitions. The measured responsivity at room temperature is $48 \pm 4 \mu\text{A/W}$. This value is quite small, mainly due to the low doping level and the inefficient coupling in the oblique incidence configuration. However, accounting for the very low ISB absorption and light coupling (proportional to the $\sin^2(r)/\cos(r)$, with r the refraction angle in the material), the maximal theoretical value (for an extraction efficiency $\eta_e=1$) of the response is expected to be $79 \mu\text{A/W}$. From this value the extraction efficiency is deduced to be $62 \pm 5 \%$, which is more than three times higher than standard GaN-based QCDs [3]. This high efficiency, which confirms the superiority of the large extractor design, is very promising and could lead to high responsivity detectors, with an improved design and growth control.

Fig. 3.17(b) is the current voltage characteristics at room temperature in dark conditions. The curve is asymmetric, which is expected from the conduction band profile. The zero bias resistance is around $1.47 \text{ k}\Omega \cdot \text{cm}^2$ at room temperature and $280 \text{ k}\Omega \cdot \text{cm}^2$ at 77 K. The access resistance due to the contact is measured *via* the transmission line method and is lower than $1 \text{ k}\Omega$. Fig. 3.17(d) shows the evolutions of the I-V curves with the temperature. The resistance is decreased by 4-5 orders of magnitude from room temperature to 10 K.

Another interesting feature of the sample is shown in Fig. 3.17(c) (it should be noticed that those measurements have been performed using plasmonic grating, as detailed in the next paragraph). The photocurrent has been measured depending on the temperature. The signal is very stable from 40 K to 294 K. No obvious broadening, nor wavelength shift is observed with the temperature. This is generally not the case for usual III-V QCDs, and this results endorses the robustness of the design.

3.4.4 Detection enhancement using plasmonic structures

In order to enhance the responsivity, the coupling efficiency of the incoming light should be improved. For this purpose, the L430 sample was regrown and plasmonic grating have been deposited on the surface to improve the coupling efficiency. This part was done in collaboration with Technion in Haifa. The results presented here are based on Ref. [136]. The idea to use grating to enhance ISB excitation is not new. In 1982, Heitmann *et al.* used plasmonic grating to excite ISB transitions in Si inversion layers [137]. In 1988, Helm *et al.* also used a grating to extract the THz ISB photoluminescence signal [49]. In 1992, grating couplers are used on QWIP to enhance the device efficiency [138]. The grating is used to scatter the light (coming either from the backside or frontside of the sample) in all directions, so that a part of it couples with the ISB dipole moment. Here, a grating with surface plasmon polaritons is presented. The advantage compared to other gratings is that the coupled light in

the layer is not scattered, but mainly supported by the TM-mode, which enhances even more the coupling.

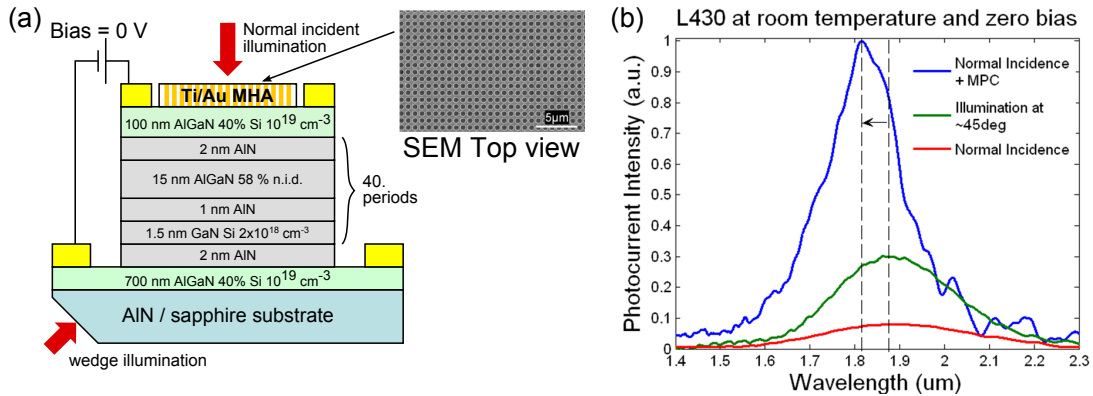


Figure 3.18 – (a) Schematic representation of the sample processed in TECHNION with SEM picture of the top of the sample with the metallic nanoholes array. (b) Measured photocurrent [136]

Fig. 3.18(a) is a schematics of the processed device. The process steps are the same as previously described, using a similar mask ($700 \times 700 \mu\text{m}^2$ mesas). The difference is in the metallic grating deposited at the surface. It consists of a Ti/Au (5 nm/200 nm) layer. The holes are patterned with a focused ion beam. The inset of the figure is a top view SEM image of the grating: the hole diameter is 580 nm and the period is 835 nm. The structure is designed to achieve a plasmon resonance near to the working wavelength of the QCD. The photovoltage is presented in Fig. 3.18(b). The response is increased by a factor of 3 compared to 45° illumination scheme and by a factor of 30 with respect to normal incidence geometry without grating. Notice that, this last value is expected to be zero. However scattering due to surface roughness, cracks on the sample surface, or scattering at the sidewall of the mesa can help coupling the light at normal incidence. Interestingly the linewidth of the spectrum is three times larger (300 meV) with the grating.

These results are promising for future prospects, since this approach not only improves the response signal, but has potential applications such as focal plane array (FPA) QCDs. Furthermore, the plasmon grating can be easily scaled to longer wavelengths up to the THz range.

3.4.5 Growth issues and strain engineering on alloy extractor QCD

As seen on the AFM picture (Fig. 3.16(b)), the QCD featuring thick extractor exhibits cracks at the surface. The optical microscope image (Fig. 3.19 (right)) attests that the sample is fully covered with cracks. As a reminder, L430 structure is grown on an AlN template. The active layer, which has an average Al content of 60 %, is grown on a doped buffer layer having an

Al content of 40 %. This choice, not favourable in terms of strain, was however found to be a compromise between material quality, and ohmic contacts. This active layer has around 1 μm thickness, which is confirmed by the cross section SEM image displayed in Fig. 3.19 (right).

In order to analyze the origins of those cracks, XRD measurements have been performed on similar samples. Reciprocal space mappings have been done in the neighbouring of the $(10\bar{1}5)$ asymmetric reflection. Contrary to the symmetric reflections (like (0002) or (0004)), the maps in asymmetric directions give information about both the a and c parameters using the following formulas for an $(hki\bar{l})$ reflection:

$$c = l \frac{1}{q_z} \quad \text{and} \quad a = h \frac{2}{\sqrt{3}} \frac{1}{q_x}, \quad (3.20)$$

where q_z and q_x are the coordinates of the peak in the reciprocal space (usually given in nm^{-1} or in \AA^{-1}). This enables the simultaneous determination of the alloy content and relaxation of the layer.

Fig. 3.20 reports reciprocal space maps in both the (0004) and $(10\bar{1}5)$ directions. In the (0004) direction no particular features are observed, except for the satellite peaks of the SL. Concerning the $(10\bar{1}5)$, data analysis leads to several conclusions. On Fig. 3.20(b), the strongest and thinnest peak at $(q_x = 0.371 \text{\AA}^{-1}, q_z = 1.004 \text{\AA}^{-1})$ giving $a = 3.112 \text{\AA}$ and $c = 4.98 \text{\AA}$) corresponds to the AlN buffer layer. Below this, a very large peak is observed. This corresponds to the $\text{Al}_{0.4}\text{Ga}_{0.6}\text{N}$ buffer layer. At first, the layer is strained to the ALN (having the same a parameter). Then, during the growth the layer partially relaxes (the oblique line corresponds to fully relaxed layers). The calculated relaxation is $\sim 65\%$. From the peak, one can see that the a parameter increases (q_x decreases in the reciprocal space) until the partially relaxed value and the c parameter increases (q_z decreases). Then the active region, having an average Al content of 60 %, is under tensile strain. Above a certain critical thickness, this tensile strain relaxes through the formation of cracks. As can be seen on the figure, there are two parallel SL signatures, represented by the two vertical lines at $q_x = 0.3665 \text{\AA}^{-1}$ and $q_x = 0.3675 \text{\AA}^{-1}$. This indicates a plastic relaxation during the growth, *i.e.* the formation of cracks. The zeroth order of the superlattice is first under tensile strain (on the left of the relaxation line) and is denoted $SL_{0,A}$. After the plastic relaxation, the $SL_{0,B}$ is fully relaxed. Another sample was grown, identical to this one but with 20 periods instead of 40. The reduction of the active regions thickness (below the critical thickness) resulted in a crack-free sample.

For mid-IR QCDs, the design have been adapted to avoid crack formation, by using a lower Al content in the extractor region, and using buffer layers having the same Al content as the active region in average. Fig. 3.21 gives two examples of different thick alloy extractor QCDs. The first and second structures feature respectively an $\text{Al}_{0.25}\text{Ga}_{0.75}\text{N}$ and an $\text{Al}_{0.35}\text{Ga}_{0.65}\text{N}$ buffer layer, which are matched to the average Al content of the active region. On the two reciprocal

3.4. QCD using large AlGaIn extractor

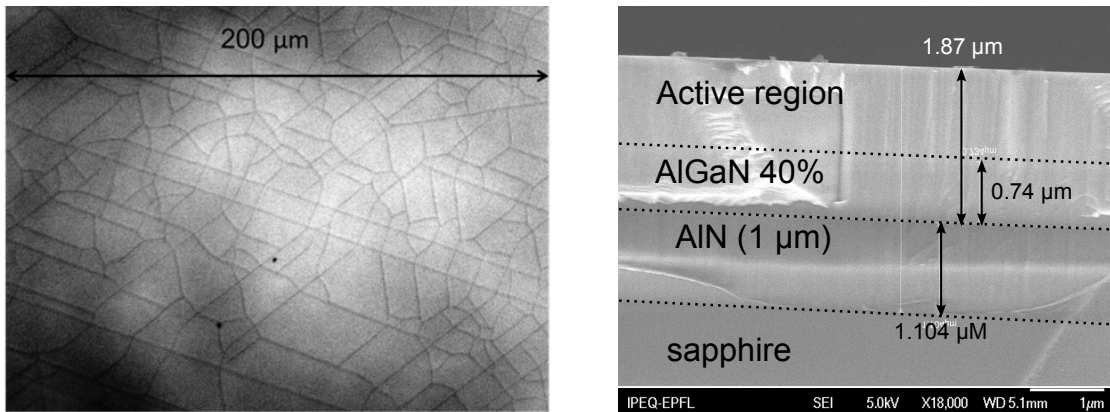


Figure 3.19 – Optical microcope image (left) and cross section SEM image (right) of the L430 sample.

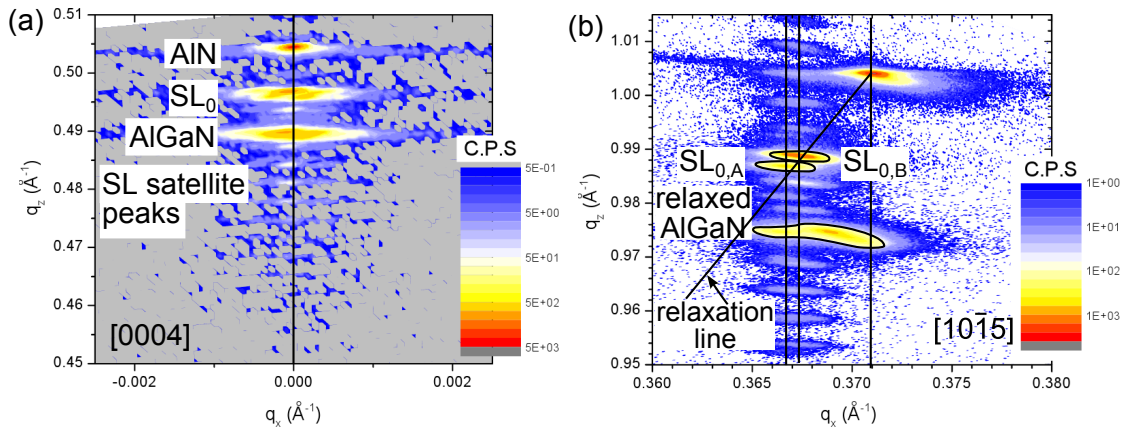


Figure 3.20 – XRD reciprocal space maps of the cracked L430 sample around the (a) [0004] and (b) [10 $\bar{1}$ 5] reflection.

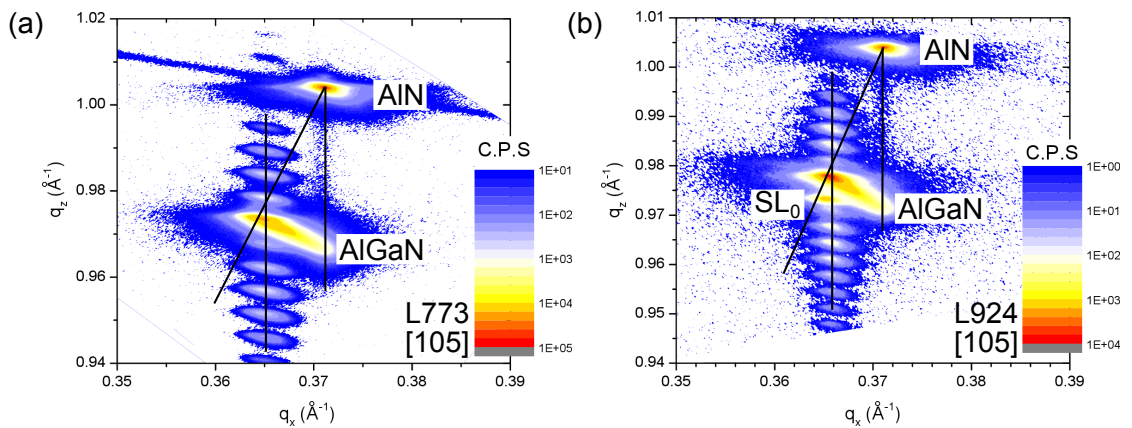


Figure 3.21 – XRD reciprocal space maps of two different samples that did not exhibit cracks.

space maps, one can see that the AlGa_N layers are nearly fully relaxed (the peak coincide with the relaxation line), and the SLs are perfectly strained on them.

3.5 Conclusion and Outlooks

To conclude this chapter, we have demonstrated that the growth optimization with NH₃-MBE could lead to QCDs with competitive performance compared to PA-MBE grown devices [78]. We demonstrated a two color QCD exhibiting a photocurrent at 1.7 and 1 μm originating respectively from the e_1e_2 and the e_1e_3 transitions. This was made possible thanks to the electric field induced asymmetry. It worth to be noticed that 1 μm is the shortest operating wavelength ever reported for an ISB optoelectronic device. This device evidences efficient electron transport in SL. However, the transport is not mediated by resonant tunneling nor miniband states, but by LO-phonon assisted multiple scattering. The low responsivity could be further improved by increasing the doping levels and achieving a better material quality. The second sample is a QCD with a simple extractor region made of a 15 nm thick Al_{0.58}Ga_{0.42}N layer. The active region is similar to the photovoltaic QWIP developed by H. Schneider *et al.* in the mid 90s [97, 96]. From a growth point of view, this structure is more robust against thickness fluctuations, as attested by the XRD measurements. This simplified device, is advantageous, and should enable ultrafast operation *via* an efficient electron transfer. Besides, the photocurrent showed a very good stability with temperature, where no degradation nor shift of the signal was observed from 40 K to room temperature. The low responsivity at oblique incidence could be enhanced by a factor of three, using a plasmonic grating at the surface, allowing coupling of normal incident light with the ISB dipole moment. This result is of particular interest in prospect of potential applications, such as FPA detectors. Growth issues such as cracks on the surface could be overcome by reducing the active region thickness or using a strain engineered cladding layer for mid-IR applications. Other QCDs have been grown for operation in the mid-IR. ISB absorption was measured and one sample exhibited photocurrent at 4.7 μm.

QCDs working in the THz regime would be a step further. However, the model of multiple LO-phonon emission cascade is not applicable for photovoltaic detectors absorbing below the LO-phonon energy. The thick alloy extractor could then be an attractive option. Another solution could be based on miniband transport for the extractor. For this purpose, one has to demonstrate the resonant tunneling, which is the object of the next chapter.

Several samples have been grown for THz range operation on different substrates like silicon or FS GaN, using a step QW geometry, but only an unpolarized photocurrent was detected. The material quality has to be improved. Recent progress on substrate quality are part of the solution. MOVPE could also be a good choice for THz applications, since the high growth

temperatures should generate less defects in the materials.

4 Unipolar vertical transport in (Al,Ga)N/GaN heterostructures

4.1 Principles and motivations for the resonant tunneling diodes

The term of tunneling refers to the ability of an electron, or any quantum object to cross a potential barrier, which has a higher energy than its own. This phenomenon is forbidden in the classical mechanics, however, when the mass of the object becomes very small and the barrier very thin, the object penetrates the barrier, and the presence probability is an evanescent wave with an exponential decay. Therefore, if the barrier thickness is of the same order of magnitude as the decay length, the tunneling probability becomes non negligible. This is a manifestation of the wave-nature of the quantum objects.

An extension of this tunneling effect is called resonant tunneling. A resonant tunneling diode (RTD) consists in an undoped QW sandwiched between two thin barriers (Fig. 4.1(a)). The electron energy is quantized in one direction. If an incoming electron has the same energy as the resonant level in the QW, the transmission energy across the whole structure is resonantly enhanced. The transmission coefficient can be close to one. This mechanism is analogous to a Fabry-Perot interferometer, and can be also explained in terms of waves interference: at the resonance, the interference will be constructive in the forward direction and destructive in the backward direction, hence the transmission probability becomes close to one. From a theoretical point of view, tunneling in double barrier structure has been studied by Bohm [139] using the Wentzel–Kramers–Brillouin (WKB) semi-classical approximation, and by Kane, using the calculation of the wave functions [140]. The first RTD was demonstrated by the group of Leo Esaki at IBM Research in 1974 [141]. This result was the first evidence of the existence of quantized states in a semiconductor QW. The current-voltage characteristics is depicted in Fig. 4.1(b), where the conductance becomes clearly negative at a ~ 0.8 V bias voltage.

Over the past decade, RTDs based on III nitride semiconductors have been of particular interest. They indeed present a twofold interest. First, since resonant tunneling is a very fast charge transport mechanism, they can be used as oscillators to emit in the far infrared. Secondly, they form a key element to understand vertical transport across SLs, a necessary milestone for the realization of a QCL. Resonant tunneling assumes a ballistic transport and is in competition with numerous parasitic non-coherent transport mechanisms, such as impurities or deep levels mediated tunneling, dislocations assisted transport, phonon scattering, *etc.* Therefore, due to the difficulty to get high quality materials, demonstration of a GaN-based RTD remains a highly challenging task.

In this chapter, we discuss the mechanism of resonant tunneling, and the different existing models. In a second part, we present an quasi-exhaustive review of previous works related to GaN-based RTDs, emphasizing the different controversies, the issues encountered, and the remaining challenging tasks.

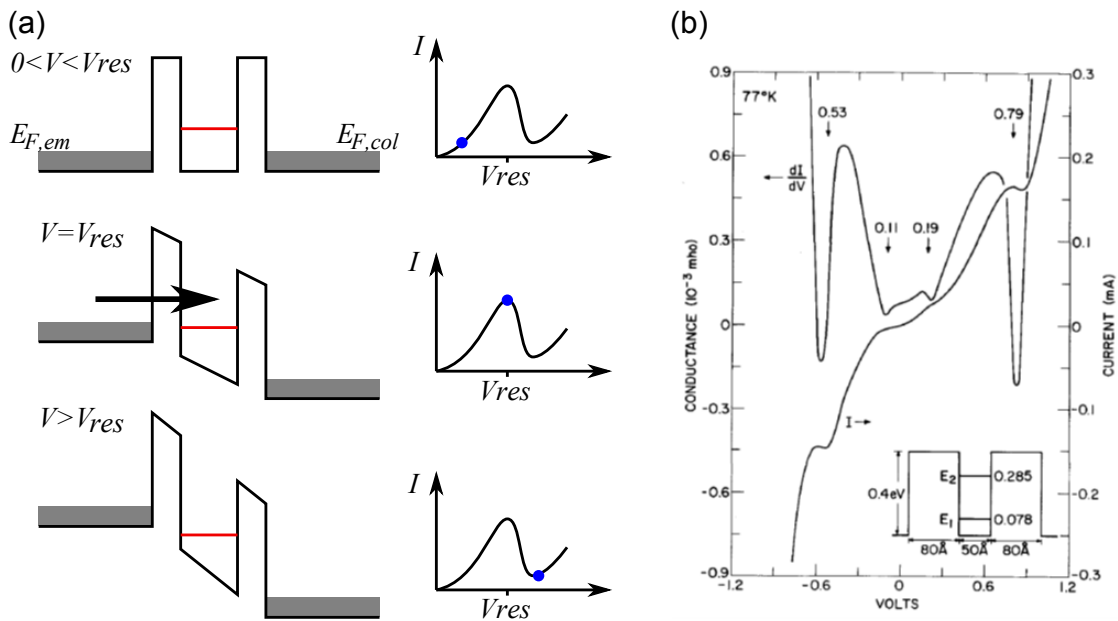


Figure 4.1 – (a) Mechanism of resonant tunneling in a double barrier RTD. Left: band profile under different bias potential, right: I-V curve. (b) I-V characteristics of the first demonstration of resonant tunneling in double barriers RTDs (reproduced from Ref. [141]).

4.2 Physics of resonant tunneling: the coherent transport model

4.2.1 Luryi's picture

A simple approach to explain the appearance of a negative resistance, when passing current through a double barrier RTD, was presented by Luryi *et al.* [142]. This explanation is based

4.2. Physics of resonant tunneling: the coherent transport model

on the energy conservation of the electron crossing the structure. In the QW, the energy is quantized only in the z direction, and can thus be written as:

$$E = E_0 + \frac{\hbar^2}{2m^*} (k_x^2 + k_y^2). \quad (4.1)$$

In the bulk, the energy is simply written:

$$E = \frac{\hbar^2}{2m^*} (k_x^2 + k_y^2 + k_z^2). \quad (4.2)$$

If one assumes the momentum conservation along the x and y directions (*i.e.* ballistic transport), then:

$$\frac{\hbar^2}{2m^*} k_z^2 = E_0. \quad (4.3)$$

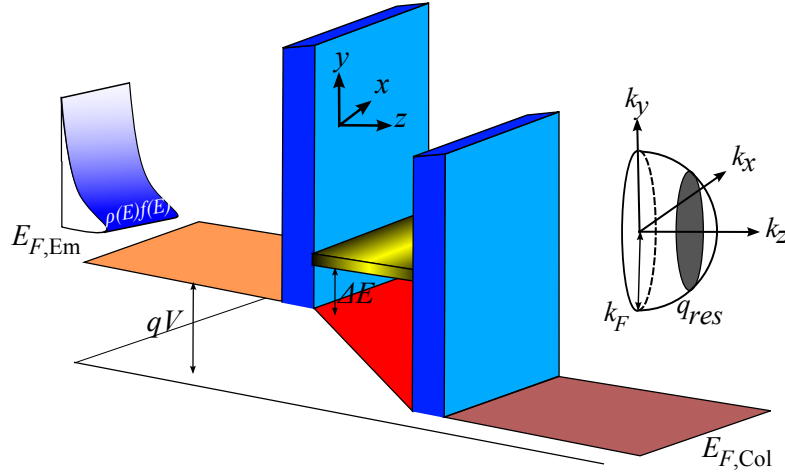


Figure 4.2 – RTD energy band diagram with the Fermi sphere of the electron coming from the emitter

In the emitter, at zero temperature, all the electrons are in the Fermi sphere of radius

$$k_F = \sqrt{2m^* E_F^{em} / \hbar^2},$$

where E_F^{em} is the quasi Fermi level in the emitter region. Considering the relation 4.3, the electrons that are able to tunnel are those at the intersection between the fermi sphere and the $k_z = k_R = \sqrt{2m^* E_z / \hbar^2}$ plane (see figure 4.2). This intersection is a disk, which has an area proportional to

$$k_F^2 - k_R^2 \propto E_F^{em} - E_0. \quad (4.4)$$

Since E_F^{em} is proportional to the applied voltage, the tunneling current will be first zero, then proportional to the voltage, and zero again when the energy level of the QW is below the

conduction band-edge energy in the emitter.

4.2.2 Esaki's transport model

Leo Esaki [143] has developed a formalism to compute the coherent tunneling (*i.e.* conservation of the wave vector) current across a quantum structure. Let's suppose that the transmission coefficient, called $T(E)$ is known (See the next section for the calculation of this function using the transfer matrix method), where E corresponds to the incident wave energy. Then the tunneling currents can be written as:

$$J = J_{\rightarrow} - J_{\leftarrow}, \quad (4.5)$$

where J_{\rightarrow} are the currents in the forward/backward directions. Let's consider the current in the forward direction. We have then:

$$J_{\rightarrow} = 2 \sum_{k_x, k_y, k_z > 0} e v_z T(E_z) f_{em}(\mathbf{k}) (1 - f_{col}(\mathbf{k})), \quad (4.6)$$

where e is the electron charge, v_z the group velocity in the z direction, and the functions $f(\mathbf{k})$ are the Fermi-Dirac occupation factors:

$$\begin{aligned} f_{em,col}(\mathbf{k}) &= \frac{1}{1 + \exp\left(\frac{1}{k_B T} (E - E_F^{em,col})\right)} \\ &= \frac{1}{1 + \exp\left(\frac{1}{k_B T} \left(\frac{\hbar^2}{2m^*} (k_x^2 + k_y^2 + k_z^2) - E_F^{em,col}\right)\right)}. \end{aligned} \quad (4.7)$$

Using the following formula of the group velocity:

$$v_z = \frac{1}{\hbar} \frac{\partial E_z}{\partial k_z},$$

equation 4.6 becomes:

$$\begin{aligned} J_{\rightarrow} &= \frac{2e}{\hbar(2\pi)^3} \iiint_{k_x, k_y, k_z > 0} \frac{\partial E_z}{\partial k_z} T(E_z) f_{em}(\mathbf{k}) (1 - f_{col}(\mathbf{k})) dk_x dk_y dk_z \\ &= \frac{2e}{\hbar(2\pi)^3} \int_0^{\infty} T(E_z) \left[\int_0^{\infty} f_{em}(E_z + E_{\parallel}) (1 - f_{col}(E_z + E_{\parallel})) 2\pi k_{\parallel} dk_{\parallel} \right] dE_z \\ &= \frac{m^* e}{2\hbar^3 \pi^2} \int_0^{\infty} T(E_z) \underbrace{\left[\int_0^{\infty} f_{em}(E_z + E_{\parallel}) (1 - f_{col}(E_z + E_{\parallel})) dE_{\parallel} \right]}_{I_{\rightarrow}(E_z)} dE_z \end{aligned} \quad (4.8)$$

4.2. Physics of resonant tunneling: the coherent transport model

From this equation, the total current can be written:

$$J = J_{\rightarrow} - J_{\leftarrow} = \int_0^{\infty} T(E_z) S(E_z) dE_z, \quad (4.9)$$

where $S(E_z)$ is called the supply function, and can be easily calculated from the integrals $I_{\rightarrow}(E_z)$ and $I_{\leftarrow}(E_z)$:

$$S(E_z) = \frac{m^* e}{2\hbar^3 \pi^2} (I_{\rightarrow}(E_z) - I_{\leftarrow}(E_z)) = \frac{m^* e k_B T}{2\hbar^3 \pi^2} \ln \left(\frac{1 + \exp\left(\frac{1}{k_B T} (E_F^{em} - E_z)\right)}{1 + \exp\left(\frac{1}{k_B T} (E_F^{col} - E_z)\right)} \right). \quad (4.10)$$

In the low temperatures limit, the supply function has a simple expression, which is independent of E_z and is a piecewise linear function:

$$S(E_z) = \begin{cases} \frac{m^* e}{2\hbar^3 \pi^2} (E_F^{em} - E_F^{col}) & \text{if } E_z < E_F^{col} < E_F^{em} \\ \frac{m^* e}{2\hbar^3 \pi^2} (E_F^{em} - E_z) & \text{if } E_F^{col} < E_z < E_F^{em} \\ 0 & \text{if } E_F^{col} < E_F^{em} < E_z \end{cases}. \quad (4.11)$$

As it is explained in the next section, the transmission coefficient for a QW that has a quantized state of energy E_0 , has a strong peak at E_0 and is almost zero elsewhere. In other words, the transmission function can be written as $T(E_z) \propto \delta(E_z - E_0)$. In this case, one finds the current to be proportional to $E_F^{em} - E_0$, which is exactly the obtained result in the previous section. However, the determination of the $I - V$ characteristics requires the calculation of the transmission function $T(E_z)$, which depends on the band profile modulated by the applied voltage V .

4.2.3 Transmission coefficient calculation: transfer matrix model

The transfer matrix method is a convenient way to compute the transmission coefficient of a RTD under different biases. It consists in discretizing the potential on different segments and considering plane waves in each segment. Let's consider the stationary Schrödinger equation in the effective mass approximation:

$$H\Psi(z) = -\frac{\hbar^2}{2} \nabla \left(\frac{1}{m^*(z)} \nabla \right) \Psi(z) + V(z)\Psi(z) = E_z \Psi(z), \quad (4.12)$$

where m^* is the effective mass and $V(z)$ the potential. This potential is approximated as a constant piecewise function, as shown on figure 4.3. Therefore, the wave function corresponding to the energy E_z on the n^{th} segment can then be written as a planewave:

$$\Psi_n(z) = A_n \exp(ik_{z,n}z) + B_n \exp(-ik_{z,n}z), \quad (4.13)$$

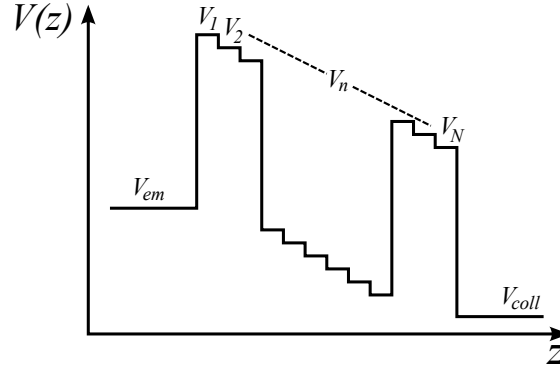


Figure 4.3 – Constant piecewise potential of a double barrier RTD used for the transfer matrix calculations.

where $k_{z,n}$ is the complex wavenumber associated to the energy E_z :

$$k_{z,n} = \frac{\sqrt{2m_n^*(E_z - V_n)}}{\hbar} \quad (4.14)$$

which can be real or imaginary, depending on the sign of $(E_z - V_n)$. At each interface, the wavefunction should fulfill the continuity relations:

$$\begin{cases} \Psi_n(z_n) = \Psi_{n+1}(z_n) \\ \frac{1}{m_n^*} \Psi_n'(z_n) = \frac{1}{m_{n+1}^*} \Psi_{n+1}'(z_n) \end{cases} \quad (4.15)$$

Those conditions can be written in a matrix form, using the wavefunction from equation 4.14:

$$\begin{aligned} \begin{pmatrix} e^{ik_n z_n} & e^{-ik_n z_n} \\ \frac{ik_n}{m_n} e^{ik_n z_n} & \frac{-ik_n}{m_n} e^{-ik_n z_n} \end{pmatrix} \begin{pmatrix} A_n \\ B_n \end{pmatrix} &= \begin{pmatrix} e^{ik_{n+1} z_n} & e^{-ik_{n+1} z_n} \\ \frac{ik_{n+1}}{m_{n+1}} e^{ik_{n+1} z_n} & \frac{-ik_{n+1}}{m_{n+1}} e^{-ik_{n+1} z_n} \end{pmatrix} \begin{pmatrix} A_{n+1} \\ B_{n+1} \end{pmatrix} \\ \Leftrightarrow M_n(z_n) \begin{pmatrix} A_n \\ B_n \end{pmatrix} &= M_{n+1}(z_n) \begin{pmatrix} A_{n+1} \\ B_{n+1} \end{pmatrix} \\ \Leftrightarrow \begin{pmatrix} A_n \\ B_n \end{pmatrix} &= M_n(z_n)^{-1} M_{n+1}(z_n) \begin{pmatrix} A_{n+1} \\ B_{n+1} \end{pmatrix}. \end{aligned} \quad (4.16)$$

From this last equation, one can deduce the general relation:

$$\begin{aligned} \begin{pmatrix} A_1 \\ B_1 \end{pmatrix} &= M_1(z_1)^{-1} M_2(z_1) M_2(z_2)^{-1} M_3(z_2) \dots M_N(z_N)^{-1} M_{N+1}(z_N) \begin{pmatrix} A_{N+1} \\ B_{N+1} \end{pmatrix} \\ &= \mathcal{M} \begin{pmatrix} A_{N+1} \\ B_{N+1} \end{pmatrix} \end{aligned} \quad (4.17)$$

4.2. Physics of resonant tunneling: the coherent transport model

\mathcal{M} is the transfer matrix and is computed numerically. However, there exists an analytical solution of the matrix in the case of simple symmetric DB structure without any electric field [144, 145]. Knowing that $B_{N+1} = 0$, which means that there is no reflected beam in the collector region, and that the intensity of the transmitted wave is proportional to $|A_{N+1}|^2$, the transmission coefficient can be simply deduced:

$$T(E_z) = \frac{k_{N+1}/m_{N+1}^*}{k_1/m_1^*} \frac{|A_{N+1}|^2}{|A_1|^2} = \frac{k_{N+1}}{k_1} \frac{1}{|\mathcal{M}_{11}|^2}. \quad (4.18)$$

An example of a transfer matrix calculation is shown on figure 4.27.

Another interesting figure can be extracted from this transmission function: the FWHM of $T(E_z)$ at a resonance peak, noted Γ . From this number, one can deduce the dwelling time of the tunneling electron in the DB structure:

$$\tau_0 = \hbar/\Gamma. \quad (4.19)$$

This result can be easily interpreted from the time-energy uncertainty relation. However, this is a very good approximation for coherent tunneling at the resonance. This dwelling time has been subject of different theoretical works. It can be more accurately calculated using the Wigner formula [146]:

$$\tau = \hbar \frac{\partial \delta}{\partial E_z},$$

where δ represents the phase shift. It has been as well calculated by simulating the transient time of a wave packet across the structure [147], all giving similar results as equation 4.19. τ_0 is strongly dependent on the structure (barrier height, well and barriers thicknesses), and can vary by several orders of magnitude, typically from 10^{-14} s to 10^{-9} s [147].

4.2.4 Limits of the model

Validity of the coherent tunneling

If the Esaki and Tsu formula, combined with transfer matrix transmission calculation, gives a simple prediction of the I-V curve, it appears that the experimental results are rarely in agreement with this theory. Indeed, the formula assumes a coherent transport in the region of the DB, which is, most of the time, not realistic. In fact, many scattering processes are involved in the electronic transport and modify the I-V characteristics: the peak to valley ratio (PVR) is thus reduced, the resonance peak enlarges or even disappears.

Here is a non-exhaustive list of scattering processes:

- ionized impurities scattering, which depends on the residual doping in the structure. The undoped spacers are sometimes included around the DB structure, in order to reduce the residual doping concentration.

- phonon scattering, which is proportional to the phonon population. It increases with the temperature. This is the main reason, with the broadening of Fermi functions, why resonant tunneling becomes weaker at higher temperatures. It is interesting to note that the electron-phonon interaction is stronger in piezoelectric materials.
- electron-electron scattering occurs at high electron density, *i.e.* at high current densities.
- crystal defects related scattering: point defects or extended defects like dislocations, stacking faults, etc.
- disorder related scattering, due to the alloy disorder (typically in the barriers), or the interface roughness.

In order to ensure the validity of the coherent transport, one should compare the scattering time of each scattering process with the tunneling time in the DB structure. If the tunneling time is shorter than the scattering time, the ballistic transport can be assumed. Theoretical studies have been carried about resonant and sequential tunneling. More details can be found in Refs. [148, 149].

Effects of space-charge buildup (self Consistent calculation methods):

In the previous paragraph, the potential has been approximated by linear segments with constant electric field, without taking into account the effect of the space-charge distribution in the structure. However, if this model can predict the existence of a NDR, it does not result in accurate quantitative prediction of the current-voltage characteristics of the structure. For a better accuracy, one has to consider the space charge layers that appear both in the neighbouring of the contact regions and in the QW populated with electrons. This effect would be even more critical for materials like GaN, which exhibits an internal polarization. In order to account for those effects, one has to solve, for the whole structure (including the contacts regions), the Poisson equation self-consistently with the Schrödinger equation for each given applied bias, analogously to the Schrödinger-Poisson method described in section (2.4.4). Refs. [150, 151] give more details about the self-consistent methods applied to the calculations of RTDs.

4.3 Challenges and review of resonant tunneling in GaN

4.3.1 Challenges for GaN-based RTDs

As mentioned earlier, GaN and related alloys are good candidates for the ISB optoelectronic devices, both in the near IR and THz regimes. Resonant tunneling is a key building block towards QCLs, since it enables very fast transport, which is necessary to achieve population inversion. Besides, III-nitrides have large band offsets, which should theoretically result in higher PVR. In addition, RTD-based oscillators can generate long wavelength electromagnetic signal at room temperature [152], and particularly in THz regime, as recently demonstrated by Suzuki *et al.* [153] in InGaAs/AlAs double barrier RTDs. Thus, GaN is a promising material for sources in the THz gap. Furthermore, GaN is known to support higher power than GaAs. For all those reasons, resonant tunneling in GaN has raised interest, and several groups have attempted to measure electron transport in GaN/(Al,Ga)N heterostructures, and particularly in DB RTDs.

However, in spite of all these promises, demonstrating an RTD based on GaN remains a challenging task for several reasons. First, there are some extrinsic reasons, due to the material quality. Indeed, GaN structures exhibit much higher dislocation densities, which can act as leakage channels. Those dislocations are inherent to the III-nitride structures, mainly because of the large lattice mismatches between the different alloys and the available substrates. Typical dislocation densities are $\sim 10^8 - 10^9 \text{ cm}^{-2}$ for layers grown on sapphire and 10^6 cm^{-2} for free standing GaN substrates. If the latter corresponds to an improvement of three orders of magnitude, it is still a high value compared to GaAs standard substrates ($\sim 10^2 \text{ cm}^{-2}$). Moreover, the large lattice mismatch between GaN and AlN and the low mobility of Al adatoms at the growing surface induce surface roughening during the growth, resulting in poor interfaces as already discussed in section (3.2.3). This interface roughness is the source of scattering, hindering as well the resonant tunneling. Besides, it is known that GaN and related compounds contain high point defects, which can act as deep traps and affect the tunneling process.

In addition, some of the intrinsic properties of III-nitrides are not beneficial to achieve RTDs. For instance, the effective masses are much higher than in GaAs based system ($\sim 0.2 m_0$ for GaN *vs.* $\sim 0.06 m_0$ for GaAs). Therefore, the tunneling probability across a barrier is smaller, and for this reason, (Al,Ga)N/GaN RTDs require thinner barriers than in GaAs. This is challenging from a growth point of view and it makes the device more sensitive to thickness fluctuations. In addition, the polar nature of III-nitride causes a 2D electron gas and a depletion region at each side of the double barrier structure. This has been theoretically studied in Ref. [154, 155]. The depletion region increases the barrier effective thickness. This point is also challenging in terms of structure design and band engineering. Finally, as it will be discussed at the end of this chapter, the polarization fields enhance the sensitivity of the structure to alloy broadening

Chapter 4. Unipolar vertical transport in (Al,Ga)N/GaN heterostructures

and interface roughness.

Another difficulty stands in the processing. A review about GaN processing can be found in Ref. [156]. III-nitride semiconductors are hard materials and have generally to be dry-etched when exhibiting the Ga polarity. If the technology is well mastered for quite large devices like LEDs or LDs, there are some shortcomings for small devices, which are aimed at limiting the number of dislocations. This point will be discussed later in this chapter.

4.3.2 Litterature review

Since the demonstration of a RTD is a crucial milestone for the development of III-nitride based unipolar optoelectronic devices, this issue has been of growing interest over the past decade, both theoretically and experimentally. Concerning early theoretical studies, Sacconi *et al.* in 2001 [157] predicted high PVR and room temperature operating RTDs thanks to the large CBO. Indlekofer *et al.* performed I-V simulations and predicted asymmetry in I-V curves, due to polarization effects [158].

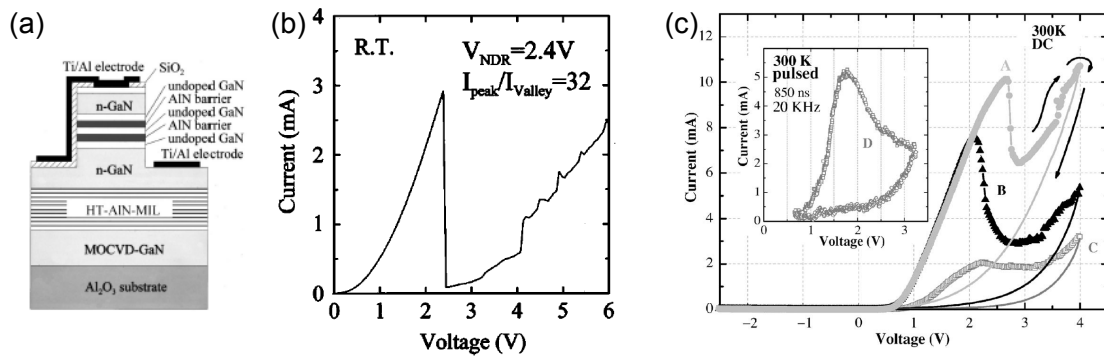


Figure 4.4 – Current-voltage measurements of GaN-based RTDs at room temperature. (a) GaN/AlN double barrier structure on sapphire (reproduced from Ref. [159]). (b) GaN/Al_{0.3}Ga_{0.7}N structure on bulk GaN substrate (reproduced from Ref. [160]).

The first result concerning DB RTDs is reported by the group of Kishino in Japan [159] in 2002. Their sample have been grown by PA-MBE on a sapphire substrate. The active region consists of two 1 nm thick AlN barriers sandwiching a 0.75 nm undoped GaN QW (see Fig. 4.4(a)). Two 2 nm thick undoped GaN spacers are surrounding the active region to avoid diffusion of donors, which might be a source of scattering. The current-voltage is measured at room temperature and a resonance peak is measured at 2.4 V, with a current density of 180 A/cm². The I-V curve is reproduced in Fig. 4.4(b). A PVR of 32 is measured.

However, the steepness of the resonance makes it looking more like current instabilities than resonant tunneling. It is specified in the article that this peak is not observed under negative bias, and the reproducibility such as the behaviour in backward sweep is not discussed. This result was subject to controversy, as attests the comment published from the group of

4.3. Challenges and review of resonant tunneling in GaN

Foxon [161] few months later. There, the authors indeed observe similar features, which are depending on the direction of the voltage sweep. This hysteresis indicates that the observed NDR cannot be clearly attributed to the resonance with a quantized state of the QW. In their response, Kikuchi *et al.* [162] allege that their NDR is related to resonant tunneling according to their simulations, and argue that the instability or hysteresis could be related to the dislocations or deep level defects in the AlN barriers, behaving like traps for electrons. Further on, Foxon *et al.* report the same discrepancies in I-V curves of GaN-based RTDs [163, 164]. They observe hysteresis and instabilities (similar as Ref. [159]), which are more pronounced at low temperatures.

Few years later, Golka *et al.* [160] report a significant improvement of the NDR characteristics, on DB-RTDs grown by PA-MBE on high quality bulk GaN substrates (dislocation density $\sim 10^2 \text{ cm}^{-2}$). Additionally, they reduce the Al content of the barrier to 70 % and use smaller mesas ($6 \times 6 \mu\text{m}^2$) to get dislocation-free devices. The observed I-V curve is depicted in Fig. 4.4(c). If the PVR (~ 2) is more realistic and the resonance less steep, these devices still exhibit hysteresis and loss of the NDR after few scans. Furthermore, the NDR is observed only on ~ 20 % of the devices.

In parallel to these attempts, interesting studies about material quality and leakage processes have been performed. For instance, Hermann *et al.* [165] have studied the transport across the single (Al,Ga)N barriers. They have observed, for instance, that under negative bias (electrons are collected from the side of the depletion region), the increase of the Al content induces larger leakage currents, whereas under positive bias, the current decreases with the Al content as it is expected in a tunneling mechanism. Conductive AFM studies have also been performed on single AlN barrier samples, and have revealed that the number of leaky dislocations (attributed to pure screw dislocations) is around ten times smaller than the overall dislocation density [166]. They have demonstrated as well that the larger is the AlN barrier, the higher are the leakages due to the dislocations coming from the AlN barrier relaxation [167, 168].

More recently, the group of Razeghi in Chicago have reported different results on MOVPE grown RTDs [169, 170, 171, 172, 173]. In the first two articles, they present GaN/AlN RTDs on sapphire samples, exhibiting features similar to Ref. [159] (accidental NDR, forward sweep only, and first scan). In the last three ones, they demonstrate significant improvements by using lower Al content barriers (down to 20 %) and low dislocation density GaN free-standing substrates. They report also the recovery of NDR but only for few scans in polar based structures [171], whereas in non-polar no ageing has been observed. Nevertheless, all those structures exhibit hysteretic behaviour. Also, it is interesting to note that the current density increases when reducing the mesa size [172]. Even if these results still present some discrepancies, they demonstrate the feasibility of such structures using MOVPE and emphasize the importance of low dislocation structures.

Chapter 4. Unipolar vertical transport in (Al,Ga)N/GaN heterostructures

Boucherit *et al.* [174] have managed to get NDR in both forward and reverse bias (but at different voltages), after applying a long constant negative bias. However, this is observed only for small mesas (2 μm diameter) and the NDR exhibits an accidental behaviour. It should be noticed that the measurement method is unusual, since the mesa is not metalized on top, but only contacted with a nanotip. This supports the influence of traps, since the negative bias is used to empty the traps. Li *et al.* have also observed similar behaviour [175, 176].

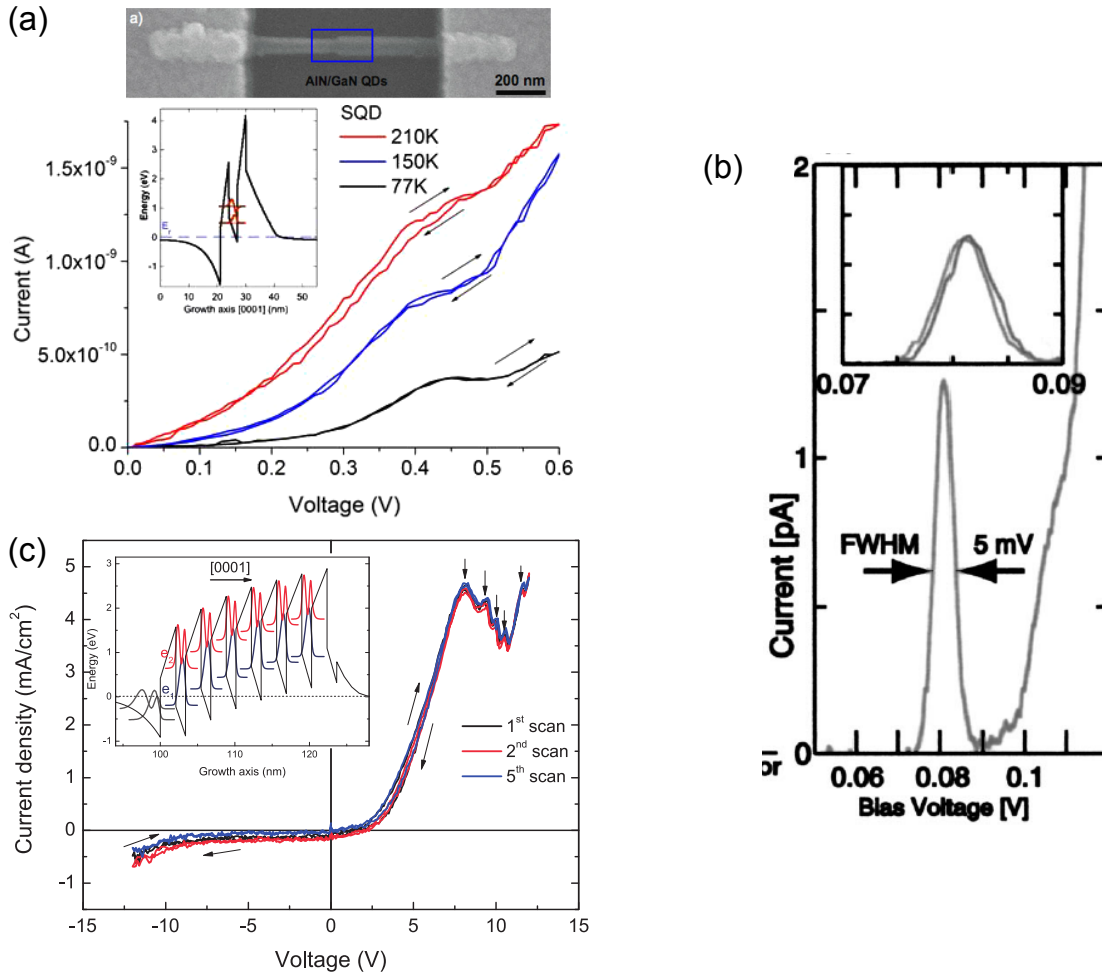


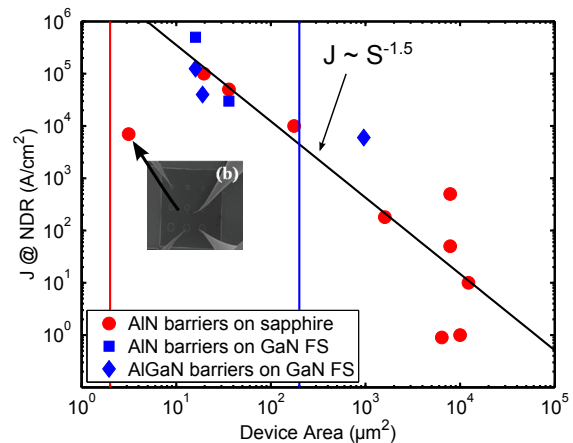
Figure 4.5 – Recent advancements on tunneling on GaN/AlN structures. (a) On a double barrier structure in a nanowire (depicted from Ref. [177]); the top image is a TEM picture of the nanowire. (b) InP-base nanowire RTD (reproduced from Ref. [178]). (c) resonant tunneling on a MQW structure (reproduced from Ref. [179]). The inset shows the conduction band profile calculated at zero bias.

Recent works have reported transport studies in quantum disks in single nanowires [180, 181, 177]. The I-V curve of a double barrier structure is depicted on Fig. 4.5(a). If the NDR can look unsatisfactory in terms of PVR, it should be noticed that this result represents a significant qualitative improvement compared to all previously reported RTDs. This improvement is

4.3. Challenges and review of resonant tunneling in GaN

ascribed to nanowires as they offer multiple advantages compared to 2D layers: they are dislocation-free and the probed area is very small, which makes them less sensitive to disorder or surface roughness. These superior figures of merit have been demonstrated in the InP/InAs system where PVR is as high as 50, and linewidth of the resonance peak is around 5 meV [178]. The I-V characteristics of those structures at low temperature are reproduced on Fig. 4.5(b). Transport measurements have been as well reported in MQW structures [182, 183, 179]. The results of the latest is presented on Fig. 4.5(c). Five reproducible NDR are observed at room temperature, both at forward and backward scans. Those NDR are attributed to the alignment of the quantized level of two subsequent QWs. However, the transport mechanism is quite different from the DB-RTD, since it is dominated by scattering assisted sequential tunneling. In addition, the MQW structure is more resistive, inducing lower current densities, as reported for DB structures. There are as well studies of RTDs on cubic GaN [184, 185]. However, these structures present the same problems as their polar counterparts, and have surprisingly asymmetric I-V curves.

Figure 4.6 – Plot of the current density at resonance versus the mesa area for all reported RTDs based on GaN. The inset correspond to a different processing without contact deposition (from Ref. [174]). Two vertical lines represent the mesa size corresponding to an expected value of one dislocation per mesa depending on the substrate: blue for GaN FS and red for sapphire.



To conclude this review, there is no obvious demonstration so far of resonant tunneling in planar DB-RTDs. If different I-V features are reported, they almost all suffer from the same issues: lack of reproducibility, hysteresis (NDR only at forward scan), fast degradation and, in some cases, an anomalously high NDR and PVR. It seems to be now accepted that electron trapping (from defects for instance) plays a role in those discrepancies. For instance, Sakr *et al.* have demonstrated that a reproducible NDR is not necessarily a proof of resonant tunneling [186]. They indeed observe a loss of the NDR when decreasing the temperature, which is contrary to the predictions of a quantum effect, as in RTDs made of other III-V materials. However, the origin of those traps is mostly subject to speculations, and no quantitative analysis of their effects has been discussed. Fig. 4.6 reports the current at the resonance *vs.* the mesa area of most of previously reported results. If the measured current density can vary by five orders of magnitude, it scales with the mesa area according to a power law, whatever

the substrate (sapphire or GaN FS) and the structure (Al content, barrier and QW thicknesses). One should expect constant current densities with the devices size.

4.4 First generation of RTDs: GaN/AlN structures

The first series of RTDs has been grown grown by MOVPE Aixtron 200/4 RF-S on GaN FS substrate (dislocation density of $\sim 10^6 \text{ cm}^{-2}$). The structure consists of a 2 nm GaN QW surrounded by two 1 nm AlN barriers at each side (Fig. 4.7(a)). The collector and injector are made of thick GaN layer doped with Si at $5 \times 10^{18} \text{ cm}^{-3}$. Indium is used as a surfactant, as described in Ref. [115]. The growth temperature is set to 935°C and indium (provided by TMIIn) is switched on only during the barrier growth. Such high temperature prevents indium incorporation, which has only a surfactant effect. The Al/In flux ratio is around 0.6 and results in an In content lower than 2 %, confirmed by XRD measurements. This results in lower interface roughness, attested by AFM measurements, and therefore a reduction of the PL linewidth by 45 %.

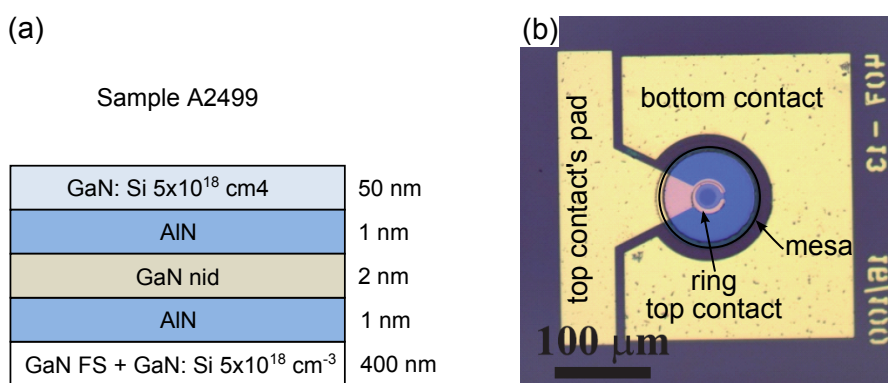


Figure 4.7 – (a) sketch of the grown structure and (b) top view image of a processed device, having a 100 μm diameter mesa.

The sample was then processed using standard UV-lithography techniques (more details are given in the appendix), with a set of masks designed for VCSEL, and having round mesa sizes from 20 to 200 μm diameter. The process starts with the dry-etching of the mesas by ICP with a chlorine mixture, followed by PECVD deposition of SiO_2 . The second mask is used for opening the SiO_2 on top of the mesas and for the bottom contact, which is dry-etched by RIE using CHF_3 . The last step of the process corresponds to the contact deposition. The set of masks enables the deposition of top (together with the metallic pads) and bottom contacts at the same time. The contacts are deposited by e-beam evaporation and consist of Ti/Al/Ti/Au (10/50/10/100 nm). Those are standard n-type ohmic contacts used for LEDs and LDs. Fig. 4.7(b) is a picture of the processed device. As can be seen, the top contact is a ring: this is because the masks were originally designed for VCSEL devices.

4.4. First generation of RTDs: GaN/AlN structures

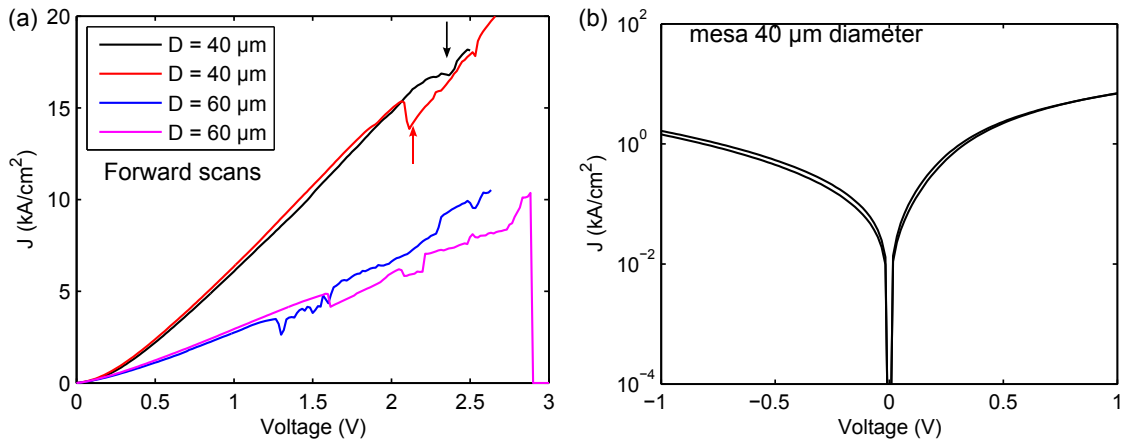


Figure 4.8 – (a) current voltage characteristics at room temperature on four different mesas. (b) close-up in log scale around zero bias for a 5 μm diameter mesa.

The I-V characteristics were then measured at room temperature using a Keithley 4200 parameter analyser and a probe station. The bias is applied on the top mesa, which means that a positive bias corresponds to electrons emitted from the substrate side and collected at the top side. All the I-V characteristics presented in this chapter are done this way. Fig. 4.8 presents some of the measurements carried out on two different diameter devices (40 μm and 60 μm). Both are done at forward voltages and exhibit "NDR-like" behaviour, pointed by the vertical black and red arrows. These features are observed for the first scan only, which is similar to previous results reported in the literature on similar samples [169], and are not recovered after applying a negative bias. Such features are not observed under negative bias. Interestingly, those features do not appear for mesas bigger than 40 μm diameter. As the figure shows, in the two curves for 60 μm diameter mesas only current instabilities are observed. However, those instabilities also disappear after the first scan. The curve in magenta exhibits a sudden decrease of the current, which corresponds to the breakdown of the device. Fig. 4.8(b) shows the I-V curve for a 40 μm diameter mesa in log scale around zero bias. In this range, there is no obvious hysteresis between forward and backward sweeps. The curve is much less asymmetric to what has been reported in the literature.

In order to assess the material quality of the sample, XRD measurements have been performed. Fig. 4.9(a) shows the $2\theta - \Omega$ scan of the [0002] reflection. As can be seen, the simulation of the nominal structure does not match with the data. The experimental XRD curve could be well fitted taking the Al content in the barriers, the barrier thicknesses, and the QW thickness as adjustable parameters (red curve in Fig. 4.9(b)). The best fit corresponds to AlGaN barriers (instead of AlN), which are thicker by a factor of two compared to nominal values. This profile can be qualitatively explained by alloy mixing and/or segregation (blue profile). One should be cautious that interface mixing profile is not the only possible explanation for these

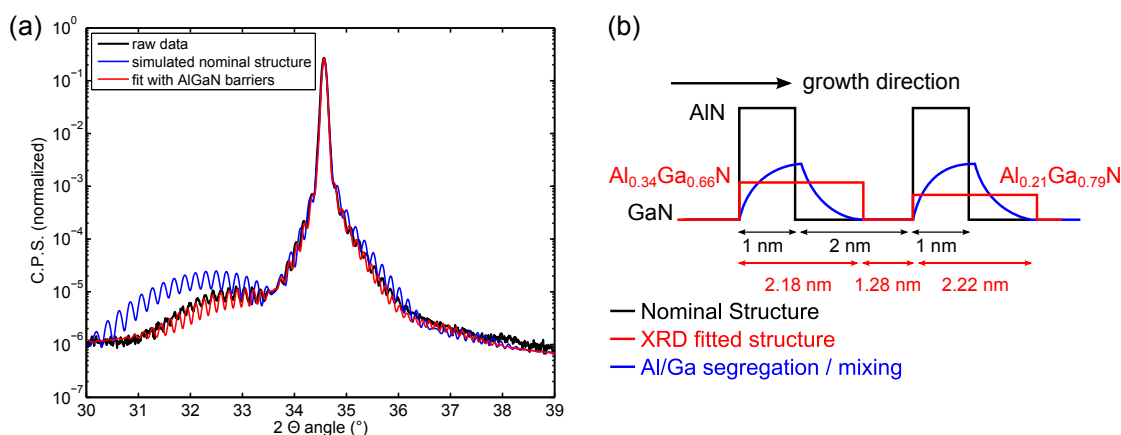


Figure 4.9 – (a) XRD analysis of the double barrier AlN/GaN structure showing the raw data (black) the simulation of the nominal structure (blue) and the best fit obtained assuming AlGaN barriers. (b) Sketch of the nominal and simulated structure.

discrepancies in the XRD data. For instance, interface roughness could be also considered. In any case, this confirms the difficulties to grow this kind of structures with MOVPE. However, even if the structure is different from the nominal one, it seems to be homogeneous, as attests the well resolved oscillations in the XRD spectrum. Therefore, a poor structural quality can not explain the observed features in the I-V characteristics. Moreover, we have grown numerous DB-RTD samples by NH_3 -MBE on both sapphire and GaN substrates (polar and non-polar), and similar I-V characteristics were obtained.

4.5 Second generation of RTDs: presentation of the approach

Following those unsuccessful attempts, the decision has been made to tackle the issue of resonant tunneling by testing different designs, using state of the art MOVPE growth recipes, and establishing a dedicated process.

4.5.1 Materials and growth

The first decision was to use barriers with low aluminium content, between 10 and 15%. This is contrary to most of all reported RTDs, where $\text{Al}_x\text{Ga}_{1-x}\text{N}$ ($x > 30\%$) or AlN barriers are used. The lowest reported Al barrier content is 20% [171, 176]. Working with low Al content barriers provides several advantages:

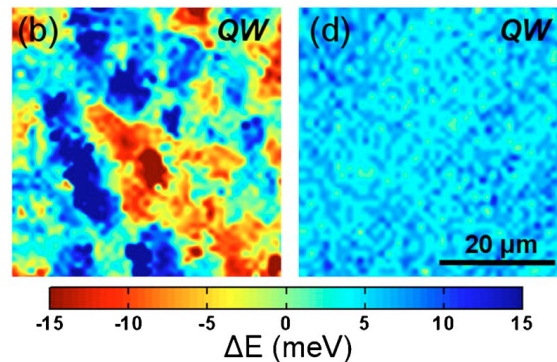
- It reduces considerably the lattice mismatch between the GaN and the barriers. Therefore, it should reduce the defect density, such as strain induced dislocations. Besides, it suppresses the interfaces instabilities that exist in AlN barriers while strained on GaN [114, 110], and should thus result in sharper interfaces.

4.5. Second generation of RTDs: presentation of the approach

- It has been shown that above a certain Al content, AlGa_xN suffers from deep level defects. For instance, Mattila *et al.* [187] theoretically predict that oxygen contamination will form DX-like centers for Al content higher than 30 %. This has been experimentally confirmed by McCluskey *et al.* [188] by Hall effect measurements. Therefore, low Al content is expected to reduce the effects of traps in the barriers, which is usually alleged to hinder the NDR and to cause hysteresis in I-V curves.
- It reduces the CBO, and thus favors tunneling probability. In addition, it allows growing thicker barriers, which in turn should be less sensitive to thickness fluctuations.
- It also results in a lower polarization mismatch, thus a lower electric field in the barriers and QWs, which will alleviate the detrimental consequences of the internal electric field.
- Moreover, lower Al content results in lower alloy disorder, as it has been experimentally demonstrated [5, 125].
- Finally, as discussed in the previous chapter, low Al content is well adapted for THz ISB applications. Therefore, the demonstration of resonant tunneling in such RTDs would be a step forward to the realization of GaN-based THz QCLs.

The principal drawback of using low Al content is the reduction of the CBO. If it increases the tunneling probability, it theoretically impacts the device performance in terms of NDR and PVR. This may also degrade the performance at room temperature. However, excellent GaAs/AlGaAs-based RTDs have been demonstrated with comparable band offsets exhibiting NDR features up to 200 K [189].

Figure 4.10 – Maximum peak energy mapping of a GaN/Al_{0.1}Ga_{0.9}N single QW measured by μ PL for the high (left) and low (right) temperature grown AlGa_xN barriers. The samples are grown on sapphire substrates. Measurements are done at 5 K. Reproduced from Ref. [5].



The structures were grown by MOVPE, in the Aixtron CCS 3 × 2" reactor. An advantage of MOVPE over MBE is the higher growth temperature, closer to equilibrium. This reduces the incorporation of point defects, which may behave as electron traps, inducing pernicious effects in RTDs. A couple of years ago, our laboratory could demonstrate high quality GaN QWs in Al_xGa_{1-x}N ($x \sim 10 - 15\%$) on sapphire substrates [5]. In this reference, it is shown

that adapted growth conditions, *i.e.* reduce growth rate and growth temperature from 1040° C to 930° C, enhancing drastically the alloy homogeneity. Fig. 4.10 shows the mapping of QW emission energy measured by μ PL at 5 K on samples grown at high (left) and low (right) temperatures. The lower dispersion of the QW energy in the low temperature grown sample gives a narrower PL peak with a FWHM of 11 meV for 9 % Al content, which is slightly better than the values measured on NH_3 -MBE grown samples [125]. Those high quality structures enabled the observation of bi-excitons [190] and spin relaxation [191]. On the other hand, those improved growth conditions increase the roughness by a factor of ~ 2 . This indicates that the inhomogeneous broadening is dominated by alloy disorder rather than by interface roughness, which is opposite to the observations made on GaAs/AlGaAs MQWs [192].

The growth recipe described in Ref. [5], developed in the horizontal MOVPE reactor, was adapted to the vertical showerhead reactor. The growth temperature for the active region of the RTDs is set to 950° C and the AlGa_N growth rate is around 50 nm/h. It has been shown that the reduction of alloy scattering in GaN/AlGa_N HEMT structures leads to higher electron mobility [193]. Similarly, one can expect that better alloy homogeneity in RTD structures should favor coherent tunneling and thus improve the characteristics of the device.

Furthermore, we decided not to grow any non intentionally doped spacer around the active region in contrary to most GaN-based RTD structures reported in the literature. Moreover, to decrease the contact resistance, a 5 nm GaN cap, highly doped at $2 \times 10^{19} \text{ cm}^{-3}$, was grown on top of the samples.

Concerning the substrate, we favored free-standing GaN. Indeed, the dislocation density is reduced by three orders of magnitudes compared to GaN grown on sapphire ($\sim 10^6 \text{ cm}^{-2}$ *vs.* $\sim 10^9 \text{ cm}^{-2}$), which should minimize the current leakages supported by screw dislocations [166]. Besides, those substrates are heavily doped, and offer the advantage of depositing the bottom contact on the backside of the substrate.

4.5.2 Processing

It is widely acknowledged that the dislocations have deleterious effects on GaN-based RTDs, as they are source of scattering and leaky parasitic channels. Therefore, an ideal device should have no dislocations. This is possible by using high quality substrates and very small device sizes. For instance, if one considers a dislocation density of $5 \times 10^6 \text{ cm}^{-2}$, which corresponds to FS GaN substrates, a mesa size of $4 \mu\text{m}^2$ (that is the smallest size used in this work), gives an expected value of 0.2 dislocation per mesa. The probability to get a device free of dislocations is 82 %, according to the Poisson distribution. This probability decreases rapidly when the mesa size increases: 28 % for $25 \mu\text{m}^2$ and 0.6 % for $100 \mu\text{m}^2$. However, devices of such small sizes are highly critical when using a standard LED-like process (3 levels), which was used for the first generation RTDs (Sec. 4.4), since it requires very precise alignment for the SiO_2

4.5. Second generation of RTDs: presentation of the approach

aperture on top of the mesa (2nd level). Unfortunately, the mask aligner at our disposal could hardly enable sub- μm precision.

In order to achieve the small size device, a self-aligned process was developed. This kind of process is already well mastered in our laboratory and is used to etch and contact the ridges of LDs, which can have width as small as $2\ \mu\text{m}$. A new set of three masks has then been designed specifically for RTDs. The details of the process flow are given in the appendix. The main steps are the following: a lithography is first done with a negative photoresist, followed by ICP dry-etching of GaN to pattern the mesas. Then the SiO_2 passivation layer is deposited by sputtering, with physical vapour deposition technique (PVD), while the resist still covers the top of the mesa. Thanks to the properties of negative photoresist, inducing an under-etched profile (see the appendix), and the directionality of the SiO_2 layer ensured by the PVD deposition, it is possible to lift-off the resist and the covering oxide. The device is thus passivated everywhere except on top of the mesa. The last lithographic level is for the contacts. The top and bottom (frontside) contacts (Ti/Al/Ti/Au ($10/50/10/150\ \text{nm}$)) are deposited together via e-beam evaporation. The final device is sketched on Fig. 4.11(a). The right figure is an optical microscope image of a device with a $10 \times 10\ \mu\text{m}^2$ mesa.

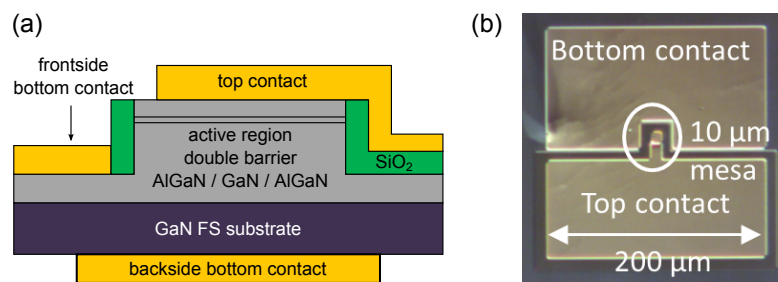


Figure 4.11 – (a) sketch of a RTD device fabricated following the self-aligned process. (b) Optical microscopy image of a $10 \times 10\ \mu\text{m}^2$ mesa device.

For the masks, square mesas of the following sizes were used: 2×2 , 5×5 , 10×10 , 20×20 , and $40 \times 40\ \mu\text{m}^2$. The two first sizes should provide a high probability to get devices free of dislocations (81 and 28 %). Therefore, the mesa size, together with the low dislocation density substrate, should enable to study the impact of dislocations on resonant tunneling.

The masks are designed to perform transmission line measurements (TLM) on both top and frontside bottom contacts to assess their quality. No Schottky behaviour is observed in those contacts and annealing was not necessary. One should notice that contact annealing is not compatible with the process. This is because it requires temperatures around 800°C , where adherence between the SiO_2 passivation layer and the metal is lost, resulting in short-circuit. Annealing at lower temperatures ($300\text{-}400^\circ\text{C}$) did not bring any improvements. Nevertheless, thanks to the highly doped GaN cap, contact resistances are between 10^{-4} and $10^{-5}\ \Omega\cdot\text{cm}^2$.

4.5.3 Design and simulations

Before growing and processing the samples, simulations of different structures fulfilling the specifications described above (Al content lower than 15 %) have been performed, and different structures have been tested to tune the band profile symmetry and the electric field in the QW. Depending on the band profile, one should expect different behaviours in the I-V curves. For instance, the NDR resonance voltage should depend on the quantized energy level in the QW. For a symmetrized band profile, a symmetric I-V curve is expected.

For the first series, simulations of symmetric structures were performed with Nextnano, varying the QW thickness from 1 to 4.5 nm, the barrier width from 1 to 2 nm, and for Al content of 10 % and 15 %. Finally four designs were selected: their structures are given in the first part of table 4.1 (N1 to N4 samples). They correspond to QW thicknesses of 3.5 and 4.5 nm. Other simulated structures were not retained because the bound states of the QW were not well confined. For thick QWs the internal field helps to confine the bound state, by increasing the barrier effective height (proportional to $t_w/(t_w + t_b)$). The conduction band profiles of the selected structures are shown on Fig. 4.12.

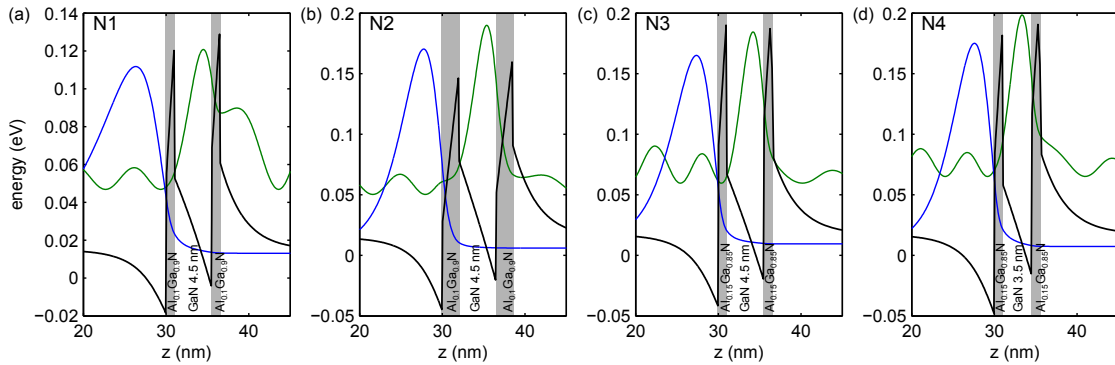


Figure 4.12 – Simulated band profile of the four symmetric structures (N1, N2, N3, and N4 of table 4.1).

As can be seen, the quantized state are slightly leaky, especially for N1. This is not an ideal case to get narrow transmission linewidth, *i.e.* large PVR, as discussed in Ref. [155]. However, it indicates that tunneling is possible, and one can expect that the improvement of the material quality, using low Al content barriers, will compensate this shortcomings. For the N series different energies are calculated, and therefore, it is expected to observe a correlation with the resonance voltage of the RTDs. This is because the required electric field to align the two levels and to observe the resonance should be roughly proportional to this energy, as long as the structures are not too different (in terms of barriers height or active region thickness). The calculated band diagram of N1 under a voltage corresponding to resonance is shown on Fig. 4.14(c).

The samples of second series (denoted A1 to A4 in Tab. 4.1) are asymmetric structures. As

4.5. Second generation of RTDs: presentation of the approach

Table 4.1 – list of the grown samples. Except for MQWs, all claddings are nominally doped at $5 \times 10^{18} \text{ cm}^{-3}$. t_{barrier} corresponds to the barrier thickness, and x_{Al} to the Al content in the barrier. For asymmetric structures, if two values are given, the first (resp. second) one refers to the lower (resp. upper) parameter in the growth direction. Energy is the difference between the first quantized state of the QW compared to the 2DEG energy level or the bandedge energy in the injector at zero bias.

sample ID		structure				Energy
ref.	growth Nb.	cladding	t_{barrier}	x_{Al}	QW	
symmetric double barrier structures						
N1	C1377 + C1529	GaN	1 nm	10 %	GaN 4.5 nm	34 meV
N2	C1402	GaN	2 nm	10 %	GaN 4.5 nm	44 meV
N3	C1403	GaN	1 nm	15 %	GaN 4.5 nm	51 meV
N4	C1404	GaN	1 nm	15 %	GaN 3.5 nm	58 meV
asymmetric double barrier structures						
A1	C1530	$\text{Al}_{0.04}\text{Ga}_{0.96}\text{N}$	2/2 nm	10/15 %	GaN 4.5 nm	-1 meV
A2	C1531	$\text{Al}_{0.04}\text{Ga}_{0.96}\text{N}$	2/1 nm	10/15 %	GaN 4.5 nm	12 meV
A3	C1532	$\text{Al}_{0.04}\text{Ga}_{0.96}\text{N}$ / GaN (top)	1/1 nm	15/15 %	GaN 4.5 nm	80 meV
step QW structures (W0 is the reference)						
W0	C1534	$\text{Al}_{0.05}\text{Ga}_{0.95}\text{N}$	1 nm	15 %	GaN 4.5 nm	12 meV
W1	C1533	$\text{Al}_{0.05}\text{Ga}_{0.95}\text{N}$	1 nm	15 %	GaN 1 nm + $\text{Al}_{0.07}\text{Ga}_{0.93}\text{N}$ 3.5 nm	35 meV
MQWs structures for calibrations (20 periods, grown on GaN-FS)						
M1	C1513	GaN nid	2 nm	10 %	GaN 4 nm	–
M2	C1515	GaN nid	1 nm	10 %	GaN 4 nm	–
M3	C1516	GaN nid	0.5 nm	10 %	GaN 4 nm	–

opposite to the N series, the simulations were performed without any restriction on the symmetry: different geometry were tested, varying independently the parameters of the two barriers (Al content and thickness). $\text{Al}_{0.04}\text{Ga}_{0.96}\text{N}$ injector / collector (instead of GaN) were also considered. The reason for the development of asymmetric structures are twofold. First, it suppresses the 2DEG at the interface between the injector and the active region. Secondly, it can be used to reduce the depletion layers subsequent to the DB structure which can considerably increase the barrier thickness, hindering resonant tunneling. Such structures have been theoretically proposed [154, 155] for AlN/GaN DB-RTDs. Moreover, the band profile is somehow symmetrized, which should enable the observation of NDR at both positive and negative biases [155]. This has never been observed for GaN-based RTDs. The conduction band diagrams for the three selected structures are shown on Fig. 4.13. The A1 and A2 samples use $\text{Al}_{0.04}\text{Ga}_{0.96}\text{N}$ for both the injector and collector. The asymmetry comes from the barrier that has different Al contents (A1 and A2) and different barrier thicknesses (A2). The thinner and lower Al content barrier is necessary on the top side to diminish the impact of the

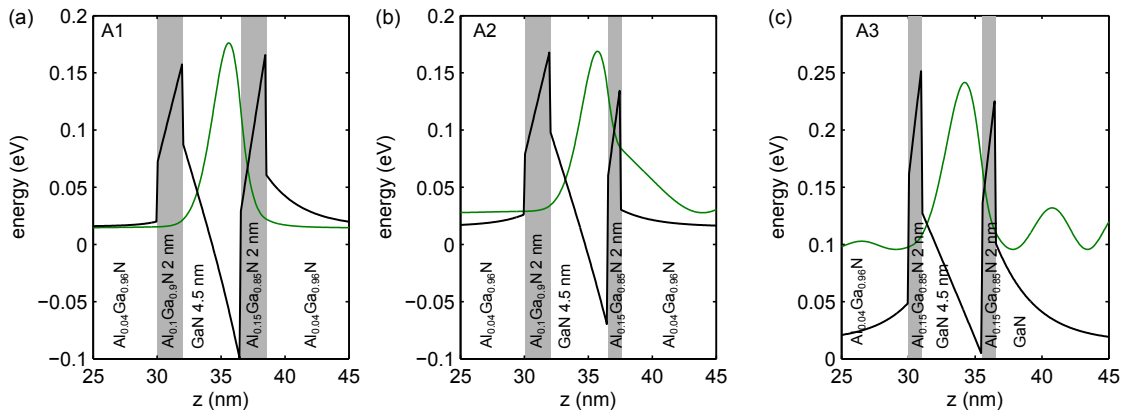


Figure 4.13 – Simulated band profile of the three asymmetric structures (A1, A2 and A3 of table 4.1).

depletion region. As seen on both diagrams, there is no 2DEG nor depletion region on the two structures. The third sample (A3) has symmetric barriers, but the cladding layers are different: $\text{Al}_{0.04}\text{Ga}_{0.96}\text{N}$ for the injector and GaN for the collector. It results in an almost symmetric band profile, without 2DEG. Fig. 4.14(f) presents the band profile close to the expected resonance. Interestingly, the energy levels of the bound states are both almost resonant at zero bias, while the third one exhibits a bound state energy of 80 meV. Therefore, one should not expect any resonance in the I-V curves, as there are no bound states of higher energies, whereas a NDR is expected for the third sample. If measurements are in agreement with those predictions, they provide good arguments in favor of resonant tunneling through the DBs.

The last two RTDs, denoted W0 and W1 in Tab. 4.1, have been grown to study the impact of the electric field in the QW on the current-voltage characteristics. They feature a step QW, composed of 1 nm GaN and 3.5 nm $\text{Al}_{0.07}\text{Ga}_{0.93}\text{N}$, which is close to the average Al content of the active region and results in a quasi-annihilation of the electric field. Similar structures have been studied to observe THz ISB absorption in GaN QWs [4]. Indeed, the flatband structure overcomes the issues of confinement by the triangular potential, and thus enables long wavelength ISB absorption. The two cladding layers are made of Si doped $\text{Al}_{0.05}\text{Ga}_{0.95}\text{N}$ layers. As for the other grown samples, a GaN cap is deposited on top of the structure to achieve low resistance contacts. Fig. 4.14(h) shows the band profile at zero bias, exhibiting almost zero internal field in the step QW. Fig. 4.14(i), corresponds to an applied field of 45 kV/cm, which is close to the resonance according to the simulations. Furthermore, the flatband conditions may result in a lower sensitivity of the sample with respect to alloy and interface disorder. This point is theoretically discussed at the end of the chapter. The first purpose of this sample is to demonstrate the feasibility of resonant tunneling on step QW, which has potential to enable devices working in the THz regime. The second aim is to study the impact of the electric field on the resonant tunneling. To this aim, a reference sample has been grown (W0), having a

4.5. Second generation of RTDs: presentation of the approach

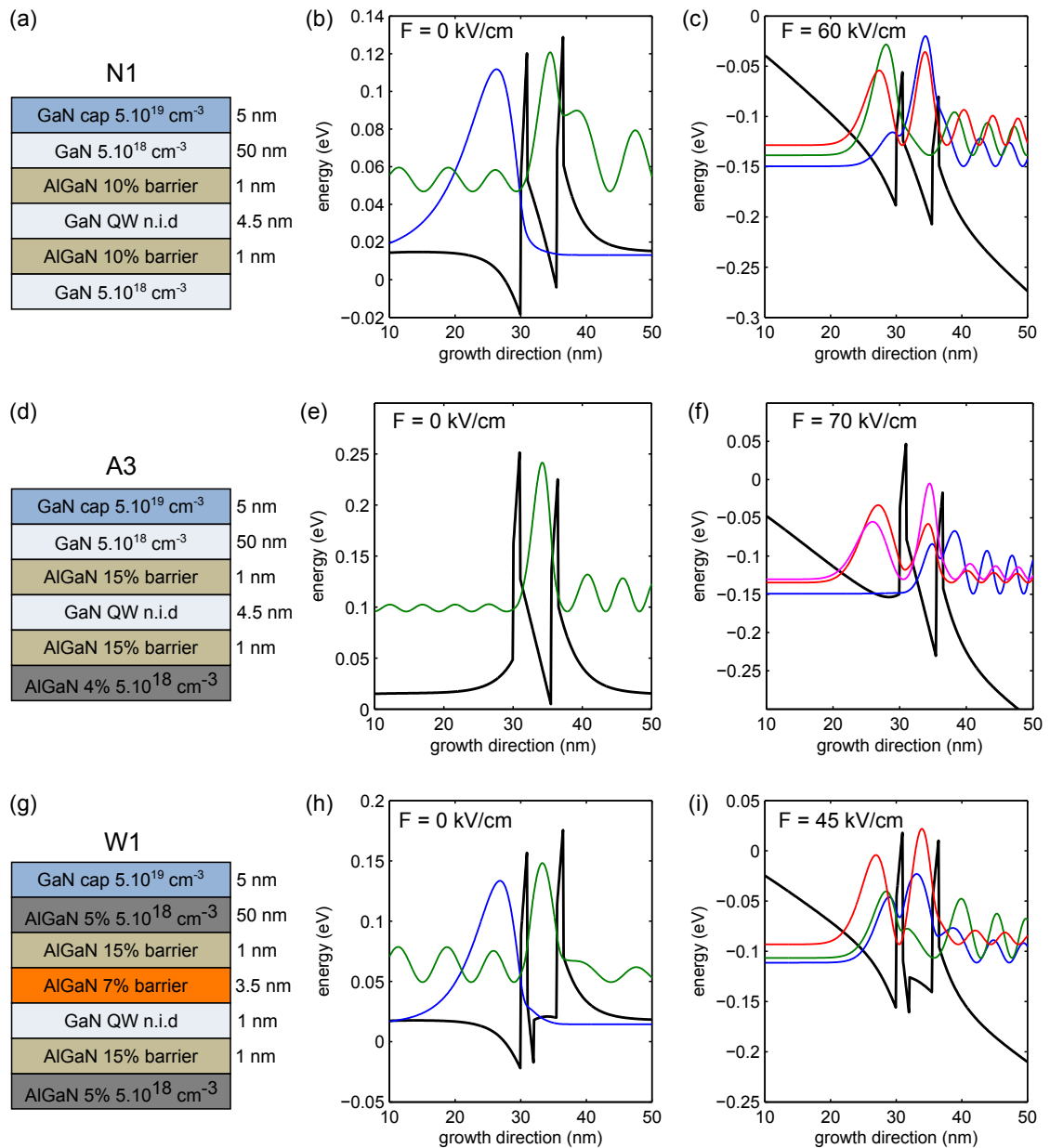


Figure 4.14 – (a-c) design and band structure calculation at zero and close to resonance bias of the reference $\text{Al}_{0.1}\text{Ga}_{0.9}\text{N}$ double barrier structure. (d-f) idem but for a polarization balanced barrier using $\text{Al}_{0.04}\text{Ga}_{0.096}\text{N}$ injector, and (g-i) for the step QW structure.

4.5 nm GaN QW.

4.6 Growth quality assessment

4.6.1 X-ray diffraction and HR-TEM on MQWs structures

In order to evaluate the MOVPE growth control and the material quality, MQW calibration samples were grown on GaN FS substrates. The list is given in Tab. 4.1: they are denoted by M1, M2 and M3. A standard 2.5 μm non intentionally doped GaN buffer layer is deposited first on the substrate. Then MQWs are grown using the RTD conditions described previously. Nominally, each layer consists of 20 QWs of 4 nm thickness, separated with $\text{Al}_{0.1}\text{Ga}_{0.9}\text{N}$ barriers of different thicknesses: 2, 1 and 0.5 nm. The samples are not capped and finish with the last barrier.

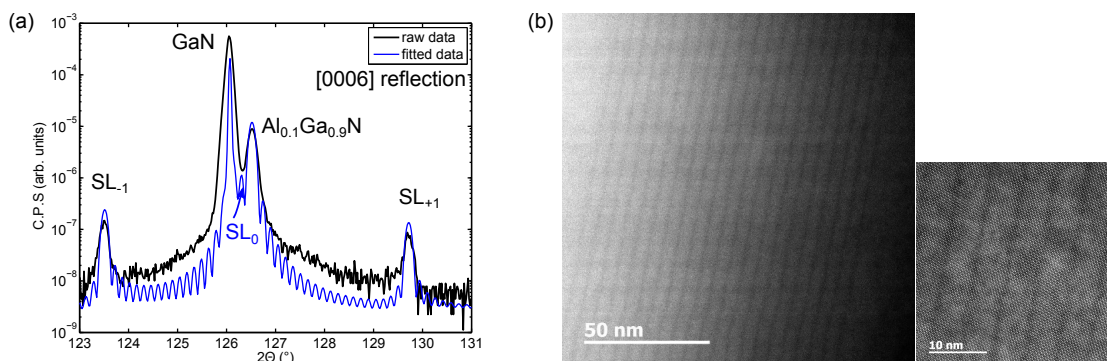


Figure 4.15 – (a) $2\theta/\Omega$ XRD data and fit of M1 sample around the [0006] reflection. (b) High resolution TEM image of M2 sample (courtesy of Dr. P. Ruterana).

The first reason to grow MQW structures was to measure the SL period by XRD. The Bruker analysis software also enables to fit the two thicknesses independently and the Al content in the barriers. Fig. 4.15(a) is the $2\theta - \Omega$ XRD pattern of M1 sample for the [0006] symmetric reflection. The high order of the reflection enables to separate the GaN and the low AlGaN peaks. The two well resolved peaks, with almost the same intensity as the fitted curve, confirm the excellent periodicity of the structure.

Table 4.2 – Results of the XRD fitting of the three grown calibration samples.

sample	Al content		QW thickness		barrier thickness	
	nominal	fit	nominal	fit	nominal	fit
M1	10 %	11.5 %	4 nm	4.20 nm	2 nm	2.15 nm
M2	10 %	11.5 %	4 nm	4.18 nm	1 nm	1.05 nm
M3	10 %	-	4 nm	-	0.5 nm	-

The results of the fits are given in Tab. 4.2. For the three samples, XRD fitting gives an Al content of 11.5 %, slightly higher than the targeted value. Concerning the fitted thicknesses of M1 and M2, they are slightly higher than the nominal ones, within a deviation of $\sim 5\%$. Concerning the M3 sample, with a barrier of 0.5 nm, no SL signature could be resolved in the XRD pattern. This might be explained both by the low contrast between GaN and $\text{Al}_{0.1}\text{Ga}_{0.9}\text{N}$, and also by the interface roughness. Indeed, in Ref. [5], where similar growth conditions are used, it is shown that the AlGaN roughness is higher when using the low temperature growth conditions.

High resolution TEM measurements have also been performed on the M2 sample (Fig. 4.15(b)). Despite the poor contrast between the barrier and the QW, the structure exhibits a good periodicity and the measured thicknesses correspond to the XRD data.

4.6.2 Temperature dependent optical spectroscopy

In order to further assess the quality of the MQW structures and estimate the inhomogeneous broadening, temperature dependant PL measurements have been performed.

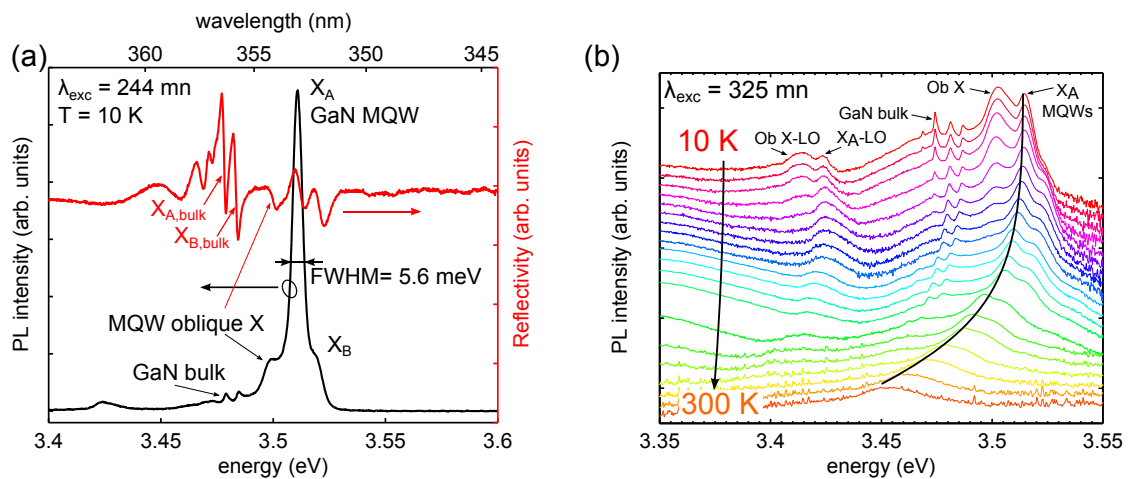


Figure 4.16 – (a) photoluminescence spectrum and reflectivity at low temperature of M1 sample ($t_b=2$ nm). (b) Temperature dependent photoluminescence spectra.

Fig. 4.16(a) presents the photoluminescence (black) and reflectivity (red) spectra taken at the same spot of the sample at 10 K. In the photoluminescence curve, an intense excitonic emission is observed at 3.511 eV, which corresponds to A free-exciton in the MQWs. This can be testified on the reflectivity spectrum, which exhibits two well-resolved features corresponding to A and B excitons. The FWHM of the peak is 5.6 meV, which confirms a very low inhomogeneous broadening. The small peaks around 3.48 eV correspond to D^0X , X_A , and X_B excitons of the bulk GaN buffer layer (they are also observed in the reflectivity spectrum). Another peak is observed at 3.499 eV (12 meV lower than the QW emission energy), between the bulk

emission and X_A of the MQW. At first, the origin of this peak was unclear. The reflectivity spectrum shows an excitonic resonance corresponding to this peak, meaning that it cannot be attributed to localized states nor bi-excitons. This peak is attributed to oblique excitons between two adjacent QWs. This transition is allowed, first because the low Al content barrier that enables tunneling. Secondly because the QCSE induces a spatial separation between electrons and holes. The QW (4 nm) is thicker than the barriers (2 nm), which favours this oblique transition. Such indirect excitonic transitions have already been observed by Gil *et al.* [194]. The energy difference could be due to a larger exciton binding energy. The energy of the oblique exciton emission peak is 8 meV, lower than for X_A of the QWs. This could be explained by a larger penetration length of the wave function in the barrier. On Fig. 4.16(b) is the evolution of the PL spectrum as a function of the temperature. The luminescence of the X_A exciton of the QW is resolved up to room temperature, where the FWHM is equal to 25 meV. The signature of the oblique exciton and its LO-phonon replica is resolved up to 100 K, likely due to the reduced oscillator strength.

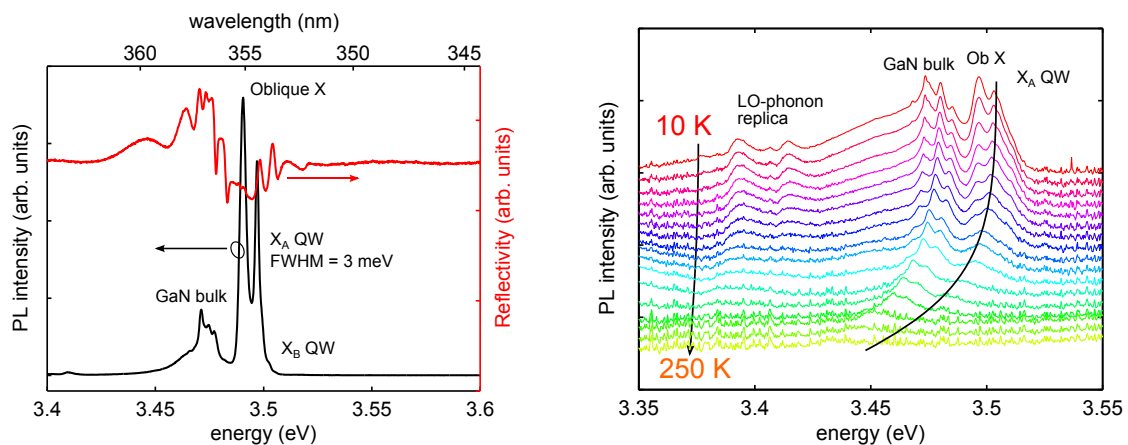


Figure 4.17 – (a) photoluminescence spectrum and reflectivity at low temperature of M3 sample ($t_b=0.5$ nm). (b) Temperature dependent photoluminescence spectra.

Fig. 4.17 shows the same measurements for the M3 sample, having barrier width of 0.5 nm. Interestingly, the SL signature could not be resolved on this sample, however it shows a very intense peak, attributed to the QWs at 3.497 eV and having a FWHM of 2.7 meV. Such a narrow linewidth can be originated from a miniband state, due to a delocalization of the electrons over the active region. On this sample, the peak attributed to oblique exciton is also observed at 3.490 eV with a FWHM of 3 meV. The peak is more intense than X_A , because the barriers are thinner, increasing therefore the oscillator strength of the transition.

Finally, the study on the MQWs (optical and structural) confirms the excellent quality of the layers and the growth excellent control. M3 sample does not exhibit SL satellite peaks in XRD, but exhibits extremely narrow PL linewidth. This indicates that even if interface roughness is

present in this sample, interfaces are homogeneous at the scale of the exciton Bohr radius.

4.6.3 Growth control on double barrier structures

Besides the characterization of the MQW structures, the material quality of RTD structures has been as well investigated. As an example, Fig. 4.18(a) shows the doping profile of a sample grown for doping calibration. This measurement is done by a electro-chemical capacitance-voltage profiler. The 5 nm GaN cap has a donor concentration of $1.5 \times 10^{19} \text{ cm}^{-3}$, close to the nominal value of $2 \times 10^{19} \text{ cm}^{-3}$. The cladding layers are doped at $2.7 \times 10^{18} \text{ cm}^{-3}$, slightly lower than the target ($5 \times 10^{18} \text{ cm}^{-3}$). The growth parameters have then been adjusted for the subsequent layers. Fig. 4.18(b) is a high resolution TEM image of the N3 sample.

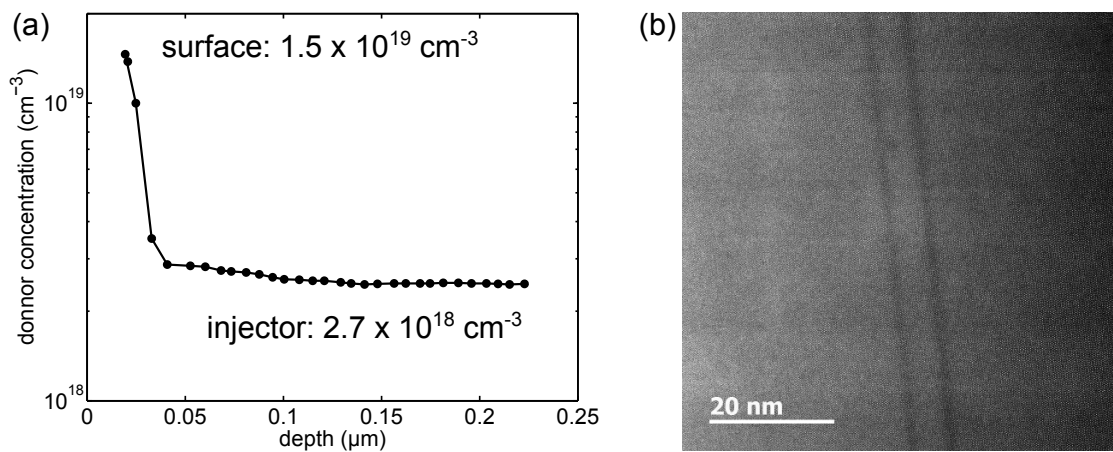


Figure 4.18 – (a) Donor concentration profile obtained by capacitance-voltage measurements. (b) High resolution TEM image of N3 sample: $\text{Al}_{0.15}\text{Ga}_{0.85}\text{N}/\text{GaN}/\text{Al}_{0.15}\text{Ga}_{0.85}\text{N}$ (1/3.5/1 nm). Courtesy of Dr. P. Ruterana.

4.7 Electrical characterization

All the RTD samples listed in Tab. 4.1 have been grown, and processed as described earlier. The I-V curves are measured with the probe station. All presented measurements are made with bias applied on the top contact: a positive voltage corresponds to electrons collected on the top side. A typical measurement is a forward and backward scan starting from 0 (or $-V$) to $+V$, where V is the maximum voltage (generally between 2 and 5 volt) depending on the sample and mesa size. The steps between each measurement are about 10 mV, and the time at each step is around 20 ms. It worth to notice that the scan speed does not seem to affect the results.

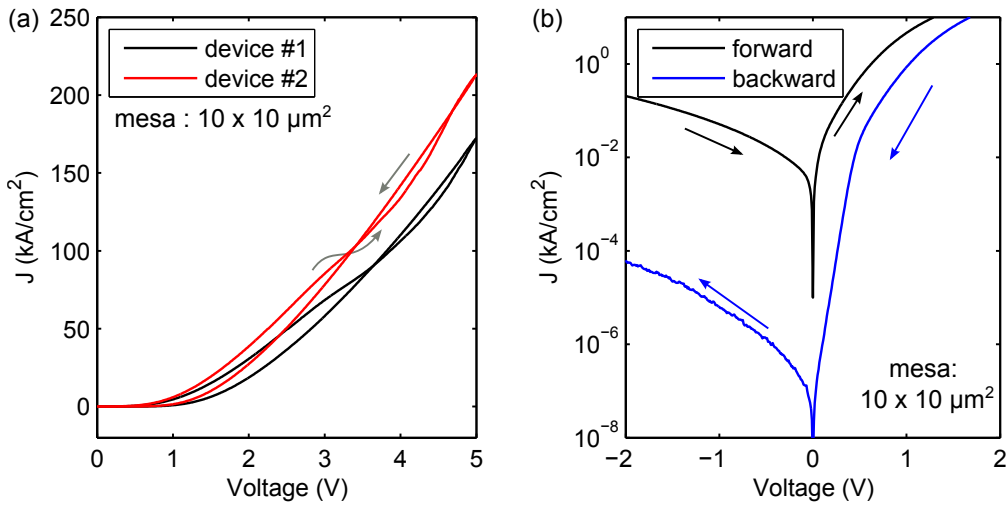


Figure 4.19 – (a) Current-voltage characteristics of N3 sample for two different devices. (b) close up logarithmic scale around 0 V for single forward and backward sweep measurement. The arrows indicate the direction of the scan.

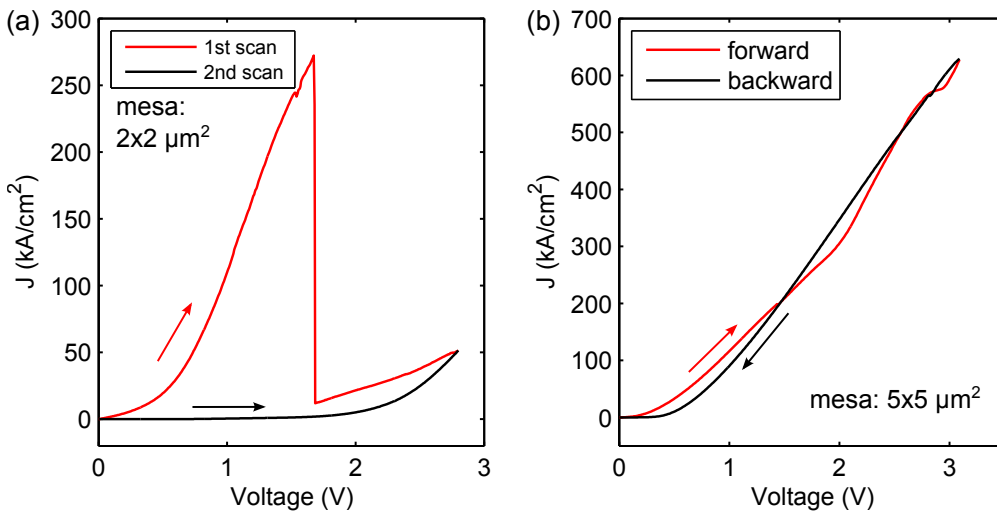


Figure 4.20 – Observed I-V features. (a) IV of A3 sample (on a small $2 \times 2 \mu\text{m}^2$ mesa): two consecutive forward scans. (b) I-V of W0 sample: forward and backward scan ($5 \times 5 \mu\text{m}^2$ mesa).

4.7.1 Observed features

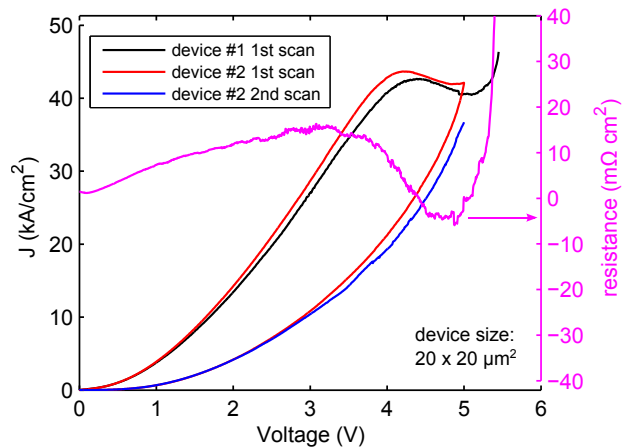
Concerning the N series (*cf.* Tab. 4.1), N1, N3 and N4 are all exhibiting an inflection point at positive bias, as depicted on Fig. 4.19(a), corresponding to the N3 sample. The N2 sample does not exhibit inflexion, but instable I-V curves, certainly because of process related issues. On the figure, the inflection occurs at ~ 3.5 V only for the first scan in forward direction. The backward scan does not show such feature. All subsequent scans are more or less superimposed with this backward scan. The I-V curve is highly asymmetric and looks like a Schottky rectifier. This asymmetry is more obvious in logarithmic scale, as presented on Fig. 4.19(b). On this

last graph, one can see that the hysteresis in the measurement is not only related to the disappearance of the inflection, but is also very strong for negative bias. The current density decreases by two orders of magnitude for the backward scan. This behaviour can be the signature of trapping effects. For N1, N2 and N3 the voltage corresponding to the inflection points are respectively 2.1 V, 3.5 V and 2.2 V. This tendency is not correlated with the theoretical predictions, as the increasing confinement energy of the quantized level is expected to result in an increasing resonance voltage. This indicates that the observed features are not likely related to resonant tunneling.

Let's now have a look at the samples of the two other series (A and W). A1 for instance (not shown) exhibits an inflection feature having the same characteristics as those of samples from A series: hysteresis and only for the first scan. The resonance voltage is about 1.9 V for this sample. This is again not consistent with the calculated predictions since the confinement energy close to zero should not induce any NDR. A3 sample presents some instability and non reproducible results from one device to another. Fig. 4.20(a) presents one of the measurements performed on a $2 \times 2 \mu\text{m}^2$ mesa, which looks like what is reported by Kikuchi *et al.* in 2002 [159]. This current instability could be related to processing issues due to the large current density ($250 \text{ kA}/\text{cm}^2$).

The I-V curve of W0 is given in Fig. 4.20(b). It presents two different inflections, which also both suffer from hysteresis. The corresponding voltages are 2 and 2.9 V. Finding two NDR-like features is surprising, since only one quantized state is found according to the simulations.

Figure 4.21 – Current voltage characteristics at room temperature of the asymmetric A2 sample.



One obvious NDR behaviour is observed on sample A2, having a PVR of 1.06, and a NDR of $\sim 5 \text{ m}\Omega \cdot \text{cm}^2$. This NDR is also reproducible from one device to another and observed up to $20 \times 20 \mu\text{m}^2$ mesa size. However, the resonance voltage of 5 V is too high comparing to other samples and the NDR disappears after the first scan.

To ensure that those measured effects are not related to contact annealing, which might be induced by the high current density, measurements have also been performed at different

scan speeds, and in pulsed mode. No change could be observed. Also measurements with both frontside and backside bottom contacts give similar I-V curves.

4.7.2 Effects low temperature measurements, and other treatments

Some of the samples presenting the most promising and reliable features (N3, N4 and A2) are chosen for low temperature measurements. Our set-up designed for low temperature transport measurements is equipped with a nitrogen cryostat enabling temperatures down to 100 K. There are four electric probes inside that cannot be moved once the cryostat is closed. Thus, only one or two devices can be measured within a day. Besides, due to the sample drifting when cooling down and the small size of the deposited contacts, the probes cannot be contacted directly and samples have to be bounded on a copper plate. This is not an easy task, as the mask is not designed for this purpose. Due to this tedious procedure, only very few devices have been characterized at low temperature.

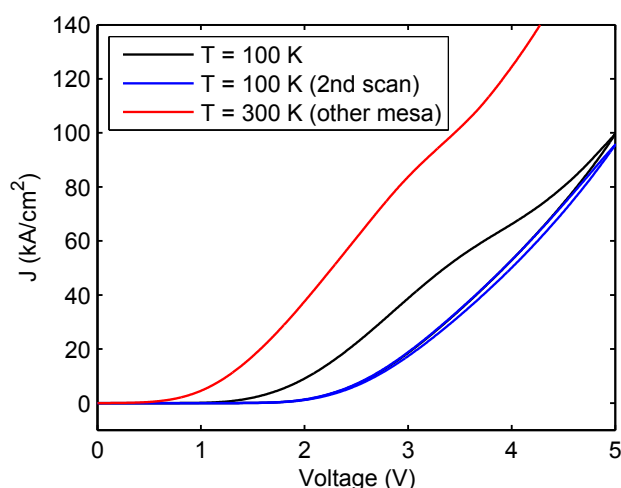


Figure 4.22 – I-V characteristic of N4 sample at low temperature (100 K) and at room temperature on two different devices (mesa size: $5 \times 5 \mu\text{m}^2$).

The I-V curves at low and room temperature of sample N4 are displayed in Fig. 4.22. No drastic improvement is observed. The device is just more resistive at low temperature, as expected in any semiconductor. The inflection is only present for the first scan and the same hysteresis behaviour is observed.

Other sample treatments have been attempted in order to check their impact on the transport characteristics. For instance, pre-processing high temperature thermal annealing has been tried. Samples have been annealed in an HVPE reactor at different temperatures (950° C and 1000° C) for one hour under ammonia pressure. This kind of treatment has been proven to improve the quality of MBE grown InGaN/GaN QWs [195]. However, in our case, it did not affect the sample properties, neither the transport measurements, nor the photoluminescence signal.

4.7.3 Summary of the results

To summarize this section, different designs of RTDs were grown and processed, using state of the art $\text{Al}_x\text{Ga}_{1-x}\text{N}$ ($0.1 \leq x \leq 0.15$) barriers with optimized MOVPE growth recipes. However, if some interesting features are observed such as NDR or smooth inflections, they suffer from the same drawbacks as the ones reported in the literature : an hysteresis between the forward and backward scans and a loss of the NDR after few scans. Recovery (for a few times) of NDR after application of a high negative voltage has been reported [160, 174]. However, due to the high conductivity of the layers and the specificities of the process, it was not possible to apply high negative voltage ($\leq -10\text{ V}$), without breaking down of the SiO_2 passivation layer. In addition, no correlation is observed between the simulated structure and the voltage of the NDR-like feature, hinting that they are not related to quantum resonant tunneling.

Besides, a majority of the samples exhibits high reproducibility from one device to another, within the same mesa size, as shown in Fig 4.19(a) and 4.21. Except for Fig. 4.20(b), all presented curves are similar over the whole sample. Furthermore, the dependence of the I-V curves on the mesa size is characterized by a softening of the NDR-like feature when going to larger mesas. No drastic change is observed, which contradicts a strong impact of dislocations. Finally, the current densities are very high, up to few $100\text{ kA}\cdot\text{cm}^{-2}$ for the smallest mesas, and are decreasing while increasing the mesa size. This can be explained by the high conductivity of the substrate, the absence of undoped spacer and the low barrier heights. However, this value is consistent to what is reported in the literature for such small mesas (*cf.* Fig. 4.6).

4.8 Characterizations of barrierless samples

4.8.1 Current-voltage characteristics

Following those unsatisfactory results, processing quality assessment has been carried out, on a structure grown in the same conditions as the RTDs, but without the active region, *i.e.* without any barrier. In other words, the sample simply consists of a GaN FS substrate, followed by a $1\text{ }\mu\text{m}$ GaN layer doped at $5 \times 10^{18}\text{ cm}^{-3}$, and capped by the 5 nm GaN layer doped at $2 \times 10^{19}\text{ cm}^{-3}$. Then the sample is processed following the same steps as for the RTDs. Both frontside and backside contacts are deposited. The measurements are performed using the parameter analyser and the probe station at room temperature. The sweeping voltage is applied on the top contact.

The observed I-V features are presented in Fig. 4.23. Surprisingly, NDR is observed on this sample (Fig. 4.23(c)). This feature is very reproducible from one device to another, as attested by the three measurements presented in Fig. 4.23(c), corresponding to three different mesas of the same size This NDR is seen on all devices, with a decrease of the PVR while increasing the

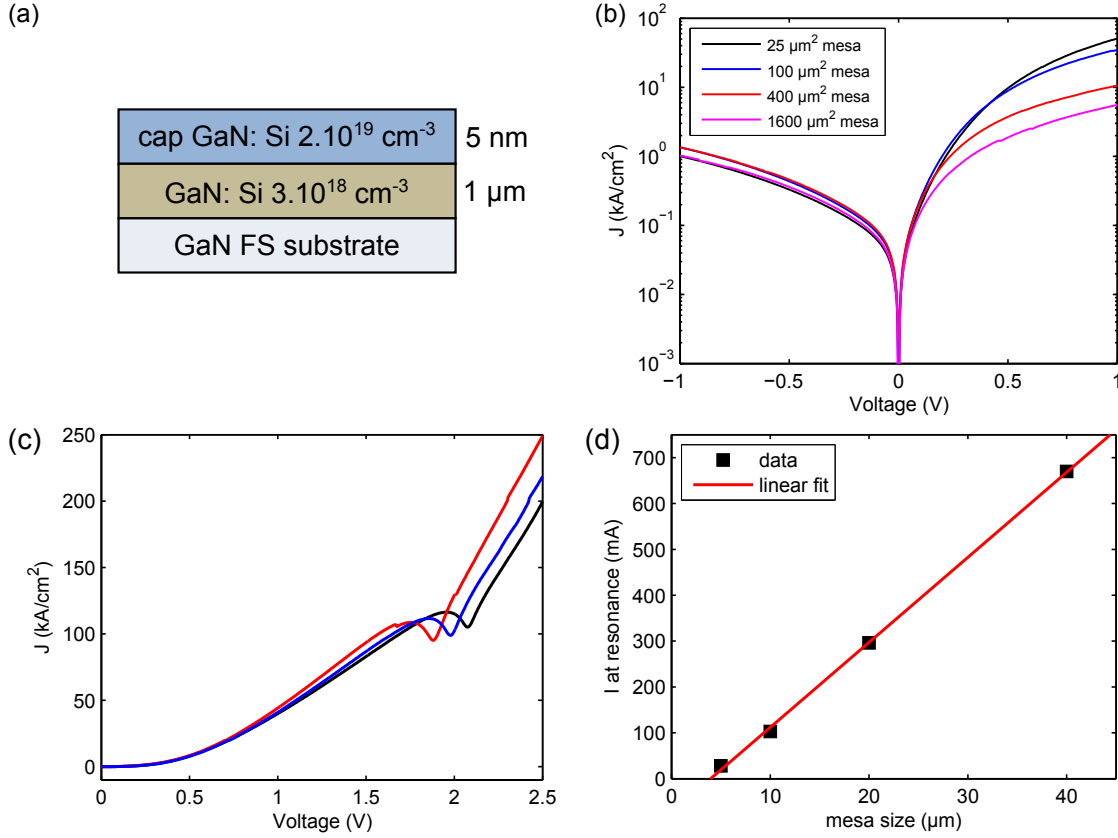


Figure 4.23 – (a) structure of the sample, and (b) current-voltage measurements for the different mesa sizes in logarithmic scale. (c) IV characteristics for the first scan of three different mesas of $10 \times 10 \mu\text{m}^2$. (d) evolution of the current at resonance with mesa perimeter ($\propto \sqrt{S}$).

meas size (*cf.* Fig. 4.24(a)). We found the same discrepancies as those observed on previously studied DB structures: hysteresis and the loss of NDR after the first scan. In addition, despite the absence of barriers, the I-V curve is asymmetric, and the current density can be up to two orders of magnitude lower at negative bias, compared to positive bias. It should be noticed that the current densities under negative voltage do not seem to depend on the mesa sizes (Fig. 4.23(b)).

Under positive voltages, the current densities change depending on the mesa size. This point is illustrated in Fig. 4.23(d), which represents the current (not the current density) at the local minimum of the NDR as a function of the mesa perimeter. The results show a clear linear dependence, while one should expect a quadratic dependence, *i.e.* proportional to the mesa surface, meaning that the current density is independent from the mesa size. To compare with Fig. 4.6, the present data exhibit also a power law behaviour:

$$J \propto S^\beta \quad \text{with} \quad \beta = -1,$$

where S is the surface and J the current density at the NDR-like feature.

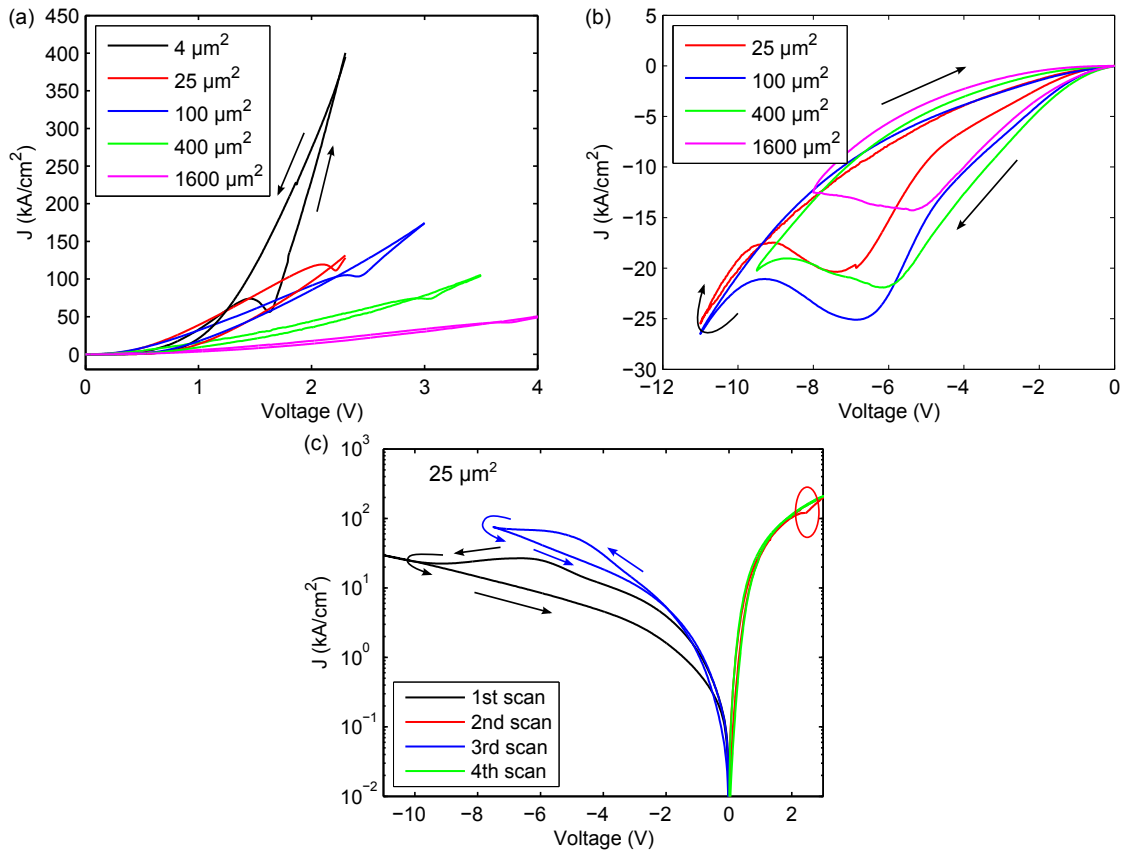


Figure 4.24 – I-V curves for barrierless sample for different mesa sizes under (a) positive and (b) negative bias. for (a) and (b), curves represent the first go and back scans of the device. (c) different scans on the same device ($5 \times 5 \mu\text{m}^2$), showing the recovery of the NDR.

A NDR feature is also measured in negative bias, but at higher voltage (~ -8 V). Contrary to the observed NDR in positive bias, the current densities and the corresponding voltages are nearly identical whatever the mesa size (*cf.* Fig. 4.24(b)). This feature could be recovered by applying a positive bias, as demonstrated on Fig. 4.24(c). The first scan corresponds to a forward and backward sweep from 0 V to -11 V, then from -11 V to 0 V: the NDR is observed. By repeating this measurement (not shown on the figure) the I-V curve superimposes with the second part of the previous measurement (from -11 V to 0 V). The next step is to scan at positive bias (0 V \rightarrow 2 V \rightarrow 0 V). Finally, redoing a scan at negative bias (0 V \rightarrow -8 V \rightarrow 0 V) recovers the first NDR-like feature. It is seen at the same voltage, but with a twice lower current density. Such kind of recovery can be explained by electron trapping and releasing.

It should be noticed that the feature observed at positive bias (red circle in Fig. 4.24(c)), is seen the first time (red curve), but not recovered after applying the negative scan.

4.8.2 Process issues

The fact that the current at the positive bias NDR increases linearly with \sqrt{S} instead of S (where S is the mesa surface), hints that some edge-related effects are probably involved. In order to verify this assumption and assess the quality of the process, SEM characterizations have been performed on the sample.

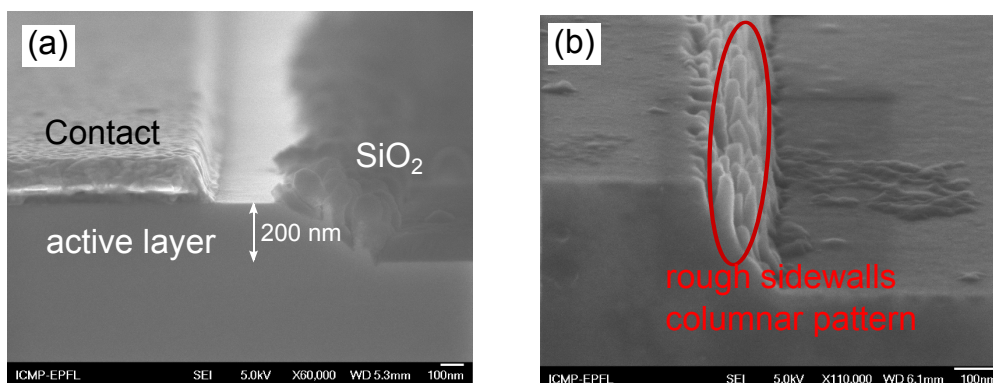


Figure 4.25 – Cross section SEM picture of a processed mesa (a), and after (b) wet-etching of oxide and metal contacts.

For this purpose, the processed sample is cleaved to observe the cross section. Fig. 4.25 shows the result of the SEM measurements. The etched depth is consistent with targeted value ($\sim 200 - 250$ nm), which ensures that the frontside bottom contact is below the active region. Besides the SiO_2 layer covers well the sidewalls of the mesa, which should prevent leakages from the edges. However, the SiO_2 layer appears to be extremely rough in the neighbouring of the mesa sidewalls. Taking the same picture after removal of the SiO_2 and the contacts reveals a high roughness at the border of the mesas, as shown in Fig. 4.25(b). In addition to the roughness, a columnar structure is observed. It can be originated from a non optimized photoresist development, which is tricky if one wants to resolve the smallest mesa, or directly from ICP dry-etching. One should notice that, following SEM observations on other processed samples, they do not all show such columnar structure. However, a high roughness is systematically observed.

This observation demonstrates the difficulty to process III-nitride materials, and particularly when scaling down the device size. It is clear that edge related effects will have more detrimental impacts on smaller devices. This can explain why the NDR-like features are smoothed when measured on bigger mesas.

In addition to this deleterious effect, one should notice that, in the developed self-aligned process, the mesas surfaces are directly exposed to the CHF_3 plasma used for the SiO_2 aperture prior to deposition of the frontside bottom contact. This exposure may also be source of surface damages and defects in the device. To test this effect the sample has been processed

without the oxide aperture, taking the bottom contact on backside. However, no improvement could be observed on the I-V curves.

All those observations may evidence that the choice to use a self-aligned process for RTDs is not judicious, since it seems to create damages that have detrimental influence on small devices. This kind of process is generally used in LDs to pattern the ridge waveguides in order to confine the optical mode. In this case, the GaN etching is shallow and does not cross the active region, which should not cause any leakage between the bottom (generally taken from the backside) and the top contact. This is not the case for our samples, where the mesas should be etched to confine the current.

4.8.3 Process without dry-etching of GaN

Following the previous study, and the assumption that dry-etching of GaN could be responsible for the observed discrepancies, another process has been investigated on similar barrierless structures. For this part, a set of masks dedicated to micro-LED has been used. The process consists in first covering the sample surface with PECVD deposited SiO₂ layer of 200 nm. Then the first lithographic step is used to create small circular holes in the oxide down to the GaN surface. The sizes of these circles are between 2 and 10 μm diameter. The SiO₂ is etched the same way as the previous process by CHF₃ plasma with RIE. Then a second mask is used to deposit the top contact (Ti/Al/Ti/Au). As no mesas are etched, the bottom contact is taken at the backside of the sample. A sketch of the processed sample is given in Fig. 4.26(a). One should notice that such a design, nevertheless free of dry-etching, presents the disadvantage to have less control of the current confinement.

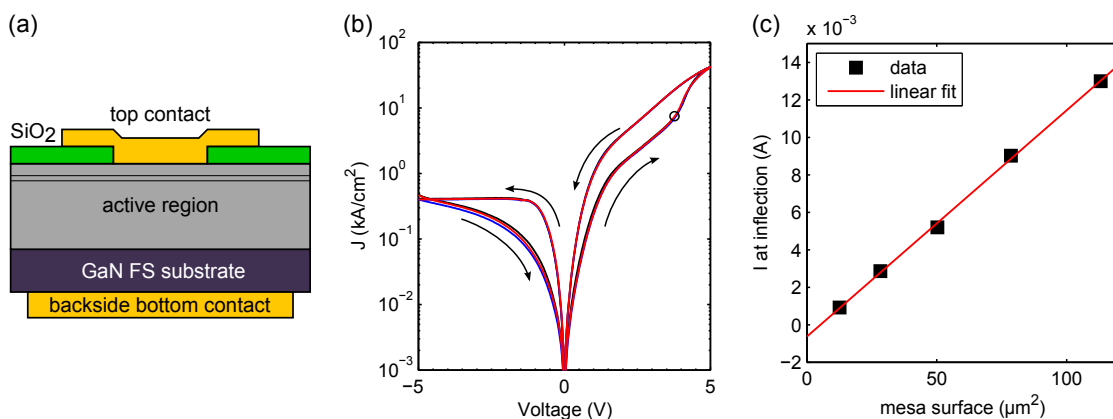


Figure 4.26 – (a) sketch of the free-etching process. (b) I-V characteristics of the same mesa: the arrows indicate the hysteresis curve, and the black circle corresponds to the position of the inflection point. (c) Current measured at the inflection point as a function of the mesa surface.

Fig. 4.26(b) is a typical I-V characteristics of a device (bias applied to top contact). The result is quite different from the other process. First, no NDR behaviour is measured at forward scan.

However, an inflection point is monitored. Interestingly, the current of this point scales with the surface of top contact (*i.e.* the circular aperture of the SiO₂), as shown in Fig. 4.26(c), which is in agreement with the expectations. In other words, the current density is independent from the device size. This means that the transport properties are not dominated by edge effect, which is an improvement comparing to the self-aligned process.

However, hysteretic features are observed, implying that the structure still presents some defects acting as electron traps. These defects might be originated from the GaN-SiO₂ interface. Interestingly, the hysteresis is perfectly recovered for more than 50 subsequent scans, which is not the case for the previous sample using the self-aligned process.

4.8.4 Summary of results on barrierless samples

Finally, to conclude this section, NDR-like features are observed on barrierless samples. The observed hysteresis and the fact that this NDRs can be recovered by electrical treatment, endorse the involvement of trapping effects in the transport measurements. Indeed, those curves can be explained by filling and emptying traps that modulate the conductivity of the layer. However, contrary to what is usually asserted, those traps are not necessarily originated from the AlN or AlGa_xN barrier. Following the obtained results on the two different processes, those traps can be attributed to process-induced defects, which can, for instance, occur during the dry-etching of the mesa (Fig. 4.25), or at the interface between GaN and the SiO₂ passivation layer. In order to be confirmed, those assertions require a deeper study of process related defects. Besides, to demonstrate that an observed NDR on RTD structures, one should always be cautious about this point, and make sure that the feature is originated from the double barrier structure. For instance, comparing the current densities with different mesa sizes, already gives a hint about the impact of edge-related defects.

4.9 Impact of disorder on the resonance: simulations

Following the numerous unsuccessful attempts to observe resonant tunneling, either from this work and from reported results in the literature, this section tentatively proposes an explanation for those discrepancies from a theoretical point of view.

The GaN/AlGa_xN system is known to suffer more from disorder than the GaAs/AlGa_xAs one. Besides, due to the internal electric field, together with the high effective electron mass in III-nitrides, it is expected that disorder has a stronger impact. This disorder is of two different types: the interface and the alloy disorders. Furthermore, still due to the high effective mass, and to the large band offsets (particularly for the AlN/GaN system) the thicknesses of barriers should be shorter in GaN/AlGa_xN system than in GaAs/AlGa_xAs system, which makes the structure intrinsically more sensitive to barriers and QWs thickness fluctuations. The

4.9. Impact of disorder on the resonance: simulations

following study proposes to assess the effects of alloy and interface disorder, using a simple model based on transfer matrix calculation. To our knowledge, no study about the impact of alloy disorder on GaN-based RTDs has been reported. One should notice that, under no circumstances, this model can explain the discrepancies of the I-V curves, *i.e.* the hysteresis and loss of NDR after few scans. However, it can give a hint about the origin of the numerous difficulties encountered to observe a proper NDR.

The aim is to study the impact of disorder in a GaN-based DB-RTD structure, and compare it systematically to a GaAs-based structure. For this purpose, simple band structure calculations are performed with Nextnano and the transmission curves are calculated at zero bias using the transfer matrix formalism described in section 4.2.3. The reference GaN-based structure is the same as N2 sample (*cf.* Tab. 4.1), *i.e.* one 4.5 nm GaN QW, sandwiched between two 2 nm $\text{Al}_{0.1}\text{Ga}_{0.9}\text{N}$ barriers. For the simulations, a doping concentration of $5 \times 10^{18} \text{ cm}^{-3}$ is assumed in the GaN cladding layers. For the GaAs-based structure, it is the same structure as the one presented in Ref. [189]. It is a $\text{Al}_{0.25}\text{Ga}_{0.75}\text{As} / \text{GaAs} / \text{Al}_{0.25}\text{Ga}_{0.75}\text{As}$ with respective thicknesses of 5 / 5 / 5 nm. The structure is directly simulated by the transfer matrix method at zero bias. The CBO is 0.23 eV, and the electron effective masses taken are $0.063 m_0$ and $0.083 m_0$ for the GaAs and the AlGaAs, respectively.

Following those initial structures, the disorder is simulated, by varying independently different parameters: the two barriers and QW thicknesses within ± 2 MLs deviation, and the alloy content within $\pm 2\%$ deviation. The two MLs deviation is chosen instead of 1 ML, since it has been demonstrated that III-nitride surfaces, grown in the (0001) direction, present double MLs step edges [196]. Finally, the results of the simulations are compared between the two structures. From the calculated transmission curves, three figures of merit are considered: the maximum of transmission, the transmission energy shift from the nominal structure, and the FWHM of the transmission peak. Note that the latest parameter is related to the resonant tunneling time, via the Heisenberg uncertainty relation (see Eq. 4.19).

Examples of the transmission calculations are given in Fig. 4.27. The left (*resp.* right) corresponds to the GaN-based (*resp.* GaAs-based) structure. The two figures on top are the results on simulating the monolayer fluctuations of the first barrier. From the figure, it is obvious that the impact is much stronger on GaN-based structure, as attests the large shift on the resonant energy. On the GaAs-based structure, no obvious shift is monitored. This colossal difference is simply explained by the presence of the internal polarization, which strongly depends on the thicknesses and changes the alignments in the band structure. On the other hand, for the GaAs-based structure, it is expected that thickness fluctuations have a limited impact due to the absence of internal field and to the large barriers (5 nm compared to 2 nm for GaN). The two figures below are the results for the Al content fluctuation in the barriers. Still, the consequences on the GaN-structures are more dramatic, than on GaAs. The internal electric

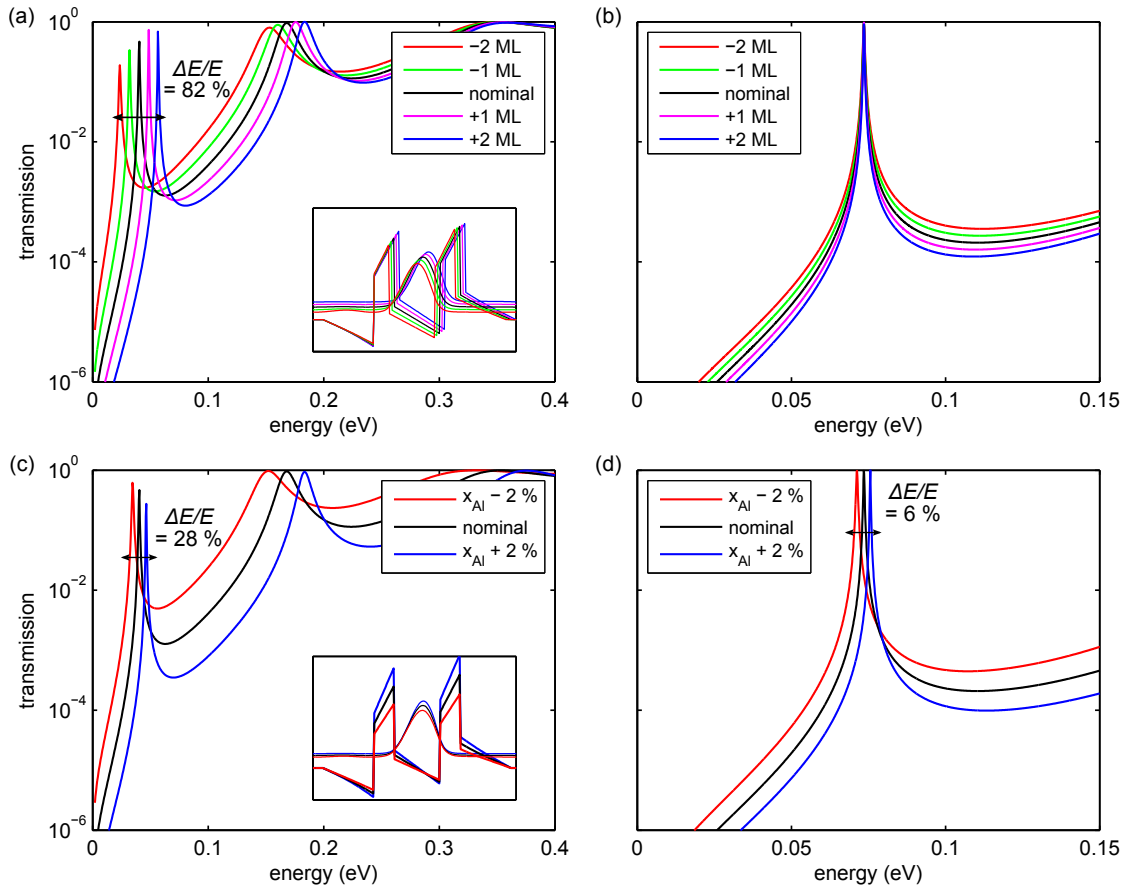


Figure 4.27 – Effect of disorder on on transmission of double barriers RTDs. On top: a ± 2 ML thickness fluctuation of the first barrier is considered for the (a) GaN-based and the (b) GaAs-based structures. Below: Al composition fluctuation in the barriers is considered for the (c) GaN-based and the (d) GaAs-based structures. the insets in (a) and (c) represent the corresponding band structures.

field is again the most responsible for this deviation.

All the other results from simulations are given in Tab. 4.3. In the first column, B1 and B2 stand for the thickness deviation of the first and second barriers respectively. Fluctuation of 1 ML and 2 ML are treated separately. The second part of the table concerns QW thickness fluctuations, and the last part, the Al content fluctuation in the barrier. The parameters for fluctuations in the second barrier are not given for GaAs since it is the same result as for first barrier, due to the symmetry of the structure. The column labelled $\Delta E/E$ gives, in percentage, the deviation of the resonant energy from the nominal structure. T_{max} is the value of the transmission at the resonance, and Γ the FWHM of the resonance peak.

From the $\Delta E/E$ column, it can be said that, for all kind of disorder considered, the GaAs-based structure is much more robust than the GaN-based one. The main reason of this discrepancy is the internal electric field, plus the thinner barriers that are necessary to promote tunneling

4.9. Impact of disorder on the resonance: simulations

Table 4.3 – Results of disorder simulations on the transmission curves. Comparison between the GaN based and GaAs-based samples. When two values are given, the first one corresponds to the "+" sign (*e.g.* +2 ML) and the second to the "-" sign (*e.g.* -2 ML).

structure	$\Delta E/E$		T_{max}		Γ (meV)	
	GaN	GaAs	GaN	GaAs	GaN	GaAs
nominal	E=39 meV	E=73.5 meV	0.57	1	0.75	0.39
B1±1 ML	±20 %	±0.1 %	0.81/0.35	0.98	0.6/1	0.34/0.45
B1±2 ML	±41 %	±0.3 %	0.98/0.19	0.91	0.5/1.4	0.30/0.55
B2±1 ML	∓15 %	–	0.31/0.87	–	0.6/1	–
B2±2 ML	∓32 %	–	0.15/1	–	0.5/1.5	–
QW±1 ML	∓10 %	∓5 %	0.60/0.55	1	0.6/1	0.33/0.46
QW±2 ML	∓20 %	∓11 %	0.62/0.54	1	0.5/1.3	0.29/0.53
$x_{Al} \pm 2\%$	±14 %	±3 %	0.49/0.65	1	0.44/1.32	0.27/0.56

because of the high effective mass. The other parameter T_{max} deviates strongly with the disorder, and can go down to 0.15. This value is related to the PVR of the RTD. In the contrary, the GaAs structure is highly robust to any kind of disorder, and T_{max} stays very close to the maximal value.

Another interesting observed feature is the enhancement of the transmission, when the structure is asymmetric. A second barrier which is 2 ML thinner than the first one seems to be favourable. This result is consistent with other reported simulations [154]. Due to the depletion region following the second barrier, reducing its thickness results in a "symmetrized" band profile. The transmission is thus enhanced.

Besides, it should be noticed that those calculations are carried out on low Al content barriers and with larger QWs than the usual RTDs structures based on AlN/GaN. Those latter structures are expected to suffer even more from interface disorder, as the electric field is stronger. Thin barriers are also intrinsically more sensitive to thickness fluctuations. Therefore, observing NDR in such system is expected to be even more challenging. Furthermore, III-nitrides suffer extrinsically more from disorder than III-arsenides, due to the different reasons explained earlier (*cf.* Sec. 2.3).

Finally, the simple model proposed, based on transfer matrix calculations at zero bias, can explain the difficulties encountered to observe NDR in GaN-based RTDs. Disorder in such structures appears to be a critical issue. With the calculated energy dispersion, the device performances in terms of figures of merit are expected to be dramatically reduced.

4.10 Conclusions

RTDs are the fundamental building block of ISB optoelectronic devices, and its demonstration is a decisive step towards the realization of QCLs. Since the first report of a GaN-based RTD in 2002 from the laboratory of K. Kishino [159], and the followed controversies [161, 162], several groups have attempted to demonstrate such devices, more or less successfully. However, most of the reported results present similar discrepancies: a hysteresis in the I-V curve, a loss of the NDR (if any) after one or few scans, and a strong asymmetry. So far, no doubtless evidence of resonant tunneling in GaN/(Al,Ga)N planar structure has been reported.

Following the state of the art quality GaN/Al_xGa_{1-x}N (0.1 ≤ x ≤ 0.15) single QWs that have been demonstrated in our laboratory, using optimized MOVPE growth recipes [5], we decided to plunge into the question of RTDs using such structures. A methodical approach is proposed, based on comprehensive simulations and a specially engineered process, allowing to downsize the mesa down to 4 × 4 μm², necessary to study the influence of dislocations.

Even if some interesting features have been observed, the transport measurements have revealed similar discrepancies as the other results reported in literature, and no clear correlation could be drawn between experimental values and theoretical predictions, denying any connection with resonant tunneling. Following this forfeit, deep investigation was carried on on processing issues. This study, done on barrierless samples, revealed that the usual observed discrepancies in I-V curves, usually attributed to electron trapping by deep defects in the AlGa_xN barriers, could originate from process related issues. It could be for instance due to sidewall damages of the mesa during GaN dry-etching, which is critical for ~μm size devices. Finally, a simple model is proposed to relate the difficulties to observe NDR in our structures with the disorder, which is known to be present in III-nitrides, and compare with a standard GaAs-based RTD. The results reveal that both the high effective mass and the polarization can be dramatic handicaps for GaN-based RTDs. This can also be taken as an explanation why the results obtained on nanowires [177] seem more reliable than those on planar structures. Indeed the very small size, plus the current confinement due to sidewall depletion, helps to probe at very small scale the RTD structure, reducing the impact of disorder.

5 Conclusions and perspectives

GaN and related materials, featuring a large CBOs and high LO-phonon energies (92 meV in GaN), appear to be suitable candidates for ISB applications, both in the near-IR and in the THz range. Previous studies have demonstrated their potential, particularly in the near infrared: devices, such as QCDs or modulators already exist. The interest in THz applications is more recent, but promising results, like absorption in GaN-based QWs, have been reported. However, a GaN-based QCL has not been demonstrated yet. Indeed, compared to conventional III-V semiconductors used for cutting edge ISB devices, GaN-based heterostructures suffer from large densities of defects mainly originating from the large lattice mismatch between the different III-nitride compounds, and the scarcity of high quality substrates. Together with interface and alloy disorder, which is known to occur in GaN/AlGaN based heterostructures, these defects are detrimental for the realization of QCLs.

The present work focused on the properties of GaN/AlGaN heterostructures, and their potential for the realization of advanced ISB optoelectronic devices. For this purpose, a systematic investigation about the growth, the material quality and related consequences was carried out. In this work two crucial building block devices towards the realization of QCLs have been investigated. First, QCDs, featuring similar quantum cascade SLs as in QCLs, are opportune devices to study the transport properties in such SLs. Then RTDs were deeply studied, as their demonstration is a necessary milestone to understand the mechanisms of resonant tunneling that govern the transport properties of most QCLs, and especially in the mid infrared spectral range ($\sim 4 - 20 \mu\text{m}$).

Concerning QCDs, this work demonstrates the feasibility of NH_3 -MBE grown complex quantum cascade structures for near-IR applications, whereas all previously reported similar devices were grown using PA-MBE. Those state of the art samples could be achieved thanks to optimized growth conditions. Interesting QCD designs were successfully demonstrated. The first one consisted in a two color QCD, that relies on the e_1e_3 ISB transition, usually

forbidden in square QWs. The operating wavelength of $\sim 1 \mu\text{m}$ is the shortest ever reported for an ISB device. Then a simplified design for QCDs was proposed, based on a 15 nm thick alloy extractor, instead of the more conventional SL-based quantum cascade structures. This simplified device, is advantageous, and should enable ultrafast operation *via* an efficient electron transfer. The design can also be adapted to operate at longer wavelengths. Besides, the photocurrent showed a very good stability with temperature.

The transport mechanisms involved in QCDs, are mostly mediated by scattering, rather than resonant tunneling. To investigate the vertical coherent transport across GaN/AlGa_N double barrier structures, a comprehensive study was performed, using state of the art MOVPE grown low Al content barriers, combined to a special design process. All the devices presented the same unexpected features in the I-V characteristics as reported in the literature, *i.e.* hysteresis and a rapid loss of the NDR feature. Further investigations demonstrated that those discrepancies be originate from processing issues, exacerbated when scaling down the device size. Finally, it was shown that simple calculations, which model the impact of alloy and interface disorder, can satisfactorily explain the difficulties encountered to observe an unambiguous resonant tunneling in GaN-based planar heterostructures.

If those last results can seem discouraging, it should be said that excellent quality MOVPE GaN/Al_xGa_{1-x}N ($x \leq 0.15$) structures have been demonstrated, using optimized growth conditions. Samples featuring an emission linewidth as low as $\sim 5 \text{ meV}$ at low temperature, confirm the very low inhomogeneous broadening. These results are very promising, regarding the realization of GaN-based QCLs operating in the THz range. Indeed, those layers have a reduced lattice-mismatch, compared to the GaN/AlN system, and are well adapted for growth on high quality GaN FS substrates. Furthermore, MOVPE is shown to be a suitable for complex GaN/AlGa_N structures. In addition, when going to the THz, GaAs/AlGaAs - based QCLs with the best performance are not based on miniband transport, but on LO-phonon assisted relaxation mechanism. Such designs are simpler from a growth point of view and might be adapted to GaN-based structures.

A Details of RTDs processing

This appendix details the self-aligned process, developed for RTDs. The mask contains different sizes of mesas, varying from $2 \times 2 \mu\text{m}^2$ to $40 \times 40 \mu\text{m}^2$.

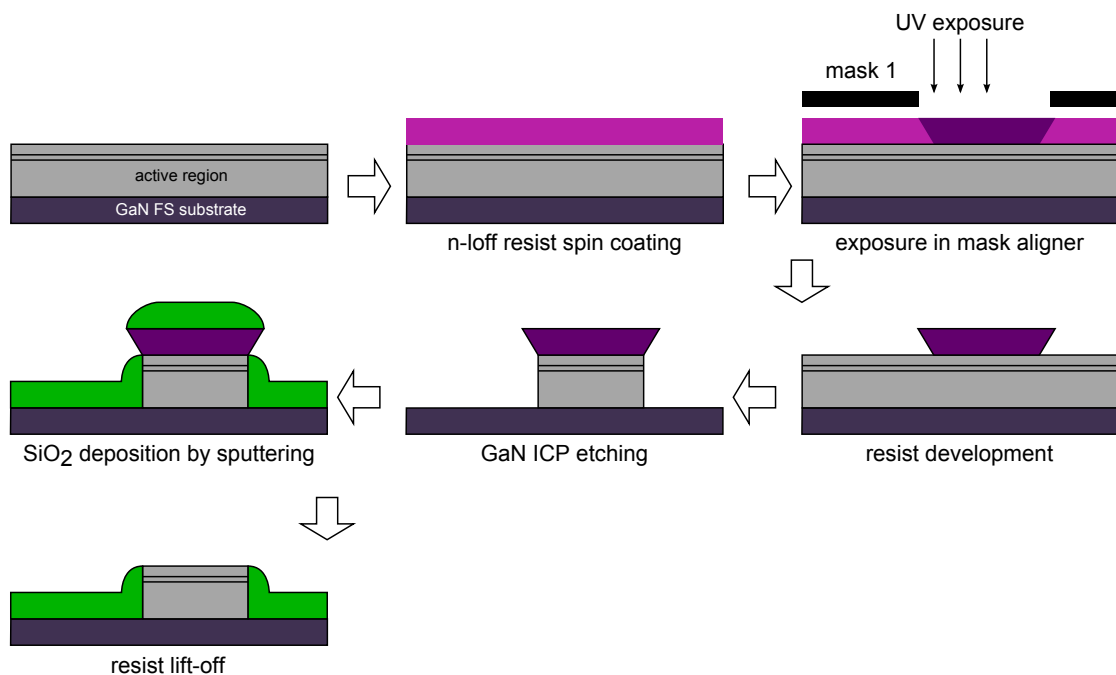


Figure A.1 – First level of RTD processing: mesa patterning and passivation using a self aligned process.

The first lithographic level is detailed in Fig. A.1. The sample is spin coated with the n-loff resist (negative). Then the first mask, containing the mesas is developed with standard UV lithographic techniques. Following that, the GaN is etched by ICP, using Ar/Cl₂ (27 / 80 sccm) mixture. The Plasma power is set to 50 W, and the RF generator to 100 W, giving etching rates of 90 nm/s. Following this step 200 nm of SiO₂ is deposited by sputtering. Then the lift-off is

Appendix A. Details of RTDs processing

performed in the 1665 resist remover, at 120° C for several hours. Note that for such result, it is necessary to use a negative resist to have the under-etched profile, in order to be able to perform the lift-off after the oxide deposition. PECVD deposition is also not possible, since this chemical deposition technique is not directional, and all the mesa will be covered, impeding the subsequent lift-off of the resist.

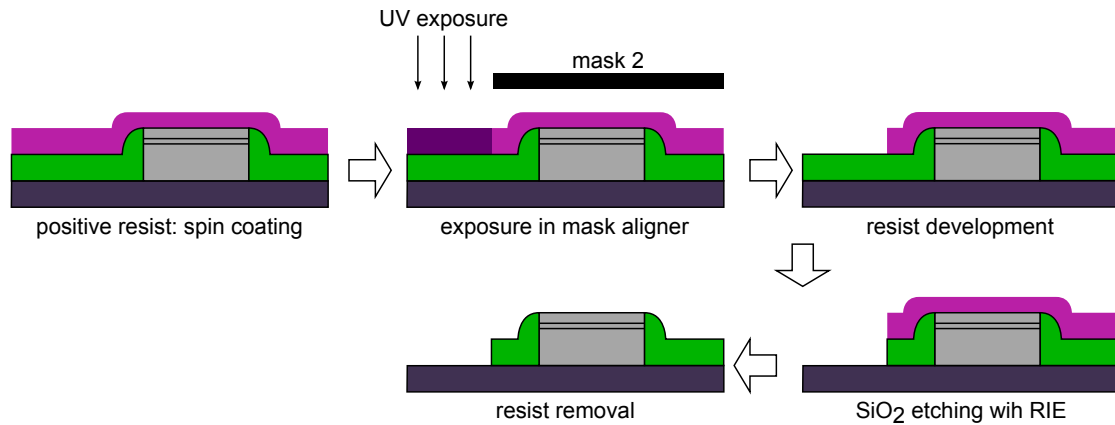


Figure A.2 – Second level of RTD processing: SiO₂ aperture.

The second step is detailed in Fig. A.2, and consists in the oxide aperture, prior to bottom contact deposition. It starts with a standard lithographic development of the second mask, using a positive photoresist. The sample is the dry-etched by RIE, using a CHF₃/Ar (25/25 sccm) mixture with a plasma power of 50 W. During this step, the mesa surface is exposed to the plasma, which can induce surface damages. Notice that this step can be skipped, if one want to avoid this plasma exposure, and only deposit a backside bottom contact.

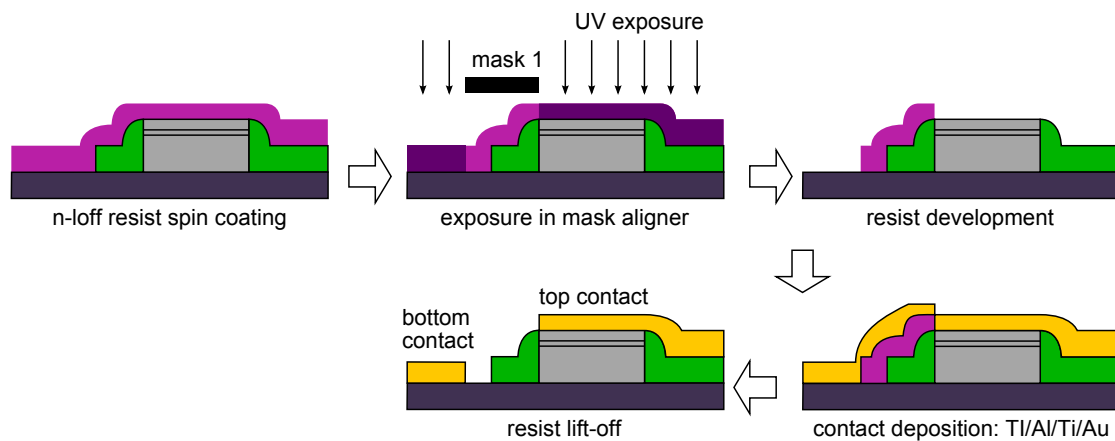


Figure A.3 – Third level of RTD processing: simultaneous top and bottom contacts deposition.

The last step is schematized in Fig. A.3. It starts with standard lithographic negative development of the third mask. Both contacts are deposited simultaneously in the electron beam

evaporator. The deposited contacts are Ti/Al/Ti/Au: 10/50/10/200 nm.

B List of acronyms

2DEG	2 dimensions electron gas
AFM	atomic force microscopy
CB	conduction Band
CBO	conduction band offset
c-GaN	cubic GaN (zb phase)
FIR	far infrared
FS	free standing
FTIR	Fourier transform infrared (spectrometer)
FPA	focal plane array
FWHM	full width at half maximum
ICP	inductively coupled plasma
IR	infrared
ISB(T)	intersubband (transition)
I-V	current voltage
LED	light emitting diode
LD	laser diode
LO	longitudinal optical
MBE	molecular beam epitaxy
MOVPE (or MOCVD)	metal-organic vapour phase epitaxy (chemical vapour deposition)
MQW	multi-quantum wells
NEP	noise equivalent power
NETD	noise equivalent temperature difference
NDR	negative differential resistance
NH ₃ -MBE	ammonia source molecular beam epitaxy
NIR	near infrared
PA-MBE	plasma-assisted molecular beam epitaxy
PECVD	plasma enhanced chemical vapour deposition
PIA	photo-induced absorption
PL	photo-luminescence
PVR	peak to valley ratio
QCD	quantum cascade detector
QCSE	quantum confined stark effect
QCL	quantum cascade laser

Appendix B. List of acronyms

QW	quantum well
QWIP	quantum well infrared photodetector
RHEED	reflection high energy electron diffraction
RIE	reactive ion etching
RTD	resonant tunneling diode
sccm	standard cubic centimeter per minute (flux unit)
SEM	scanning electron microscopy
SL	superlattice
SQW	single quantum well
TE	transverse electric
TEM	transmission electron microscopy
TM	transverse magnetic
TLM	transmission line method
VB	valence band
VBO	valence band offset
WG	waveguide
wz	wurtzite
XRD	X-ray diffraction
zb	zinc-blende

Bibliography

- [1] M Tchernycheva, L Nevou, L Doyennette, FH Julien, E Warde, F Guillot, E Monroy, E Bellet-Amalric, T Remmele, and M Albrecht. Systematic experimental and theoretical investigation of intersubband absorption in GaN/AlN quantum wells. *Phys. Rev. B*, 73(12):125347, 2006.
- [2] L Nevou, N Kheirodin, M Tchernycheva, L Meignien, P Crozat, A Lupu, E Warde, FH Julien, et al. Short-wavelength intersubband electroabsorption modulation based on electron tunneling between GaN/AlN coupled quantum wells. *Appl. Phys. Lett.*, 90(22):223511, 2007.
- [3] A Vardi, N Kheirodin, L Nevou, H Machhadani, L Vivien, P Crozat, M Tchernycheva, R Colombelli, FH Julien, F Guillot, et al. High-speed operation of GaN/AlGaIn quantum cascade detectors at $\lambda \sim 1.55 \mu\text{m}$. *Appl. Phys. Lett.*, 93(19):193509, 2008.
- [4] H Machhadani, Y Kotsar, S Sakr, M Tchernycheva, R Colombelli, J Mangeney, E Bellet-Amalric, E Sarigiannidou, E Monroy, and FH Julien. Terahertz intersubband absorption in GaN/AlGaIn step quantum wells. *Appl. Phys. Lett.*, 97(19):191101, 2010.
- [5] E Feltin, D Simeonov, J-F Carlin, R Butté, and N Grandjean. Narrow uv emission from homogeneous GaN/AlGaIn quantum wells. *Appl. Phys. Lett.*, 90(2):021905, 2007.
- [6] HP Maruska and JJ Tietjen. The preparation and properties of vapor-deposited single-crystal-line GaN. *Appl. Phys. Lett.*, 15(10):327, 1969.
- [7] R Dingle, DD Sell, SE Stokowski, and M Ilegems. Absorption, reflectance, and luminescence of GaN epitaxial layers. *Phys. Rev. B*, 4(4):1211, 1971.
- [8] H Amano, N Sawaki, I Akasaki, and Y Toyoda. Metalorganic vapor phase epitaxial growth of a high quality GaN film using an AlN buffer layer. *Appl. Phys. Lett.*, 48(5):353, 1986.
- [9] H Amano, M Kito, K Hiramatsu, and I Akasaki. P-type conduction in Mg-doped GaN treated with low-energy electron beam irradiation (LEEBI). *Jpn. J. Appl. Phys.*, 28(12A):L2112, 1989.
- [10] I Akasaki, H Amano, M Kito, and K Hiramatsu. Photoluminescence of Mg-doped p-type GaN and electroluminescence of GaN pn junction LED. *Journal of Luminescence*, 48-49:666, 1991.
- [11] S Nakamura. GaN growth using GaN buffer layer. *Jpn. J. Appl. Phys.*, 30(10A):L1705, 1991.
- [12] S Nakamura, T Mukai, M Senoh, and N Iwasa. Thermal annealing effects on p-type Mg-doped GaN films. *Jpn. J. Appl. Phys.*, 31(2B):L139, 1992.
- [13] S Nakamura, T Mukai, and M Senoh. Candela-class high-brightness InGaIn/AlGaIn double-heterostructure blue-light-emitting diodes. *Appl. Phys. Lett.*, 64(13):1687, 1994.
- [14] S Nakamura, M Senoh, S Nagahama, N Iwasa, T Yamada, Tand Y Sugimoto. InGaIn-based multi-quantum-well-structure laser diodes. *Jpn. J. Appl. Phys.*, 35(1B):L74, 1996.
- [15] I Vurgaftman and JR Meyer. Band parameters for nitrogen-containing semiconductors. *J. of Appl. Physics*, 94(6):3675, 2003.

Bibliography

- [16] O Ambacher, J Majewski, C Miskys, Al Link, M Hermann, M Eickhoff, M Stutzmann, F Bernardini, V Fiorentini, V Tilak, et al. Pyroelectric properties of (Al,In)GaN/GaN hetero- and quantum well structures. *J. Phys.: Condens. Matter*, 14(13):3399, 2002.
- [17] J Wu. When group-III nitrides go infrared: New properties and perspectives. *J. of Appl. Physics*, 106(1):011101, 2009.
- [18] J Wu, W Walukiewicz, W Shan, KM Yu, JW Ager III, SX Li, EE Haller, Hai Lu, and William J Schaff. Temperature dependence of the fundamental band gap of InN. *J. of Appl. Physics*, 94(7):4457, 2003.
- [19] CG Van de Walle and J Neugebauer. Universal alignment of hydrogen levels in semiconductors, insulators and solutions. *Nature*, 423(6940):626, 2003.
- [20] YP Varshni. Temperature dependence of the energy gap in semiconductors. *Physica*, 34(1):149, 1967.
- [21] LC de Carvalho, A Schleife, and F Bechstedt. Influence of exchange and correlation on structural and electronic properties of AlN, GaN, and InN polytypes. *Phys. Rev. B*, 84(19):195105, 2011.
- [22] SL Chuang and CS Chang. $\mathbf{k} \cdot \mathbf{p}$ method for strained wurtzite semiconductors. *Phys. Rev. B*, 54(4):2491, 1996.
- [23] F Bernardini, V Fiorentini, and D Vanderbilt. Accurate calculation of polarization-related quantities in semiconductors. *Phys. Rev. B*, 63(19):193201, 2001.
- [24] D Holec, Y Zhang, DVS Rao, MJ Kappers, C McAleese, and CJ Humphreys. Equilibrium critical thickness for misfit dislocations in III-nitrides. *J. Appl. Phys.*, 104(12):123514, 2008.
- [25] V Fiorentini, F Bernardini, and O Ambacher. Evidence for nonlinear macroscopic polarization in III-V nitride alloy heterostructures. *Appl. Phys. Lett.*, 80(7):1204–1206, 2002.
- [26] R Dwiliński, R Doradziński, J Garczyński, LP Sierzputowski, A Puchalski, Y Kanbara, K Yagi, H Minakuchi, and H Hayashi. Excellent crystallinity of truly bulk ammonothermal GaN. *J. Cryst. Growth*, 310(17):3911, 2008.
- [27] AY Cho and JR Arthur. Molecular beam epitaxy. *Prog. Solid State Chem.*, 10:157, 1975.
- [28] BM McSkimming, F Wu, T Huault, C Chaix, and JS Speck. Plasma assisted molecular beam epitaxy of GaN with growth rates $> 2.6 \mu\text{m/h}$. *J. Cryst. Growth*, 386:168, 2014.
- [29] N Grandjean and J Massies. GaN and $\text{Al}_x\text{Ga}_{1-x}\text{N}$ molecular beam epitaxy monitored by reflection high-energy electron diffraction. *Appl. Phys. Lett.*, 71(13):1816, 1997.
- [30] MA Moram and ME Vickers. X-ray diffraction of III-nitrides. *Rep. Prog. Phys.*, 72(3):036502, 2009.
- [31] K Kornitzer, T Ebner, K Thonke, R Sauer, C Kirchner, V Schwegler, M Kamp, M Leszczynski, I Grzegory, and S Porowski. Photoluminescence and reflectance spectroscopy of excitonic transitions in high-quality homoepitaxial GaN films. *Phys. Rev. B*, 60(3):1471, 1999.
- [32] M Leroux, N Grandjean, M Laügt, J Massies, B Gil, P Lefebvre, and P Bigenwald. Quantum confined Stark effect due to built-in internal polarization fields in (Al,Ga)N/GaN quantum wells. *Phys. Rev. B*, 58(20):R13371, 1998.
- [33] VA Fonoberov and AA Balandin. Excitonic properties of strained wurtzite and zinc-blende GaN/ $\text{al}_x\text{ga}_{1-x}\text{n}$ quantum dots. *J. Appl. Phys.*, 94(11):7178–7186, 2003.
- [34] UME Christmas, AD Andreev, and DA Faux. Calculation of electric field and optical transitions in InGaN/GaN quantum wells. *J. Appl. Phys.*, 98(7):073522, 2005.
- [35] DAB Miller, DS Chemla, TC Damen, AC Gossard, W Wiegmann, TH Wood, and CA Burrus. Band-edge electroabsorption in quantum well structures: the quantum-confined Stark effect. *Phys. Rev. Lett.*, 53(22):2173, 1984.

- [36] N Grandjean, B Damilano, S Dalmaso, M Leroux, M Lügt, and J Massies. Built-in electric-field effects in wurtzite AlGa_N/Ga_N quantum wells. *J. Appl. Phys.*, 86(7):3714, 1999.
- [37] Evan O Kane. Band structure of indium antimonide. *J. Phys. Chem. Solids*, 1(4):249, 1957.
- [38] Gerald Bastard. *Wave mechanics applied to semiconductors*. Les editions de Physique (CNRS, Paris, 1988), 1988.
- [39] <http://www.nextnano.de>.
- [40] E Rosencher and B Vinter. *Optoélectronique*. Dunod, Paris, 2002.
- [41] W Terashima and H Hirayama. Spontaneous emission from Ga_N/AlGa_N terahertz quantum cascade laser grown on Ga_N substrate. *Phys. Stat. Sol. (c)*, 8(7-8):2302, 2011.
- [42] LC West and SJ Eglash. First observation of an extremely large-dipole infrared transition within the conduction band of a GaAs quantum well. *Appl. Phys. Lett.*, 46(12):1156–1158, 1985.
- [43] BF Levine, KK Choi, CG Bethea, J Walker, and RJ Malik. New 10 μm infrared detector using inter-subband absorption in resonant tunneling GaAlAs superlattices. *Appl. Phys. Lett.*, 50(16):1092, 1987.
- [44] D Hofstetter, M Beck, and J Faist. Quantum-cascade-laser structures as photodetectors. *Appl. Phys. Lett.*, 81(15):2683, 2002.
- [45] L Gendron, M Carras, A Huynh, V Ortiz, C Koeniguer, and V Berger. Quantum cascade photodetector. *Appl. Phys. Lett.*, 85(14):2824, 2004.
- [46] A Harwit and JS Harris Jr. Observation of stark shifts in quantum well intersubband transitions. *Appl. Phys. Lett.*, 50(11):685, 1987.
- [47] N Vodjdani, B Vinter, V Berger, E Böckenhoff, and E Costard. Tunneling assisted modulation of the intersubband absorption in double quantum wells. *Appl. Phys. Lett.*, 59(5):555, 1991.
- [48] F Capasso, C Gmachl, DL Sivco, and AY Cho. Quantum cascade lasers. *Physics Today*, 55(5):34, 2002.
- [49] M Helm, E Colas, P England, F DeRosa, and SJ Allen Jr. Observation of grating-induced intersubband emission from GaAs/AlGaAs superlattices. *Appl. Phys. Lett.*, 53(18):1714, 1988.
- [50] J Faist, F Capasso, DL Sivco, C Sirtori, AL Hutchinson, and AY Cho. Quantum cascade laser. *Science*, 264(5158):553, 1994.
- [51] RF Kazarinov and RA Suris. On a possibility of amplifying electromagnetic waves in a superlattice semiconductor. *Sov. Phys - Semicond.*, 5(4):707, 1971.
- [52] R Köhler, A Tredicucci, F Beltram, HE Beere, EH Linfield, AG Davies, DA Ritchie, RC Iotti, and F Rossi. Terahertz semiconductor-heterostructure laser. *Nature*, 417(6885):156, 2002.
- [53] S Kumar, CWI Chan, Q Hu, and JL Reno. A 1.8-THz quantum cascade laser operating significantly above the temperature of $\hbar\omega/k_B$. *Nature Phys.*, 7(2):166, 2011.
- [54] S Fatholouloumi, E Dupont, CWI Chan, ZR Wasilewski, SR Laframboise, D Ban, A Mátyás, C Jirauschek, Q Hu, and HC Liu. Terahertz quantum cascade lasers operating up to $\sim 200\text{K}$ with optimized oscillator strength and improved injection tunneling. *Opt. Express*, 20(4):3866, 2012.
- [55] J Faist. *Quantum cascade lasers*. Oxford University Press, 2013.
- [56] O Gauthier-Lafaye, P Boucaud, FH Julien, S Sauvage, S Cabaret, J-M Lourtioz, V Thierry-Mieg, and R Planel. Long-wavelength ($\approx 15.5\ \mu\text{m}$) unipolar semiconductor laser in GaAs quantum wells. *Appl. Phys. Lett.*, 71(25):3619, 1997.
- [57] Di Dini, R Köhler, A Tredicucci, G Biasiol, and L Sorba. Microcavity polariton splitting of inter-subband transitions. *Phys. Rev. Lett.*, 90(11):116401, 2003.

Bibliography

- [58] R Colombelli, C Ciuti, Y Chassagneux, and C Sirtori. Quantum cascade intersubband polariton light emitters. *Semicond. Sci. Technol.*, 20(10):985, 2005.
- [59] JH Smet, LH Peng, Y Hirayama, and CG Fonstad. Electron intersubband transitions to 0.8 eV (1.55 μm) in InGaAs/AlAs single quantum wells. *Appl. Phys. Lett.*, 64(8):986–987, 1994.
- [60] R Akimoto, Y Kinpara, K Akita, F Sasaki, and S Kobayashi. Short-wavelength intersubband transitions down to 1.6 μm in ZnSe/BeTe type-II superlattices. *Appl. Phys. Lett.*, 78(5):580–582, 2001.
- [61] O Cathabard, R Teissier, J Devenson, JC Moreno, and AN Baranov. Quantum cascade lasers emitting near 2.6 μm . *Appl. Phys. Lett.*, 96(14):141110, 2010.
- [62] N Suzuki and N Iizuka. Feasibility study on ultrafast nonlinear optical properties of 1.55 μm intersubband transition in AlGaN/GaN quantum wells. *Jpn. J. Appl. Phys.*, 36(8A):L1006, 1997.
- [63] N Suzuki and N Iizuka. Electron scattering rates in AlGaN/GaN quantum wells for 1.55- μm inter-subband transition. *Jpn. J. Appl. Phys.*, 37(4A):L369, 1998.
- [64] N Suzuki and N Iizuka. Effect of polarization field on intersubband transition in AlGaN/GaN quantum wells. *Jpn. J. Appl. Phys.*, 38(4A):L363, 1999.
- [65] N Iizuka, K Kaneko, N Suzuki, T Asano, S Noda, and O Wada. Ultrafast intersubband relaxation (≤ 150 fs) in AlGaN/GaN multiple quantum wells. *Appl. Phys. Lett.*, 77(5):648, 2000.
- [66] C Gmachl, HM Ng, and AY Cho. Intersubband absorption in GaN/AlGaN multiple quantum wells in the wavelength range of $\lambda \sim 1.75$ -4.2 μm . *Appl. Phys. Lett.*, 77(3):334, 2000.
- [67] C Gmachl, HM Ng, SNG Chu, and AY Cho. Intersubband absorption at $\lambda \sim 1.55$ μm in well-and modulation-doped GaN/AlGaN multiple quantum wells with superlattice barriers. *Appl. Phys. Lett.*, 77(23):3722, 2000.
- [68] N Iizuka, K Kaneko, and N Suzuki. Near-infrared intersubband absorption in GaN/AlN quantum wells grown by molecular beam epitaxy. *Appl. Phys. Lett.*, 81(10):1803, 2002.
- [69] K Kishino, A Kikuchi, H Kanazawa, and T Tachibana. Intersubband transition in $(\text{GaN})_m/(\text{AlN})_n$ superlattices in the wavelength range from 1.08 to 1.61 μm . *Appl. Phys. Lett.*, 81(7):1234, 2002.
- [70] C Gmachl, HM Ng, and AY Cho. Intersubband absorption in degenerately doped GaN/ $\text{Al}_x\text{Ga}_{1-x}\text{N}$ coupled double quantum wells. *Appl. Phys. Lett.*, 79(11):1590, 2001.
- [71] K Driscoll, A Bhattacharyya, T D Moustakas, R Paiella, L Zhou, and DJ Smith. Intersubband absorption in AlN/ GaN/ AlGaN coupled quantum wells. *Appl. Phys. Lett.*, 91(14):141104, 2007.
- [72] S Nicolay, J-F Carlin, E Felton, R Butte, M Mosca, N Grandjean, M Ilegems, M Tchernycheva, L Nevou, and FH Julien. Midinfrared intersubband absorption in lattice-matched AlInN/GaN multiple quantum wells. *Appl. Phys. Lett.*, 87(11):111106, 2005.
- [73] L Nevou, FH Julien, R Colombelli, F Guillot, and E Monroy. Room-temperature intersubband emission of GaN/AlN quantum wells at $\lambda = 2.3$ μm . *Electron. Lett.*, 42(22):1308, 2006.
- [74] L Nevou, M Tchernycheva, FH Julien, F Guillot, and E Monroy. Short wavelength ($\lambda = 2.13$ μm) intersubband luminescence from GaN/AlN quantum wells at room temperature. *Appl. Phys. Lett.*, 90(12):121106, 2007.
- [75] Kristina Driscoll, Yitao Liao, Anirban Bhattacharyya, Lin Zhou, David J Smith, Theodore D Moustakas, and Roberto Paiella. Optically pumped intersubband emission of short-wave infrared radiation with GaN/AlN quantum wells. *Appl. Phys. Lett.*, 94(8):081120, 2009.
- [76] D Hofstetter, SS Schad, H Wu, WJ Schaff, and LF Eastman. GaN/AlN-based quantum-well infrared photodetector for 1.55 μm . *Appl. Phys. Lett.*, 83(3):572, 2003.

- [77] A Vardi, G Bahir, F Guillot, C Bougerol, E Monroy, SE Schacham, M Tchernycheva, and FH Julien. Near infrared quantum cascade detector in GaN/ AlGaIn/ AlN heterostructures. *Appl. Phys. Lett.*, 92(1):011112, 2008.
- [78] A Vardi, N Akopian, G Bahir, L Doyennette, M Tchernycheva, L Nevou, FH Julien, F Guillot, and E Monroy. Room temperature demonstration of GaN/AlN quantum dot intraband infrared photodetector at fiber-optics communication wavelength. *Appl. Phys. Lett.*, 88(14):143101, 2006.
- [79] L Doyennette, L Nevou, M Tchernycheva, A Lupu, F Guillot, E Monroy, R Colombelli, and FH Julien. GaN-based quantum dot infrared photodetector operating at 1.38 μm . *Electron. Lett.*, 41(19):1077, 2005.
- [80] Y Song, R Bhat, TY Huang, P Badami, CE Zah, and C Gmachl. III-nitride quantum cascade detector grown by metal organic chemical vapor deposition. *Appl. Phys. Lett.*, 105(18):182104, 2014.
- [81] N Iizuka, K Kaneko, and N Suzuki. Sub-picosecond modulation by intersubband transition in ridge waveguide with GaN/AlN quantum wells. *Electron. Lett.*, 40(15):962, 2004.
- [82] N Iizuka, K Kaneko, and N Suzuki. Sub-picosecond all-optical gate utilizing an intersubband transition. *Opt. Express*, 13(10):3835, 2005.
- [83] N Iizuka, K Kaneko, and N Suzuki. All-optical switch utilizing intersubband transition in GaN quantum wells. *Quantum Electron., IEEE Journal of*, 42(8):765, 2006.
- [84] E Baumann, FR Giorgetta, D Hofstetter, S Leconte, F Guillot, E Bellet-Amalric, and E Monroy. Electrically adjustable intersubband absorption of a GaN/ AlN superlattice grown on a transistorlike structure. *Appl. Phys. Lett.*, 89(10):101121, 2006.
- [85] N Kheirodin, L Nevou, H Machhadani, P Crozat, L Vivien, M Tchernycheva, A Lupu, FH Julien, Gianmauro Pozzovivo, Sebastian Golka, et al. Electrooptical modulator at telecommunication wavelengths based on GaN–AlN coupled quantum wells. *Photon. Technol. Lett., IEEE*, 20(9):724, 2008.
- [86] VD Jovanović, D Indjin, Z Ikonić, and P Harrison. Simulation and design of GaN/AlGaIn far-infrared ($\lambda \sim 34 \mu\text{m}$) quantum-cascade laser. *Appl. Phys. Lett.*, 84(16):2995, 2004.
- [87] G Sun, RA Soref, and JB Khurgin. Active region design of a terahertz GaN/Al_{0.15}Ga_{0.85}N quantum cascade laser. *Superlattices and Microstruct.*, 37(2):107, 2005.
- [88] E Bellotti, K Driscoll, TD Moustakas, and R Paiella. Monte Carlo study of GaN versus GaAs terahertz quantum cascade structures. *Appl. Phys. Lett.*, 92(10):101112, 2008.
- [89] F F Sudradjat, W Zhang, J Woodward, H Durmaz, TD Moustakas, and R Paiella. Far-infrared intersubband photodetectors based on double-step III-nitride quantum wells. *Appl. Phys. Lett.*, 100(24):241113, 2012.
- [90] W Terashima and H Hirayama. Design and fabrication of terahertz quantum cascade laser structure based on III-nitride semiconductors. *Phys. Stat. Sol. (c)*, 6(S2):S615, 2009.
- [91] JB Johnson. Thermal agitation of electricity in conductors. *Phys. Rev.*, 32(1):97, 1928.
- [92] H Schneider and HC Liu. *Quantum well infrared photodetectors*. Springer, 2007.
- [93] WA Beck. Photoconductive gain and generation-recombination noise in multiple-quantum-well infrared detectors. *Appl. Phys. Lett.*, 63(26):3589, 1993.
- [94] A Kastalsky, T Duffield, SJ Allen, and J Harbison. Photovoltaic detection of infrared light in a GaAs/AlGaAs superlattice. *Appl. Phys. Lett.*, 52(16):1320, 1988.
- [95] H Schneider, EC Larkins, JD Ralston, K Schwarz, F Fuchs, and P Koidl. Space-charge effects in photovoltaic double barrier quantum well infrared detectors. *Appl. Phys. Lett.*, 63(6):782, 1993.

Bibliography

- [96] C Schönbein, H Schneider, G Bihlmann, K Schwarz, and P Koidl. A 10 μm GaAs/Al_xGa_{1-x}As intersubband photodetector operating at zero bias voltage. *Appl. Phys. Lett.*, 68(7):973, 1996.
- [97] H Schneider, C Schönbein, M Walther, K Schwarz, J Fleissner, and P Koidl. Photovoltaic quantum well infrared photodetectors: The four-zone scheme. *Appl. Phys. Lett.*, 71(2):246, 1997.
- [98] L Gendron, C Koeniguer, V Berger, and X Marcadet. High resistance narrow band quantum cascade photodetectors. *Appl. Phys. Lett.*, 86(12):121116, 2005.
- [99] M Graf, G Scalari, D Hofstetter, J Faist, H Beere, E Linfield, D Ritchie, and G Davies. Terahertz range quantum well infrared photodetector. *Appl. Phys. Lett.*, 84(4):475, 2004.
- [100] FR Giorgetta, E Baumann, M Graf, Q Yang, C Manz, K Kohler, HE Beere, DA Ritchie, E Linfield, AG Davies, et al. Quantum cascade detectors. *Quantum Electron., IEEE Journal of*, 45(8):1029, 2009.
- [101] A Buffaz, M Carras, L Doyennette, A Nedelcu, P Bois, and V Berger. State of the art of quantum cascade photodetectors. In *SPIE Defense, Security, and Sensing*, page 76603Q. International Society for Optics and Photonics, 2010.
- [102] C Koeniguer, G Dubois, A Gomez, and V Berger. Electronic transport in quantum cascade structures at equilibrium. *Phys. Rev. B*, 74(23):235325, 2006.
- [103] A Gomez, N Péré-Laperne, LA De Vaulchier, C Koeniguer, A Vasanelli, A Nedelcu, X Marcadet, Y Guldner, and V Berger. Dark current analysis of quantum cascade detectors by magnetoresistance measurements. *Phys. Rev. B*, 77(8):085307, 2008.
- [104] R Ferreira and G Bastard. Evaluation of some scattering times for electrons in unbiased and biased single- and multiple-quantum-well structures. *Phys. Rev. B*, 40(2):1074, 1989.
- [105] F R Giorgetta, E Baumann, D Hofstetter, C Manz, Q Yang, K Kohler, and M Graf. InGaAs/AlAsSb quantum cascade detectors operating in the near infrared. *Appl. Phys. Lett.*, 91(11):111115, 2007.
- [106] S Sakr, P Crozat, D Gacemi, Y Kotsar, A Pesach, P Quach, N Isac, M Tchernycheva, L Vivien, G Bahir, et al. GaN/AlGaN waveguide quantum cascade photodetectors at $\lambda \approx 1.55 \mu\text{m}$ with enhanced responsivity and 40 GHz frequency bandwidth. *Appl. Phys. Lett.*, 102(1):011135, 2013.
- [107] A Buffaz, M Carras, L Doyennette, V Trinite, X Marcadet, and V Berger. Long range resonant tunneling in quantum cascade structures. *Appl. Phys. Lett.*, 96(16):162103, 2010.
- [108] A Dussaigne, S Nicolay, D Martin, A Castiglia, N Grandjean, L Nevou, H Machhadani, M Tchernycheva, L Vivien, FH Julien, et al. Growth of intersubband GaN/AlGaN heterostructures. In *OPTO*, page 76080H. International Society for Optics and Photonics, 2010.
- [109] S Nicolay. *Physics and applications of intersubband transitions in nitride based heterostructures*. PhD thesis, École Polytechnique Fédérale de Lausanne, 2008.
- [110] S Nicolay, E Feltin, J-F Carlin, N Grandjean, L Nevou, FH Julien, M Schmidbauer, T Remmele, and M Albrecht. Strain-induced interface instability in GaN/AlN multiple quantum wells. *Appl. Phys. Lett.*, 91(6):061927, 2007.
- [111] I Waki, C Kumtornkittikul, Y Shimogaki, and Y Nakano. Shortest intersubband transition wavelength (1.68 μm) achieved in AlN/GaN multiple quantum wells by metalorganic vapor phase epitaxy. *Appl. Phys. Lett.*, 82(25):4465, 2003.
- [112] I Waki, C Kumtornkittikul, Y Shimogaki, and Y Nakano. Erratum: "shortest intersubband transition wavelength (1.68 μm) achieved in AlN/GaN multiple quantum wells by metalorganic vapor phase epitaxy" [*Appl. Phys. Lett.* 82, 4465 (2005)]. *Appl. Phys. Lett.*, 84(18):3704, 2004.
- [113] DB Laks and A Zunger. Theory of interfacial stability of semiconductor superlattices. *Phys. Rev. B*, 45(24):14177, 1992.

- [114] P Bogusławski, Krzysztof Rapcewicz, and JJ Bernholc. Surface segregation and interface stability of AlN/GaN, GaN/InN, and AlN/InN {0001} epitaxial systems. *Phys. Rev. B*, 61(16):10820, 2000.
- [115] S Nicolay, E Feltin, J-F Carlin, M Mosca, L Nevou, M Tchernycheva, FH Julien, M Ilegems, and N Grandjean. Indium surfactant effect on AlN/GaN heterostructures grown by metal-organic vapor-phase epitaxy: Applications to intersubband transitions. *Appl. Phys. Lett.*, 88(15):151902, 2006.
- [116] C Bayram, N Péré-Laperne, R McClintock, B Fain, and M Razeghi. Pulsed metal-organic chemical vapor deposition of high-quality AlN/GaN superlattices for near-infrared intersubband transitions. *Appl. Phys. Lett.*, 94(12):121902, 2009.
- [117] JS Yang, H Sodabanlu, M Sugiyama, Y Nakano, and Y Shimogaki. Intersubband transition at 1.55 μm in AlN/GaN multiple quantum wells by metal organic vapor phase epitaxy using the pulse injection method at 770°C. *J. Cryst. Growth*, 314(1):252, 2011.
- [118] M Mesrine, N Grandjean, and J Massies. Efficiency of NH_3 as nitrogen source for GaN molecular beam epitaxy. *Appl. Phys. Lett.*, 72(3):350, 1998.
- [119] A Helman, M Tchernycheva, A Lusson, E Warde, FH Julien, Kh Moumanis, G Fishman, E Monroy, B Daudin, D Le Si Dang, et al. Intersubband spectroscopy of doped and undoped GaN/AlN quantum wells grown by molecular-beam epitaxy. *Appl. Phys. Lett.*, 83(25):5196, 2003.
- [120] Y Kotsar, H Machhadani, S Sakr, PK Kandaswamy, M Tchernycheva, E Bellet-Amalric, FH Julien, and E Monroy. III-Nitride semiconductors for intersubband devices. In *SPIE OPTO*, page 79451D. International Society for Optics and Photonics, 2011.
- [121] L Lugani, M Malinverni, S Tirelli, D Marti, E Giraud, J-F Carlin, CR Bolognesi, and N Grandjean. n^+ -GaN grown by ammonia molecular beam epitaxy: application to regrown contacts. *Appl. Phys. Lett.*, 105(20):202113, 2014.
- [122] DD Yang, FH Julien, J-M Lourtioz, P Boucaud, and R Planel. First demonstration of room temperature intersubband-interband double-resonance spectroscopy of GaAs/AlGaAs quantum wells. *Photon. Technol. Lett., IEEE*, 2(6):398, 1990.
- [123] EF Schubert, EO Göbel, Y Horikoshi, K Ploog, and HJ Queisser. Alloy broadening in photoluminescence spectra of $\text{Al}_x\text{Ga}_{1-x}\text{As}$. *Phys. Rev. B*, 30(2):813, 1984.
- [124] G Steude, BK Meyer, A Göldner, A Hoffmann, F Bertram, J Christen, H Amano, and I Akasaki. Optical investigations of AlGaIn on GaN epitaxial films. *Appl. Phys. Lett.*, 74(17):2456, 1999.
- [125] F Natali, D Byrne, M Leroux, B Damilano, F Semond, A Le Louarn, S Veizan, N Grandjean, and J Massies. Inhomogeneous broadening of $\text{Al}_x\text{Ga}_{1-x}\text{N}$ /GaN quantum wells. *Phys. Rev. B*, 71(7):075311, 2005.
- [126] N Grandjean, B Damilano, J Massies, G Neu, M Teissere, I Grzegory, S Porowski, M Gallart, P Lefebvre, B Gil, et al. Optical properties of GaN epilayers and GaN/AlGaIn quantum wells grown by molecular beam epitaxy on GaN (0001) single crystal substrate. *J. Appl. Phys.*, 88(1):183, 2000.
- [127] S Sakr, E Giraud, A Dussaigne, M Tchernycheva, N Grandjean, and FH Julien. Two-color GaN/AlGaIn quantum cascade detector at short infrared wavelengths of 1 and 1.7 μm . *Appl. Phys. Lett.*, 100(18):181103, 2012.
- [128] L Nevou, M Tchernycheva, F Julien, M Raybaut, A Godard, E Rosencher, F Guillot, and E Monroy. Intersubband resonant enhancement of second-harmonic generation in GaN/AlN quantum wells. *Appl. Phys. Lett.*, 89(15):151101, 2006.
- [129] A Köck, E Gornik, G Abstreiter, G Böhm, M Walther, and G Weimann. Double wavelength selective GaAs/AlGaAs infrared detector device. *Appl. Phys. Lett.*, 60(16):2011, 1992.

Bibliography

- [130] MZ Tidrow, JC Chiang, Sheng S Li, and K Bacher. A high strain two-stack two-color quantum well infrared photodetector. *Appl. Phys. Lett.*, 70(7):859, 1997.
- [131] D Hofstetter, F R Giorgetta, E Baumann, Q Yang, C Manz, and K Kohler. Midinfrared quantum cascade detector with a spectrally broad response. *Appl. Phys. Lett.*, 93(22):221106, 2008.
- [132] PK Kandaswamy, F Guillot, E Bellet-Amalric, E Monroy, Lt Nevou, M Tchernycheva, A Michon, FH Julien, E Baumann, F R Giorgetta, et al. GaN/AlN short-period superlattices for intersubband optoelectronics: A systematic study of their epitaxial growth, design, and performance. *J. of Appl. Physics*, 104(9):093501, 2008.
- [133] S Sakr, E Giraud, M Tchernycheva, N Isac, P Quach, E Warde, N Grandjean, and FH Julien. A simplified GaN/AlGaIn quantum cascade detector with an alloy extractor. *Appl. Phys. Lett.*, 101(25):251101, 2012.
- [134] S Sakr. *Dispositifs intersousbandes à base de nitrures d'éléments III du proche infrarouge au THz*. PhD thesis, Université Paris Sud, 2012.
- [135] S Vézian, F Natali, F Semond, and J Massies. From spiral growth to kinetic roughening in molecular-beam epitaxy of GaN (0001). *Phys. Rev. B*, 69(12):125329, 2004.
- [136] A Pesach, S Sakr, E Giraud, O Sorias, L Gal, M Tchernycheva, M Orenstein, N Grandjean, FH Julien, and G Bahir. First demonstration of plasmonic GaN quantum cascade detectors with enhanced efficiency at normal incidence. *Opt. express*, 22(17):21069, 2014.
- [137] D Heitmann, JP Kotthaus, and EG Mohr. Plasmon dispersion and intersubband resonance at high wavevectors in Si (100) inversion layers. *Solid State Commun.*, 44(5):715, 1982.
- [138] JY Andersson, L Lundqvist, and ZF Paska. Quantum efficiency enhancement of AlGaAs/GaAs quantum well infrared detectors using a waveguide with a grating coupler. *Appl. Phys. Lett.*, 58(20):2264, 1991.
- [139] D Bohm. *Quantum theory*. Prentice-Hall, Englewood, Cliffs, N.J., 1951.
- [140] EO Kane. *Tunneling phenomena in solids*, chapter 1. Plenum, New York, 1969.
- [141] LL Chang, L Esaki, and R Tsu. Resonant tunneling in semiconductor double barriers. *Appl. Phys. Lett.*, 24(12):593, 1974.
- [142] S Luryi. Frequency limit of double-barrier resonant-tunneling oscillators. *Appl. Phys. Lett.*, 47(5):490, 1985.
- [143] L Esaki. Long journey into tunneling. *Rev. Mod. Phys.*, 46:237, 1974.
- [144] B Ricco and MY Azbel. Physics of resonant tunneling. the one-dimensional double-barrier case. *Phys. Rev. B*, 29(4):1970, 1984.
- [145] HC Liu. Tunneling time through heterojunction double barrier diodes. *Superlattices Microstruct.*, 3(4):379, 1987.
- [146] EP Wigner. Lower limit for the energy derivative of the scattering phase shift. *Phys. Rev.*, 98(1):145, 1955.
- [147] N Harada and S Kuroda. Lifetime of resonant state in a resonant tunneling system. *Jpn J. Appl. Phys.*, 25(11A):L871, 1986.
- [148] T Weil and B Vinter. Equivalence between resonant tunneling and sequential tunneling in double-barrier diodes. *Appl. Phys. Lett.*, 50(18):1281, 1987.
- [149] S Luryi. Coherent versus incoherent resonant tunneling and implications for fast devices. *Superlattices Microstruct.*, 5(3):375, 1989.

- [150] H Ohnishi, T Inata, S Muto, N Yokoyama, and A Shibatomi. Self-consistent analysis of resonant tunneling current. *Appl. Phys. Lett.*, 49(19):1248, 1986.
- [151] KF Brennan. Self-consistent analysis of resonant tunneling in a two-barrier-one-well microstructure. *J. Appl. Phys.*, 62(6):2392, 1987.
- [152] ER Brown, TCLG Sollner, CD Parker, WD Goodhue, and CL Chen. Oscillations up to 420 ghz in gaas/alas resonant tunneling diodes. *Appl. Phys. Lett.*, 55(17):1777–1779, 1989.
- [153] S Suzuki, M Asada, A Teranishi, H Sugiyama, and H Yokoyama. Fundamental oscillation of resonant tunneling diodes above 1 THz at room temperature. *Appl. Phys. Lett.*, 97(24):242102, 2010.
- [154] K Berland, TG Andersson, and P Hyldgaard. Polarization-balanced design of heterostructures: Application to AlN/GaN double-barrier structures. *Phys. Rev. B*, 84(24):245313, 2011.
- [155] S Sakr, E Warde, M Tchernycheva, and FH Julien. Ballistic transport in GaN/AlGaIn resonant tunneling diodes. *J. of Appl. Physics*, 109(2):023717, 2011.
- [156] SJ Pearton, JC Zolper, RJ Shul, and F Ren. GaN: Processing, defects, and devices. *J. Appl. Phys.*, 86(1):1, 1999.
- [157] F Sacconi, A Di Carlo, and P Lugli. Modeling of gan-based resonant tunneling diodes: Influence of polarization fields. *Phys. Stat. Sol. (a)*, 190(1):295–299, 2002.
- [158] KM Indlekofer, E Dona, J Malindretos, M Bertelli, M Kočan, A Rizzi, and H Lüth. Modelling of polarization charge-induced asymmetry of i–v characteristics of aln/gan-based resonant tunnelling structures. *Phys. Stat. Sol. (b)*, 234(3):769, 2002.
- [159] A Kikuchi, R Bannai, K Kishino, CM Lee, and JI Chyi. AlN/GaN double-barrier resonant tunneling diodes grown by rf-plasma-assisted molecular-beam epitaxy. *Appl. Phys. Lett.*, 81(9):1729, 2002.
- [160] S Golka, C Pflügl, W Schrenk, G Strasser, C Skierbiszewski, et al. Negative differential resistance in dislocation-free GaN/ AlGaIn double-barrier diodes grown on bulk GaN. *Appl. Phys. Lett.*, 88(17):172106, 2006.
- [161] AE Belyaev, CT Foxon, SV Novikov, O Makarovski, L Eaves, et al. Comment on " AlN/GaN double-barrier resonant tunneling diodes grown by rf-plasma-assisted molecular-beam epitaxy" [Appl. Phys. Lett. 81, 1729 (2002)]. *Appl. Phys. Lett.*, 83(17):3626, 2003.
- [162] A Kikuchi, R Bannai, K Kishino, CM Lee, and JI Chyi. Response to “comment on ‘AlN/GaN double-barrier resonant tunneling diodes grown by rf-plasma-assisted molecular-beam epitaxy’” [Appl. Phys. Lett. 83, 3626(2003)]. *Appl. Phys. Lett.*, 83(17):3628, 2003.
- [163] CT Foxon, SV Novikov, AE Belyaev, LX Zhao, O Makarovsky, et al. Current-voltage instabilities in GaN/AlGaIn resonant tunnelling structures. *Phys. Stat. Sol. (c)*, (7):2389, 2003.
- [164] AE Belyaev, O Makarovsky, DJ Walker, L Eaves, CT Foxon, SV Novikov, LX Zhao, RI Dykeman, SV Danylyuk, SA Vitusevich, et al. Resonance and current instabilities in AlN/GaN resonant tunnelling diodes. *Physica E*, 21(2):752, 2004.
- [165] M Hermann, E Monroy, A Helman, B Baur, M Albrecht, et al. Vertical transport in group iii-nitride heterostructures and application in AlN/GaN resonant tunneling diodes. *Phys. Stat. Sol. (c)*, 1(8):2210, 2004.
- [166] S Leconte, E Monroy, and J-M Gerard. Vertical electron transport study in GaN/AlN/GaN heterostructures. *Superlattices Microstruct.*, 40(4):507, 2006.
- [167] S Leconte, F Guillot, E Sarigiannidou, and E Monroy. Charge distribution and vertical electron transport through GaN/AlN/GaN single-barrier structures. *Semicond. Sci. and Technol.*, 22(2):107, 2007.

Bibliography

- [168] S Leconte, L Gerrer, and Eva Monroy. Electronic transport through GaN/AlN single barriers: effect of polarisation and dislocations. *Microelectron. J.*, 40(2):339, 2009.
- [169] C Bayram, Z Vashaei, and M Razeghi. AlN/GaN double-barrier resonant tunneling diodes grown by metal-organic chemical vapor deposition. *Appl. Phys. Lett.*, 96(4):042103, 2010.
- [170] Z Vashaei, C Bayram, and M Razeghi. Demonstration of negative differential resistance in GaN/AlN resonant tunneling diodes at room temperature. *J. of Appl. Physics*, 107(8):083505, 2010.
- [171] C Bayram, Z Vashaei, and M Razeghi. Reliability in room-temperature negative differential resistance characteristics of low-aluminum content AlGaN/GaN double-barrier resonant tunneling diodes. *Appl. Phys. Lett.*, 97(18):181109, 2010.
- [172] C Bayram, Z Vashaei, and M Razeghi. Room temperature negative differential resistance characteristics of polar III-nitride resonant tunneling diodes. *Appl. Phys. Lett.*, 97(9):092104, 2010.
- [173] C Bayram, DK Sadana, Z Vashaei, and M Razeghi. Reliable GaN-based resonant tunneling diodes with reproducible room-temperature negative differential resistance. In *SPIE OPTO*, page 826827. International Society for Optics and Photonics, 2012.
- [174] M Boucherit, A Soltani, E Monroy, M Rousseau, D Deresmes, et al. Investigation of the negative differential resistance reproducibility in AlN/GaN double-barrier resonant tunnelling diodes. *Appl. Phys. Lett.*, 99(18):182109, 2011.
- [175] D Li, L Tang, C Edmunds, J Shao, G Gardner, Michael J Manfra, and O Malis. Repeatable low-temperature negative-differential resistance from $\text{Al}_{0.18}\text{Ga}_{0.82}\text{N}/\text{GaN}$ resonant tunneling diodes grown by molecular-beam epitaxy on free-standing GaN substrates. *Appl. Phys. Lett.*, 100(25):252105, 2012.
- [176] D Li, J Shao, L Tang, C Edmunds, G Gardner, MJ Manfra, and O Malis. Temperature-dependence of negative differential resistance in GaN/AlGa_xN resonant tunneling structures. *Semicond. Sci. and Technol.*, 28(7):074024, 2013.
- [177] L Rigutti, G Jacopin, AL Bugallo, M Tchernycheva, E Warde, FH Julien, R Songmuang, E Galopin, L Largeau, and JC Harmand. Investigation of the electronic transport in GaN nanowires containing GaN/AlN quantum discs. *Nanotechnology*, 21(42):425206, 2010.
- [178] MT Björk, BJ Ohlsson, Claes Thelander, AI Persson, Knut Deppert, LR Wallenberg, and Lars Samuelson. Nanowire resonant tunneling diodes. *Appl. Phys. Lett.*, 81(23):4458, 2002.
- [179] S Sakr, Y Kotsar, M Tchernycheva, E Warde, N Isac, E Monroy, and FH Julien. Resonant tunneling transport in a GaN/AlN multiple-quantum-well structure. *Appl. Phys. Express*, 5(5):052203, 2012.
- [180] M. Dragoman, G. Konstantinidis, A. Cismaru, D. Vasilache, A. Dinescu, D. Dragoman, D. Neculoiu, R. Buiculescu, et al. Negative differential resistance in GaN nanowire network. *Appl. Phys. Lett.*, 96(5):053116, 2010.
- [181] R Songmuang, G Katsaros, E Monroy, P Spathis, Catherine Bougerol, et al. Quantum transport in GaN/AlN double-barrier heterostructure nanowires. *Nano lett.*, 10(9):3545, 2010.
- [182] E Valcheva, K Kirilov, Bo Monemar, H Amano, and I Akasaki. Tunneling effects in short period strained AlN/GaN superlattices. *Phys. Stat. Sol. (c)*, 6(S2):S751, 2009.
- [183] F Sudradjat, W Zhang, K Driscoll, Y Liao, A Bhattacharyya, C Thomidis, L Zhou, D J Smith, TD Moustakas, and R Paiella. Sequential tunneling transport characteristics of gan/algan coupled-quantum-well structures. *J. of Appl. Physics*, 108(10):103704, 2010.
- [184] N Zainal, SV Novikov, CJ Mellor, CT Foxon, and AJ Kent. Current-voltage characteristics of zinc-blende (cubic) $\text{Al}_{0.3}\text{Ga}_{0.7}\text{N}/\text{GaN}$ double barrier resonant tunneling diodes. *Appl. Phys. Lett.*, 97(11):2102, 2010.

- [185] C Mietze, K Lischka, and DJ As. Current–voltage characteristics of cubic Al(Ga)N/GaN double barrier structures on 3C–SiC. *Phys. Stat. Sol. (a)*, 209(3):439, 2012.
- [186] S Sakr, E Warde, M Tchernycheva, L Rigutti, N Isac, and FH Julien. Origin of the electrical instabilities in GaN/AlGaN double-barrier structure. *Appl. Phys. Lett.*, 99(14):142103, 2011.
- [187] T Mattila and RM Nieminen. Ab initio study of oxygen point defects in GaAs, GaN, and AlN. *Phys. Rev. B*, 54(23):16676, 1996.
- [188] MD McCluskey, NM Johnson, Chris G Van de Walle, DP Bour, M Kneissl, and W Walukiewicz. Metastability of oxygen donors in AlGaN. *Phys. Rev. Lett.*, 80(18):4008, 1998.
- [189] TCLG Sollner, WD Goodhue, PE Tannenwald, CD Parker, and DD Peck. Resonant tunneling through quantum wells at frequencies up to 2.5 THz. *Appl. Phys. Lett.*, 43(6):588, 1983.
- [190] FS Cheregi, A Vinattieri, E Feltin, D Simeonov, JF Carlin, R Butté, N Grandjean, and M Gurioli. Biexciton kinetics in GaN quantum wells: Time-resolved and time-integrated photoluminescence measurements. *Phys. Rev. B*, 77(12):125342, 2008.
- [191] J Besbas, A Gadalla, M Gallart, O Crégut, B Hönerlage, P Gilliot, E Feltin, J-F Carlin, R Butté, and N Grandjean. Spin relaxation of free excitons in narrow GaN/Al_xGa_{1-x}N quantum wells. *Phys. Rev. B*, 82(19):195302, 2010.
- [192] C Weisbuch, R Dingle, AC Gossard, and W Wiegmann. Optical characterization of interface disorder in GaAs-Ga_{1-x}Al_xAs multi-quantum well structures. *Solid State Commun.*, 38(8):709, 1981.
- [193] IP Smorchkova, L Chen, T Mates, L Shen, S Heikman, B Moran, S Keller, SP DenBaars, JS Speck, and UK Mishra. AlN/GaN and (Al,Ga)N/AlN/GaN two-dimensional electron gas structures grown by plasma-assisted molecular-beam epitaxy. *J. of Appl. Physics*, 90(10):5196, 2001.
- [194] B Gil, P Lefebvre, J Allegre, H Mathieu, N Grandjean, M Leroux, J Massies, P Bigenwald, and P Christol. Observation of long-lived oblique excitons in gan-algan multiple quantum wells. *Phys. Rev. B*, 59(15):10246, 1999.
- [195] NAK Kaufmann, A Dussaigne, D Martin, P Valvin, T Guillet, B Gil, F Ivaldi, S Kret, and N Grandjean. Thermal annealing of molecular beam epitaxy-grown InGaN/GaN single quantum well. *Semicond. Sci. and Technol.*, 27(10):105023, 2012.
- [196] MH Xie, SM Seutter, WK Zhu, LX Zheng, Huasheng Wu, and SY Tong. Anisotropic step-flow growth and island growth of GaN (0001) by molecular beam epitaxy. *Phys. Rev. Lett.*, 82(13):2749, 1999.

Remerciements

La thèse n'est pas seulement un travail personnel, et nécessite le concours d'un certain nombre de personnes. Je ne peux donc pas terminer ce manuscrit sans citer ceux qui ont rendu ce travail possible.

En premier lieu, je tiens à remercier le Prof. Hans Peter Herzig de Neuchâtel pour avoir accepté de présider mon jury de thèse. Je remercie également les autres membres du jury, Prof. Christophe Ballif, Dr. François Julien et Dr. Jean-Yves Duboz, pour leur lectures attentives et critiques de mon manuscrit, ainsi que pour les discussions intéressantes à l'occasion de mon examen.

Je tiens évidemment à remercier Nicolas Grandjean, mon directeur de thèse, qui m'a accepté dans son laboratoire, et m'a donné l'opportunité de mener à bien mes travaux de recherche sur un sujet aussi stimulant durant ces quelques années au LASPE. J'ai beaucoup appris tant humainement que scientifiquement lors de nos régulières discussions. Sa volonté de remettre en question les hypothèses préétablies nous a permis d'avancer dans la compréhension des problèmes liés aux diodes à effet tunnel résonant, même si les résultats n'ont pas été à la hauteur de nos espérances. J'ai apprécié son enthousiasme communicatif et nécessaire pour retrouver la motivation après plusieurs jours de manips infructueuses. Je n'oublierai pas les moments passés à épilucher les courbes I-V à la recherche d'une trace de NDR, ou d'une "bouffiole".

Je remercie également les personnes extérieures à l'EPFL, avec qui j'ai eu l'occasion de collaborer durant le projet Unitride : les équipes de l'IEF à Paris, du CEA à Grenoble et de Technion à Haifa. Et plus particulièrement, je remercie Salam Sakr, pour notre fructueuse collaboration ainsi que nos nombreux échanges scientifiques. Concernant le projet du NCCR, je remercie Laurent Nevou du groupe de Jérôme Faist à l'ETH Zürich.

Toutes les compétences techniques nécessaires à la réalisation de ce travail, je les ai acquises grâce aux nombreux échanges avec mes collègues du LASPE.

Concernant la MBE, je tiens à remercier Denis et Amélie, qui ont fait tout ce qu'ils ont pu pour me transmettre leur savoir, même s'il est regrettable qu'Amélie nous ait quittés rapidement pour de meilleures latitudes. La team MBE était également composée de Marco M. et Nils. Merci pour ces moments partagés autour du traditionnel café/biscuits du Lundi matin, ainsi que lors des ouvertures, où les heures passées à visser et dévisser passait plus rapidement en votre compagnie.

Tout ce que j'ai appris sur le processing, je le dois à Nino et Jean-Michel, qui ont usé de patience pour m'apprendre à utiliser les équipements de la salle blanche, et m'ont conseillé pour la réalisation de mes masques. Au passage, je remercie également les membres de l'équipe des

Acknowledgements

salles blanches, qui sont toujours disponibles et maintiennent les installations en parfait état de fonctionnement. Merci donc à Nicolas Leiser, ainsi qu'à Damien et Yoann Trolliet.

Je remercie aussi ceux qui m'ont transmis leur savoir en spectroscopie et m'ont épaulé lors de certaines manips, c'est à dire Jacques, Georg (au passage, merci à vous deux pour les belles balades à moto) et Marlene. Je n'oublie évidemment pas Raphaël qui, en plus de ses connaissances en spectro, est un champion de biblio et a toujours une réponse à mes questions. J'ai particulièrement apprécié sa disponibilité, ainsi que nos discussions enrichissantes, scientifiques ou moins scientifiques.

Un grand merci également à la team MOCVD, pour tous les échantillons "state of the art" (qui suscitent la jalousie de nos compétiteurs), que vous avez épitaxiés pour ce travail. J'ai nommé Denis, Jean-François et Lise (Merci Lise également pour cette très bonne ambiance musicale dans le bureau et ta constante bonne humeur).

Je remercie également nos secrétaires, Aline et Nadja, pour leur aide et leur disponibilité. Merci aussi à Roger pour le support technique, toujours rapide et efficace, et à Florence du service informatique pour son support technique indispensable.

Je n'oublie évidemment pas les autres membres du groupe, et plus généralement de l'EPFL, qui ont contribué à la bonne ambiance du labo, et qui m'ont laissé des souvenirs inoubliables, autour d'une bière à Sat, d'un café, d'un barbecue ou sur les pistes de ski lors de nos mémorables sorties de labo. Merci donc à (dans le désordre) Munise, Markus, Guillaume, Julien, Eric, Pascal, Marco R., Yoshi, Marcel, Jérôme, Christophe, Gwénolé, Gedis, Mehran, Pierre, Hiro, Christian, Jonas, Luca, Lorenzo, Noelia, Gatien, Mauro et Alexei. J'espère n'avoir oublié personne. Je souhaite également bonne chance aux derniers arrivants au LASPE : Joachim, Sebastian, Ian et Pirouz.

Pour finir je tiens à remercier mes proches en commençant par mes parents, Marie-Claude et Jacques, qui m'ont toujours soutenu et fait confiance, et ma sœur, Lorène, que je ne vois plus trop souvent, à regrets. Je remercie également ma belle-famille qui m'a accepté à bras ouverts, et qui font preuve d'une infinie gentillesse à mon égard. Finalement, un immense merci à mon épouse Neda qui a partagé mes joies et mes peines, m'a soutenu et supporté dans les moments difficiles de la thèse.

Concernant le soutien financier, ce projet a été financé par le projet européen FP7 "Unitride", et par le Fond National Suisse à travers le consortium "Quantum Photonics".

10 août 2015

E. G.

CURRICULUM VITAE

Étienne Giraud

PhD candidate at EPFL (Switzerland)
Master of science from EPFL (Switzerland)
Engineer graduated from École Polytechnique (France)

date of birth: September 18th, 1984
place of birth: Colombes, France
Nationality: France
marital status: married

Professional address: EPFL – ICMP – LASPE
station 3
CH-1015 Lausanne, Switzerland
tel: +41-21-693-45-33
e-mail: etienne.giraud@epfl.ch

personal address:
Ch. des Champs-Meunier 11B
CH-1052 Le Mont sur Lausanne
Switzerland
e-mail: etienne.giraud@polytechnique.edu
mobile: +41-76-270-79-94

Education

- 08/2010-present: **PhD** in physics in the Laboratory of advanced semiconductors for photonics and electronics (LASPE), EPF Lausanne, Switzerland.
PhD thesis: Optical and transport properties of GaN/(Al,Ga)N heterostructures in prospect of infrared unipolar devices.
supervisor: Prof. N. Grandjean.
- 09/2008-05/2010 **MS** in Material science, EPF Lausanne, Switzerland.
Diploma thesis: Fabrication and characterization of fluorescent polymer thin films for lighting applications.
Supervisor: Prof. L. Zuppiroli.
- 09/2005-04/2010: **Engineering Diploma** from École Polytechnique, Palaiseau, France.
Specialization in Physics.
- 09/2002-07/2005: **Preparatory School** in Lycée Chaptal, Paris, France.
09/1999-07/2002: **High school degree** in Lycée Albert Camus, Bois-Colombes, France.

Experience

- 09/2010-12/2014: Teaching Assistant at EPFL: writing the exercise series, supervising bachelor and master students for exercises and practical works, correcting student reports and exams.
- 04/2008-07/2008: Research internship in Laboratory of Prof. L. Forro at EPF Lausanne: Rheology of carbon nanotubes dispersions using optical tweezers.
- 08/2007: Internship as a worker in a car assembly line at Nissan in Yokohama, Japan.

Skills

- Languages: French: native speaker
English: fluent
German: scholar level
Japanese : basics (JLPT 4th Level)
Persian : basics
- Computer skills: *Data processing and programming:* MatLab, Mathematica, Origin, Labview, Java.
Computer-aided drawing: SolidWorks, Inkscape.
Word processing: Latex, Microsoft Office suite.
Simulations of semiconductor hetero-structures.
- Laboratory skills : **Semiconductors epitaxy:** MBE (ultra high vacuum semiconductor growth technique).
Structural characterization of thin films: X-ray diffraction, atomic force microscopy, scanning electron microscopy.
Optical spectroscopy: photoluminescence, absorption and ellipsometry measurements.
Clean room facilities: optical lithography, e-beam evaporation, plasma etching (ICP, RIE), and deposition (PECVD, sputtering).
Electrical characterization and transport measurements in semiconductors

Workshops and conferences attended

March 2011:	Euro-MBE conference, L'Alpe d'Huez, France (attendee)
May 2011:	Swiss and Austrian Physical society meeting, Lausanne, Switzerland (oral presentation).
September 2011:	Internal Conference on intersubband transitions in quantum wells, Badesi, Italy (Poster presentation)
August 2012:	International conference on physics of semiconductors, Zurich, Switzerland (Poster presentation).
August 2013:	International nano-optoelectronics workshop, Cargese, France (Poster presentation).
August 2014:	International workshop on nitride semiconductors, Wroclaw, Poland (Oral presentation).
2010 – 2014:	Several oral or poster presentations in internal EPFL seminar or workshops.

Selected publications

- P. Corfdir, A. Dussaigne, H. Teisseyre, T. Suski, I. Grzegory, P. Lefebvre, E. Giraud, J.-D. Ganière, N. Grandjean, and B. Deveaud-Plédran, Thermal carrier emission and non-radiative recombinations in non-polar (Al,Ga)N/GaN QWs grown on bulk GaN, *J. Appl. Phys.* 111, 033517 (2012)
- S. Sakr, E. Giraud, A. Dussaigne, M. Tchernycheva, N. Grandjean, F.H Julien, Two-color GaN/AlGaIn quantum cascade detector at short infrared wavelengths of 1 and 1.7 μm , *Appl. Phys. Lett.* 100, 181103 (2012) – highlighted in *Semiconductors Today*
- S. Sakr, E. Giraud, M. Tchernycheva, N. Isac, P. Quach, E. Warde, N. Grandjean, and F.H Julien, A simplified GaN/AlGaIn quantum cascade detector with an alloy extractor, *Appl. Phys. Lett.* 101, 251101 (2012)
- L. Zhou, M. Gonschorek, E. Giraud, E. Feltin, J.-F. Carlin, N. Grandjean, D. J. Smith, M. R. McCartney, Measurement of polarization-induced electric fields in GaN/AlInN quantum wells, *Appl. Phys. Lett.* 101, 251902 (2012)
- L. Nevou, E. Giraud, F. Castellano, N. Grandjean and J. Faist, Interaction between meta-materials and bound excitons in bulk GaN at THz frequency, *Optic Express* 22, 3199 (2014)
- A. Pesach, S. Sakr, E. Giraud, N. Grandjean, F. H. Julien, G. Bahir, First demonstration of plasmonic GaN quantum cascade detectors with enhanced efficiency at normal incidence, *Optic Express* 22, 21069 (2014)

Interests

Sports: rugby, running, tennis.

Music: Violin, 12 years study in conservatory. participations in regional competitions.

Miscellaneous

Driving Liscence

Swiss residency permit since 07/2010

References

Prof. N. Grandjean, EPFL

(PhD thesis supervisor)

Prof. L. Zuppiroli, EPFL

(Master thesis supervisor)